POLITECNICO DI TORINO

Master's Degree Thesis in Mechanical Engineering

A Study and Implementation of Stability in Electrodynamic Levitation Systems

Supervisors

Prof. Nicola AMATI

Prof. Renato GALLUZZI

Prof. Andrea TONOLI

Candidate

Marius PAKŠTYS

October 2022

Abstract

The increased interest in electrodynamic levitation systems for the purpose of commercial transportation has put a focus on the need to fully characterise their dynamic behaviour. The requirement for passenger comfort has introduced challenges related to the stability and control of vibrations that may be induced from track irregularities and changing weight distribution in the vehicle. The aim of the present thesis is to understand the solution to the inherent instability of the levitating system by means of a quarter-car model, with the possibility of validating the same by means of a dedicated test bench. A voice coil that exhibits a sprung and unsprung mass provides the ability to practically study the system, by considering a lack of decoupling of the masses, as well as an application of passive damping. A COMSOL Multiphysics® model of the experimental system is refined to account for magnet misalignment and spacing, also considering two differing orientations of the Halbach array. Offset values for each nominal air gap are suggested, for each Halbach array, obtained from comparing numerical and experimental forces. A general offset value is also reported for each array, accounting for pad irregularities, with satisfactory correspondence between experimental and FEM data. To further improve on the discussion of stability, several control strategies are explored, where the initial approach consists of implementing extensively studied solutions in the automotive field, namely skyhook and groundhook damping. A stability analysis in MATLAB® and Simulink® is performed, and simulations in the time domain confirm certain favourable configurations. A general approach is then adopted, by means of the Linear Quadratic Regulator introduced in a simplified model of the system that exhibits observable states. The compatibility of the reduced order model with the model including the inherent instability is verified in frequency domain. The effect of the control input penalisation on the sensitivity of a single weighting parameter influencing the states of interest is explored and agreeable design choices are suggested, considering varying excitation profiles pertaining to the track. These include a sinusoidal profile used for the HyperloopTT™ test track, and a random profile defined by the ISO/TC 108/WG9 standard, as well as a combination of the two.

Acknowledgements

First and foremost, I deeply thank my brother Saulius for his unwavering support during the course of my academic career, whose forward thinking has been crucial to keeping me curious about new opportunities.

My debt of gratitude also extends to my parents and grandparents, whose lifting conversations reminded me of other important aspects of life, whose belief and aid in emotional and practical matters was undeniably precious and selfless.

I would like to thank Renato, who has been the most prominent and supportive figure in my thesis work, whose guidance and advice has enabled me to greatly expand my understanding of the topics I endeavoured to study. I also wholly appreciate the time and experience gained with my colleagues Eugenio and Lorenzo, whose enthusiasm and motivation are profound. I would also like to thank Professors Nicola Amati and Andrea Tonoli for making this work possible, and for showing their confidence in me.

Lastly, I thank my close friends Rodrigo, Luca, Gianluca, Gaia, and Carina, who have been always present, genuine and joyful during the course of my thesis. I will forever hold dear the time I have shared with you.

I eagerly await the challenges, failures and achievements in the next stages of my academic, professional, and personal journeys.

Table of Contents

List of Tables

List of Figures

Nomenclature

L	Inductance component of the electric circuit	H
R	Resistance component of the electric circuit	Ω
E	Back electromotive force (BEMF)	V
E_d	Direct component of BEMF	V
E_q	Quadrature component of BEMF	V
i	Current flowing in the electric circuit	A
i_d	Direct component of the current	A
i_q	Quadrature component of the current	A
ω_p	Pole frequency of electrodynamic circuit	$\mathrm{rad\,s^{-1}}$
ω	Excitation frequency	$\mathrm{rad\,s^{-1}}$
Λ	Flux linkage	Wb
Λ_0	Amplitude of flux linkage	Wb
z_p	Unsprung mass vertical displacement (air gap)	m
$z_{p,0}$	Nominal unsprung mass vertical displacement (nominal air gap)	m
v	Longitudinal velocity	$\mathrm{m\,s^{-1}}$
γ	Magnetic pole pair pitch ratio	m
F	Force (with the subscript specifying the type)	N
N_b	Number of branches in the equivalent electrodynamic circuit	-
m_s	Sprung mass of the quarter-car model for the system	kg

m_p	Unsprung mass of the quarter-car model for the system	kg
m_t	Total mass of the quarter-car model for the system	kg
k_s	Intermediate suspension stiffness	$\mathrm{N\,m^{-1}}$
c_s	Intermediate suspension damping coefficient	$\mathrm{N\,s\,m^{-1}}$
c_{sky}	Skyhook damping coefficient	$\mathrm{N\,s\,m^{-1}}$
c_{gr}	Groundhook damping coefficient	$\mathrm{N\,s\,m^{-1}}$
z_R	Vertical road profile at a spatial coordinate	m
A_R	Amplitude of road profile	m
Ω	Spatial frequency or wave number	$\mathrm{rad\,m^{-1}}$
Ω_0	Reference spatial frequency or wave number	$\mathrm{rad\,m^{-1}}$
x	Longitudinal distance	m
x_0	Longitudinal distance travelled	m
λ	Wavelength	m
λ_f	Wavelength for filter in ISO profile generation	m
λ_f	Frequency for filter in ISO profile generation	Hz
t	Time	s
Z_{HA}	Vertical displacement of Halbach array on the HTT test track	m
Z_D	Amplitude pertaining to mechanical loading	m
λ_L	Wavelength pertaining to mechanical and thermal loading	m
$Z_{\Delta T}$	Amplitude pertaining to thermal loading	m
Z_S	Amplitude pertaining to effect of linear synchronous motor	m
λ_S	Wavelength pertaining to effect of linear synchronous motor	m
$\Phi(\Omega)$	One sided power spectral density (PSD)	$\mathrm{m^2/(rad/m)}$
ξ	Spatial shift pertaining to auto-correlation function	m
$R(\xi)$	Auto-correlation function in spatial domain	$\mathrm{m^2}$

σ^2	Variance of random profile	m^2
$\Delta\Omega$	Wave number discretisation	$\mathrm{rad\,m^{-1}}$
N	Number of sine waves or wave numbers	-
w	Waviness	-
A_i	Amplitude of sine wave in sinusoidal approximation	m
G_r	Roughness coefficient	$\mathrm{m\,rad}$
$TF(s)$	Transfer function for ISO profile generation	-
J	Quadratic cost function	$\mathrm{E\,U}^2$
$\boldsymbol{x}$	State vector	E U
u	Control input	N
R	Control input penalisation	-
r	State penalisation	-
$\boldsymbol{K}$	State gain matrix	N/E U
k_p	Equivalent stiffness of pad	$\mathrm{N\,m^{-1}}$
z_s	Sprung mass vertical displacement	m
$\dot{z}_s$	Sprung mass vertical velocity	$\mathrm{m\,s^{-1}}$
$\ddot{z}_s$	Sprung mass vertical acceleration	$\mathrm{m\,s^{-2}}$
$\dot{z}_p$	Unsprung mass vertical velocity	$\mathrm{m\,s^{-1}}$
B_r	Remanence flux of permanent magnet	T
μ_{pm}	Recoil permeability of permanent magnet	-
ρ_t	Resistivity of track	Ωm
z_{in}	Input profile	m
D_t	Average diameter of test bench track	m
L_p	Length of pad with Halbach array	m

Chapter 1

Introduction

1.1 System

The theoretical model by which the system can be modelled and subsequently controlled is that of a quarter-car configuration, due to prevalent similarities in conventional automotive systems. In particular, it can be demonstrated that the system in a single degree of freedom arrangement exhibits an inherent instability beyond a certain threshold of longitudinal velocity [1]. Indeed, the solution involves decoupling the pad (bogie) and the capsule (passenger compartment), effectively converting the system into a two degree of freedom arrangement. In between the sprung and unsprung masses, a suspension is introduced, where an optimal damping factor can be identified in a passive damping configuration, maximising the system's stability. The model for this system can be noted in Figure 1.1. The identification of this damping factor requires a stability analysis of the system, by observing the poles of the dynamic matrix. For each damping factor, for a specific longitudinal velocity, a set of poles can be extracted, with the largest pole representing the most critical condition for the system's stability.

Moreover, the model used to fully capture the system's instability consists of a lumped parameter approach, coupling the electrical and mechanical domains [1]. This approach involves states that may not be directly measured, such as the eddy currents in the track, as well as states that can be readily observed, for example the vertical displacements of the sprung and unsprung masses. This model in particular is implemented in the stability and dynamic response analyses of conventional automotive control strategies. As a further step, a model incorporating the pad as an equivalent stiffness is used in the exploration of control strategies pertaining to a Linear Quadratic Regulator.

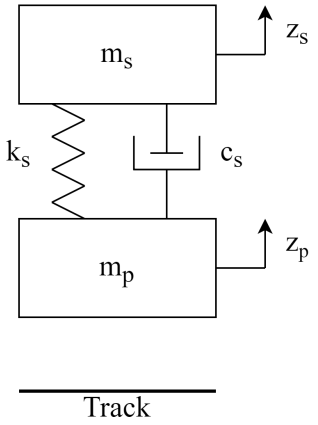

Figure 1.1: Quarter-car model of electrodynamically levitated pod.

For clarity, it is necessary to outline the key arguments pertaining to the system incorporating a lumped parameter approach. The electrodynamic domain is modelled by means of a multi-branch electrical circuit that consists of a voltage generator representing a Back Electromotive Force (BEMF), in parallel with a number of branches, each containing a resistor and inductor connected in series. The balance of terms pertaining to the k-th branch of the circuit is indicated in Equation 1.1, representing the starting point from which the formulations for the lift and drag forces can be obtained.

$$L_k \frac{di_k}{dt} + R_k i_k + E = 0 \tag{1.1}$$

By considering a transformation from the static to the rotating reference frame concerning the current, and by identifying the BEMF in terms of the flux linkage, two coupled expressions that become useful for describing the electrodynamic behaviour of the system are obtained, evident in Equations 1.2 and 1.4. In particular, the BEMF is distinguished with its direct and quadrature components highlighted in Equations 1.3 and 1.5. The electrodynamic pole frequency is defined as for an eddy current damper [2] or electromagnetic bearing, due to the exploitation of identical principles for modeling.

$$\frac{di_{d,k}}{dt} = -\omega_{p,k} i_{d,k} + \omega i_{q,k} - \frac{E_d}{L_k} \tag{1.2}$$

$$E_d = \frac{\partial \Lambda}{\partial z_p} \dot{z_p} \tag{1.3}$$

$$\frac{di_{q,k}}{dt} = -\omega_{p,k} i_{q,k} - \omega i_{d,k} - \frac{E_q}{L_k} \tag{1.4}$$

$$E_q = \Lambda \frac{v}{\gamma} \tag{1.5}$$

Performing a power balance, three contributions are evident: the rate of change of stored magnetic energy, the dissipated power by Joule effect, and the mechanical power developed. By focusing one's attention on the final contribution, the lift and drag forces are highlighted in Equations 1.6 and 1.7 respectively. In particular, these forces stem from the interaction between the Halbach array and the track, when a relative motion between the two is present.

$$F_{lift} = \frac{E_d}{\dot{z_p}} \sum_{k=1}^{N_b} i_{dk} \tag{1.6}$$

$$F_{drag} = -\frac{E_g}{v} \sum_{k=1}^{N_b} i_{q,k} \tag{1.7}$$

Having identified the non-linear expressions for the lift and drag force, a linearisation in particular for the lift force is performed around a nominal air gap to allow for its inclusion in a state space representation of the system. This linearisation depends on Taylor-expanding the flux linkage, meaning that the Equations 1.2 and 1.4 for the direct and quadrature components of the current necessary for the aforementioned power balance also become linearised around a nominal air gap, allowing them to be designated as states. The appropriate terms concerning these linearised equations can be found represented within a matrix notation for a system incorporating the inherent instability in section A.1 of the Appendix. The nominal air gap is computed by equating the total weight force of the system with the expression of the non-linear lift force in static conditions, present in Equation 1.9. This force is obtained by neglecting all transient variables, and developing an expression for the direct current component stemming from Equations 1.2 and 1.4, to be substituted into Equation 1.6. The linearised lift force and the nominal air gap expressions are indicated in Equations 1.8 and 1.10 respectively.

$$\bar{F}_{lift} = -\sum_{k=1}^{N_b} \left(\frac{\Lambda_0^2}{\gamma L_k} \, \mathrm{e}^{-2z_{p,0}/\gamma} + \frac{2\Lambda_0}{\gamma} \, \mathrm{e}^{-z_{p,0}/\gamma} \, i_{d,k} \right) \tag{1.8}$$

$$F_{lift,s} = \frac{\Lambda_0^2}{\gamma} \, \mathrm{e}^{-2z_p/\gamma} \, \Gamma(\omega) \tag{1.9}$$

$$z_{p,0}(\omega) = -\frac{\gamma}{2} \ln \left(\frac{m_t g \gamma}{\Lambda_0^2 \Gamma(\omega)} \right) \tag{1.10}$$

$$\Gamma(\omega) = \sum_{k=1}^{N_b} \frac{\omega^2/\omega_{p,k}^2}{L_k(1 + \omega^2/\omega_{p,k}^2)} \tag{1.11}$$

The lift force in static conditions is useful for the treatment regarding the tuning of the FEM model to the experimental data. Likewise, the drag force is useful to the same end, with its definition outlined in Equation 1.12. Similarly to the derivation of the lift force, an expression for the quadrature current component is obtained by operating on Equations 1.2 and 1.4, disregarding all transient variables, and substituting into Equation 1.7.

$$F_{drag,s} = \frac{\Lambda_0^2}{\gamma} \, \mathrm{e}^{-2z_p/\gamma} \, \Theta(\omega) \tag{1.12}$$

$$\Theta(\omega) = \sum_{k=1}^{N_b} \frac{\omega/\omega_{p,k}}{L_k(1+\omega^2/\omega_{p,k}^2)} \tag{1.13}$$

The above mentioned discussion represents the foundation for the dynamic analysis and numerical validation of the automotive control strategies, as well as the fitting for the FEM model to the experimental test bench, herein reported.

1.2 Test Bench

Considering the extensive theoretical treatment of the system, a test bench to validate the stability and dynamic response of the system is used. A notable feature of the test bench is its rotating track. It is constructed with a vertical rotation axis layout, to reduce footprint, as a linear guideway entails larger space requirements [3]. The circular non-ferromagnetic metal (copper) track is attached to an aluminium disc, whose rotation is induced by means of a Kollmorgen™ servo-motor. A flexible joint connection between the disc and motor shaft allows for this rotation. In particular, the average diameter of the track D_t, and the length of the pad L_p can inform an appropriate selection of the test bench dimensions. The ratio $D_t/L_p \geq 10$ ensures that the peripheral velocity can be approximated as constant along the entire pad length. A horizontal rotation axis layout is also possible [4], however the size of the circular track increases considerably if a planar pad is desired. A constant air gap must be guaranteed, meaning the Halbach array must be curved with respect to the track, increasing costs. The air gap is ideally constant in the vertical axis layout, however in practice conical motion due to the lift force may cause variations. Figure 1.2 indicates the most prominent features of the test bench. On one side of the test bench, a structure facilitating the mounting of the pad is present, with the possibility of mounting two different assemblies. Quasi-static phenomena can be studied using one layout of the test bench, while the system's dynamics can be studied using another.

For quasi-static experimentation, the pad is fixed by means of flex hinges in the vertical and horizontal directions. HBM™ S2 load cells are present along the

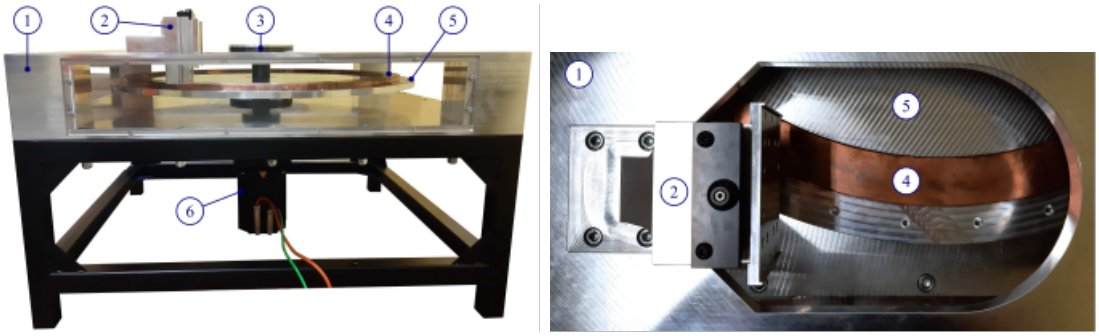

(a) Lateral view of test bench.

(b) Top view of slot cavity on test bench.

Figure 1.2: Lateral and top views of the test bench. Prominent features: 1. Test bench structure; 2. Equipment support block with micro-metric stage; 3. Shaft; 4. Copper track; 5. Aluminium disc; 6. Servo-motor.

vertical and horizontal directions to acquire the lift force and drag force, respectively. The vertical flex hinges allow for horizontal deflection, while the horizontal flex hinges permit vertical deflection. Two pad types are studied, the 90° and the 45° magnetisation orientations of the Halbach array, to understand their performance differences. Figure 1.3 summarises the described assembly.

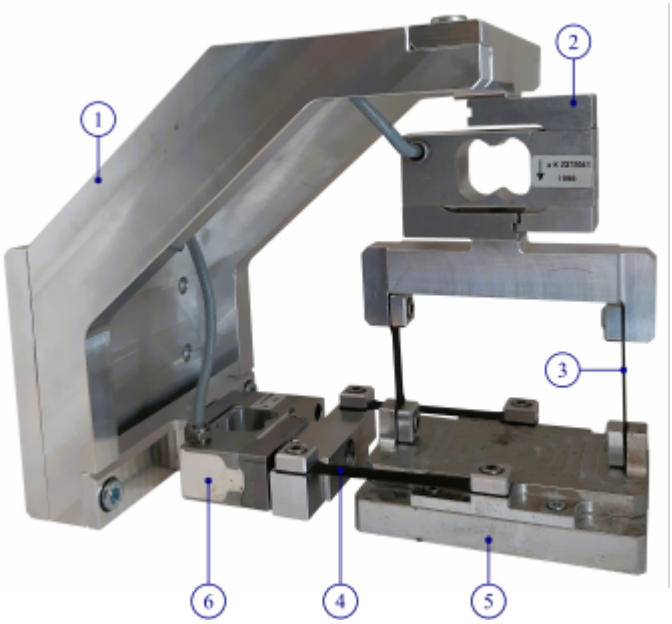

Figure 1.3: Assembly of equipment required for quasi-static experiments. Prominent features: 1. Support structure; 2. HBM™ S2 load cell for lift force acquisition; 3. Vertical flex hinge; 4. Horizontal flex hinge; 5. Mount with PM array; 6. HBM™ S2 load cell for drag force acquisition.

To acquire quasi-static force data, a nominal air gap is set using the micro-metric stage on the test bench. A target angular velocity corresponding to an equivalent longitudinal velocity is imposed in the Kollmorgen™ Workbench software controlling the servo-motor. Once this velocity is reached, acquisition is executed by means of Siemens LMS™ SCADAS Mobile platform. Lift and drag force data are logged in this manner for different nominal air gaps. A COMSOL Multiphysics® model is produced to simulate the behaviour of the test bench in the static configuration for each pad type, and its tuning is facilitated by the experimental data recorded.

In the dynamic configuration, the pad is attached to an effective unsprung mass of a voice coil assembly, with the ferromagnetic casing of the mover representing the sprung mass. The use of a voice coil is advantageous due to the possibility of controlling its vertical displacement by means of externally supplied current. With a voltage across the coil's terminals, a separation of the sprung and unsprung masses is achieved, allowing one to study the dynamic response of the system as though a suspension were present. Additionally, control strategies based on state observation can be implemented, to understand the system's capability of being actively controlled. The voice coil subsystem can be replaced with a passive damper, with a damping coefficient corresponding to optimum stability of the system, allowing one to compare the effectiveness of an active control as opposed to a passive damping. Note that the scope of this work does not extend to treating dynamic experimental data, and therefore further details on the dynamic configuration are not provided.

The overall aim of the study on stability and control of the system is to obtain strategies and corresponding system parameters for which passenger comfort is prioritised. An alternative consideration is the prioritisation of handling, however this does not fall into the scope of commercial applications for the system's technology. A further aim is to obtain a satisfactory characterisation of the behaviour of the non-linear system, by means of a FEM model.

Chapter 2

FEM Model

2.1 Model Tuning

The expected non-conformity of the results produced by the 3D FEM model on COMSOL Multiphysics® and the results obtained experimentally for the two different pad configurations demands further treatment regarding the FEM model. The presence of pitch, yaw, and roll angles, however minute in the experimental setup of the pad yield performance differences when compared to the ideal setup. Moreover, irregularities in the magnet array as well as in the track impact the magnitude of the lift force that can be generated. Investing time and effort in quantifying these deviations from the nominal condition may prove to be costly in light of the potential improvement in accuracy of the FEM model. A more straightforward approach is adopted, where the effects of irregularities are lumped into an air gap offset added to the nominal air gap of the model. In particular, a study is performed for the 90° and the 45° configurations of the Halbach array, for which experimental data are already available.

Note that the use of the lift and drag force formulations in static conditions is necessary to identify the air gap offset. In particular, a fitting for these forces is performed for both the experimental and nominal FEM data, allowing the curves to be more readily compared, as a root mean square (RMS) error can be extracted. An additional motivation for using the expressions fitted to the experimental and FEM data is the computational cost; generating multiple curves for the same nominal air gap at different offsets on FEM software would considerably increase the time to reach the final results. The identification of the most adequate air gap offset is achieved by minimising the squared error between the forces obtained using the expressions of the lift and drag in static conditions fitted to the FEM and experimental data. Specifically, a vector of offsets is introduced as inputs for

the lift and drag forces fitted to the FEM data, to vary the outputs over a range of longitudinal velocities. The most appropriate offset corresponds to the lowest RMS error between the experimental and FEM curves.

2.1.1 45° configuration

The 3D FEM model for the pad in 45° configuration incorporates the magnetisation scheme depicted in Figure 2.1. The parameters obtained after fitting the multi-branch electrical model used for the generation of the forces in MATLAB® are reported in Table 2.1 for the experimental data and in Table 2.2 for the COMSOL data. In particular, to configure the 3D FEM model, magnet and track characteristics are introduced. Regarding the magnet array, the remanence flux $B_r = 1.35\,\mathrm{T}$ while the recoil permeability $\mu_{pm} = 1.05$. The magnet side length is 12.7 mm and there are 8 magnets per pole pair, which is useful for the identification of the magnetic pole pair pitch ratio, γ. The resistivity of the copper track is set to $\rho_t = 1.72 \times 10^{-8}\ \Omega\,\mathrm{m}$ for both configuration studies. As the amplitude of the flux linkage Λ_0 is not known, a unitary value is imposed, meaning all parameters obtained from fitting the multi-branch electrical model to the nominal FEM data and the experimental data are in correspondence with this value (applicable also for the 90° configuration).

When carrying out the fitting for each nominal air gap, the optimal air gap offset is observed to be different and unique. By applying these unique air gap offsets to the expressions for static lift and drag corresponding to FEM data, the fit achieved between the numerical curves and the experimental data is remarkable as seen in Figures 2.2 and 2.3. Moreover, a plot, present in Figure 2.4 can be generated indicating the air gap offsets for each nominal air gap. Multiple offsets are generated for each air gap, by focusing the least square optimisation on the error stemming only from the lift force, only from the drag force, and from the two combined. The plot evidences a greater weighting of the error in favour of the lift force, due to its larger magnitude with respect to the drag force, using the Halbach array in question. Indeed, Figure 2.5 indicates the contribution (as a percentage) to the combined error for the lift and drag forces, with a greater weighting for the lift force evident in lower air gaps, due to a comparatively larger magnitude.

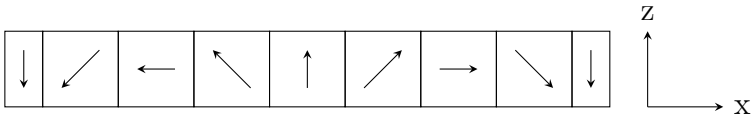

Figure 2.1: Magnetisation scheme for Halbach array in 45° configuration (cross-sectional view).

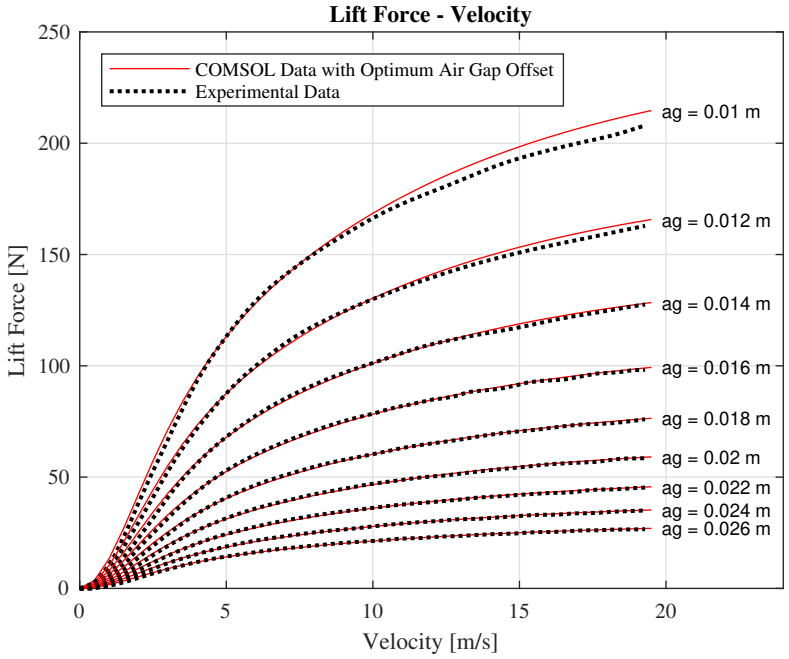

Figure 2.2: Lift force fitted to a set of experimental data for nominal air gaps by means of unique air gap offsets obtained from minimisation of RMS error for 45° configuration.

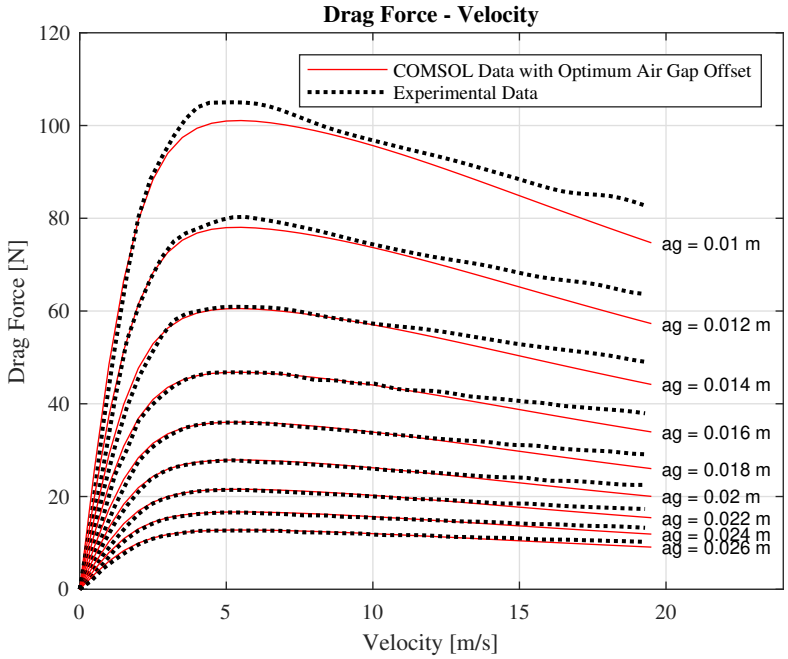

Figure 2.3: Drag force fitted to a set of experimental data for nominal air gaps by means of unique air gap offsets obtained from minimisation of RMS error for 45° configuration.

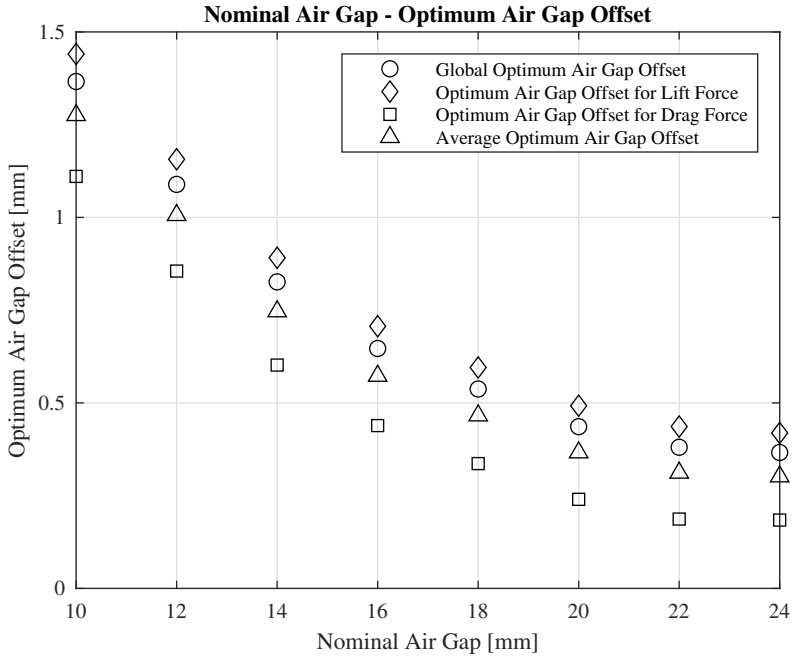

Figure 2.4: Optimum air gap offsets for each nominal air gap, dependent on the error used for computation regarding the 45° configuration.

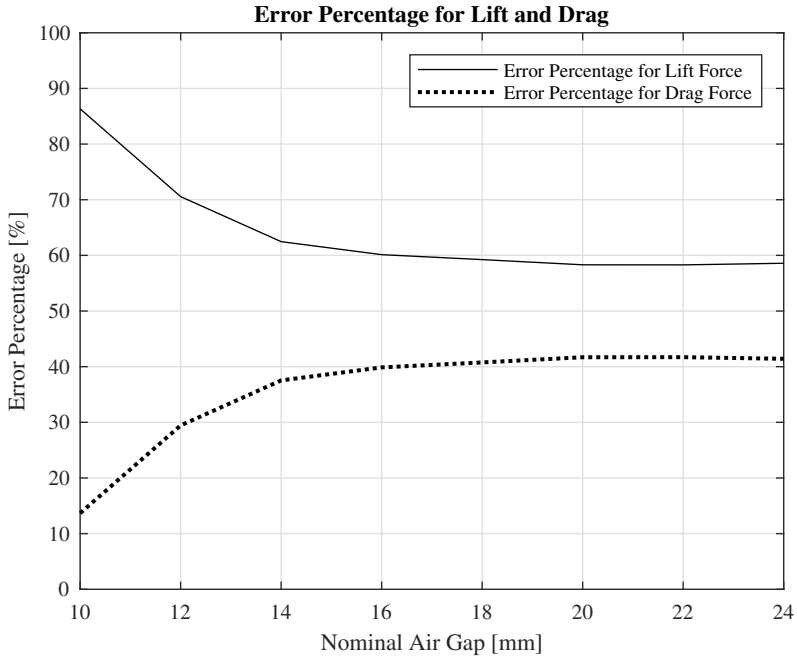

Figure 2.5: Percentage of combined error for lift and drag force, for each nominal air gap, in the identification of unique air gap offsets for 45° configuration.

Air gap [mm]	$\omega_{p,1}$ [rad s^{-1}]	$\omega_{p,2}$ [rad s^{-1}]	L_1 [H]	L_2 [H]
10	245.06	1.43×10^3	0.103	0.176
12	235.26	1.22×10^3	0.108	0.177
14	226.49	1.09×10^3	0.113	0.173
16	221.51	1.04×10^3	0.115	0.173
18	220.65	1.03×10^3	0.117	0.177
20	219.62	1.03×10^3	0.117	0.182
22	221.72	1.04×10^3	0.117	0.180
24	219.09	1.01×10^3	0.120	0.180
26	223.05	1.03×10^3	0.120	0.185

Table 2.1: Multi-branch electrical circuit model parameters for experimental data in 45° configuration.

In addition, to obtain a single offset value that applies to all air gaps, and to both forces, the combined error (of the lift and drag forces) is averaged across all contributing nominal air gaps. Applying the resulting value to the lift force and drag force fitted to the FEM data, and comparing the curves with respect to the experimental data, an agreeable match is noted in Figures 2.6 and 2.7.

To verify the procedure in identifying the unique offsets, the FEM model is exploited. Figures 2.8 and 2.9 highlight comparisons for different selections of the air gap offset imposed in the model, for a nominal air gap of 10 mm for the lift and drag force respectively. Observed in Figure 2.8a, the data obtained from COMSOL Multiphysics® presents a satisfactory fit with the experimental data, for an imposed (unique) offset of 1.37 mm, corresponding to that calculated from the combined error of the lift and drag force. Figure 2.8b indicates the FEM data stemming from the imposition of the unique offset of 1.11 mm calculated from only the drag force error, and as expected presents a less adequate fit. The converse of these observations is evident in Figures 2.9a and 2.9b, regarding the drag force. The offset calculated prioritising the drag force presents curves that fit more closely with the experimental data. A further improvement in the fit is achieved through an estimation of a lower offset value that presents the most satisfactory match for the experimental drag force data, for the nominal air gap of 10 mm, evident in Figure 2.10. However, it is advised to remain within the limits of the offsets computed using the RMS error, as further improvements by means of estimation may prove time-consuming.

To generate lift and drag force data in static conditions as a function of longitudinal velocity in COMSOL Multiphysics®, the air gap offset approximating all contributing irregularities is imposed. The resulting data generated serves as an

Air gap [mm]	$\omega_{p,k}$ [rad s^{-1}]	L_k [H]
10	$\omega_{p,1} = 195.90$	$L_1 = 0.112$
	$\omega_{p,2} = 792.19$	$L_2 = 0.128$
	$\omega_{p,3} = 3.99 \times 10^3$	$L_3 = 9.48 \times 10^6$
12	$\omega_{p,1} = 195.93$	$L_1 = 0.116$
	$\omega_{p,2} = 785.70$	$L_2 = 0.134$
	$\omega_{p,3} = 3.76 \times 10^3$	$L_3 = 3.68 \times 10^7$
14	$\omega_{p,1} = 196.21$	$L_1 = 0.121$
	$\omega_{p,2} = 779.25$	$L_2 = 0.140$
	$\omega_{p,3} = 3.85 \times 10^3$	$L_3 = 2.92 \times 10^7$
16	$\omega_{p,1} = 195.38$	$L_1 = 0.125$
	$\omega_{p,2} = 768.22$	$L_2 = 0.144$
	$\omega_{p,3} = 4.15 \times 10^3$	$L_3 = 2.32 \times 10^7$
18	$\omega_{p,1} = 195.35$	$L_1 = 0.128$
	$\omega_{p,2} = 761.13$	$L_2 = 0.147$
	$\omega_{p,3} = 4.29 \times 10^3$	$L_3 = 1.82 \times 10^5$
20	$\omega_{p,1} = 195.09$	$L_1 = 0.131$
	$\omega_{p,2} = 752.84$	$L_2 = 0.150$
	$\omega_{p,3} = 4.30 \times 10^3$	$L_3 = 1.43 \times 10^7$
22	$\omega_{p,1} = 195.09$	$L_1 = 0.134$
	$\omega_{p,2} = 745.38$	$L_2 = 0.152$
	$\omega_{p,3} = 4.71 \times 10^3$	$L_3 = 1.12 \times 10^7$
24	$\omega_{p,1} = 195.26$	$L_1 = 0.136$
	$\omega_{p,2} = 739.34$	$L_2 = 0.153$
	$\omega_{p,3} = 5.22 \times 10^3$	$L_3 = 1.72 \times 10^6$
26	$\omega_{p,1} = 195.35$	$L_1 = 0.137$
	$\omega_{p,2} = 732.73$	$L_2 = 0.152$
	$\omega_{p,3} = 5.74 \times 10^3$	$L_3 = 6.58 \times 10^6$

Table 2.2: Results after fitting multi-branch electrical circuit model to COMSOL data in 45° configuration.

approximation for the lift and drag forces that are present on the test bench for the Halbach array configuration. To represent these forces more accurately, individual air gap offsets for each nominal air gap are suggested to be imposed in the FEM model.

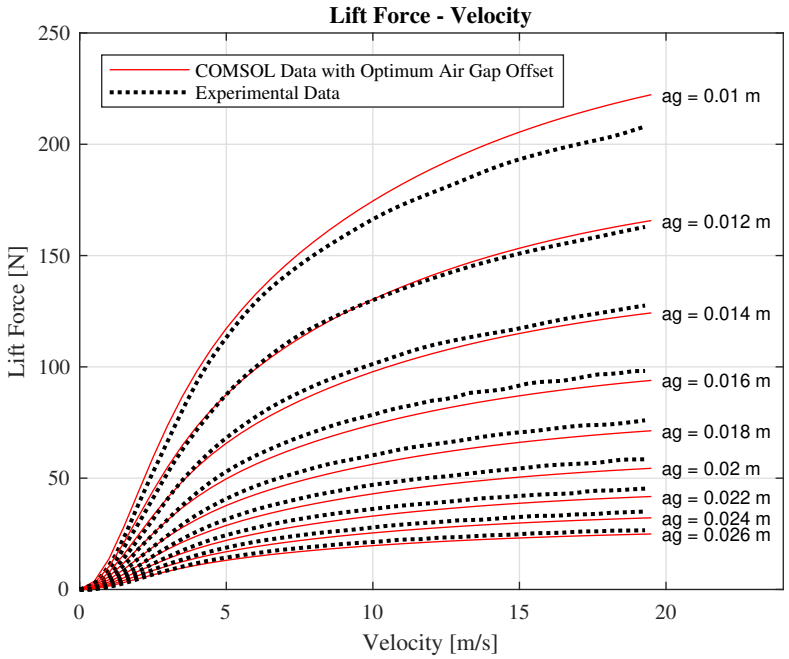

Figure 2.6: Lift force fitted to a set of experimental data for nominal air gaps by means of a single air gap offset obtained from minimisation of averaged RMS error across all gaps for 45° configuration.

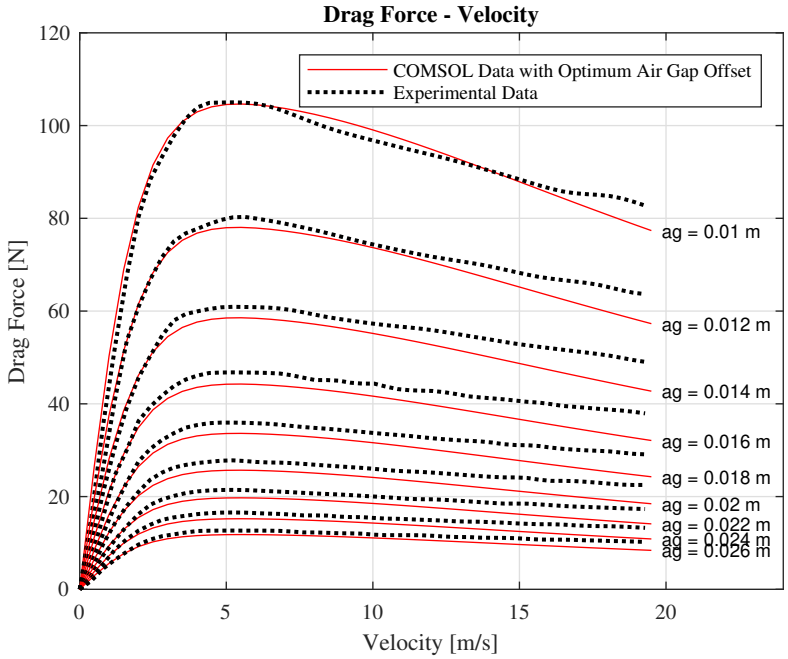

Figure 2.7: Drag force fitted to a set of experimental data for nominal air gaps by means of a single air gap offset obtained from minimisation of averaged RMS error across all gaps for 45° configuration.

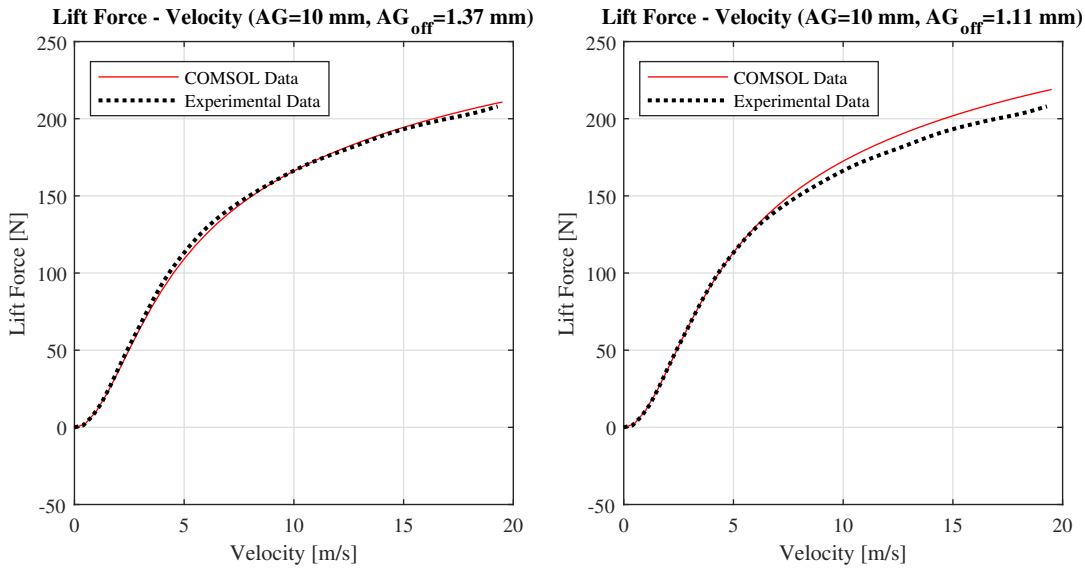

(a) FEM data obtained imposing an air gap offset of 1.37 mm for the lift force.

(b) FEM data obtained imposing an air gap offset of 1.11 mm for the lift force.

Figure 2.8: FEM data for the lift force fitted to experimental data at a nominal air gap of 10 mm and at different offsets.

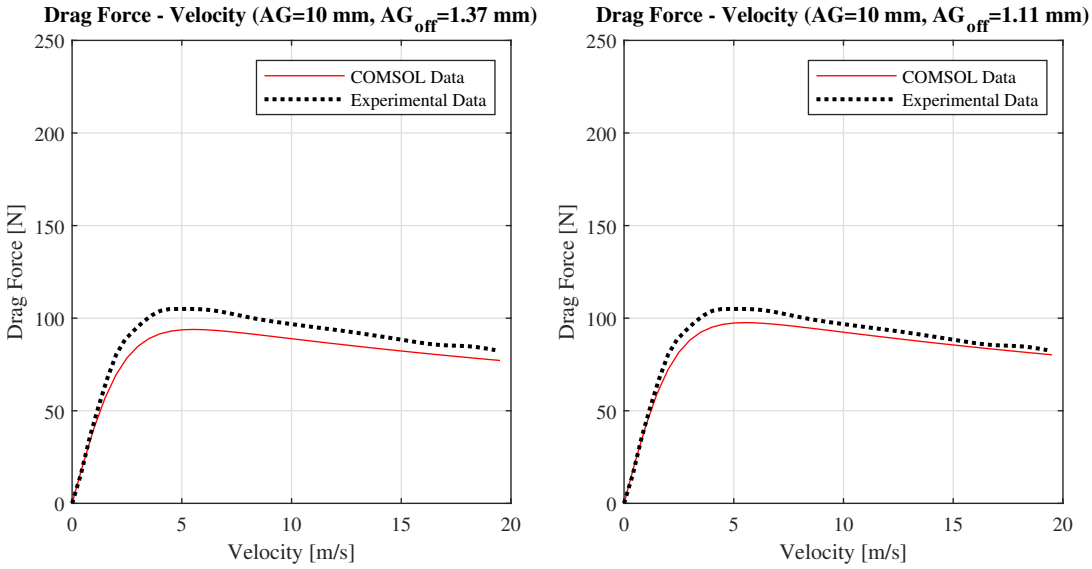

(a) FEM data obtained imposing an air gap offset of 1.37 mm for the drag force.

(b) FEM data obtained imposing an air gap offset of 1.11 mm for the drag force.

Figure 2.9: FEM data for the drag force fitted to experimental data at a nominal air gap of 10 mm and at different offsets.

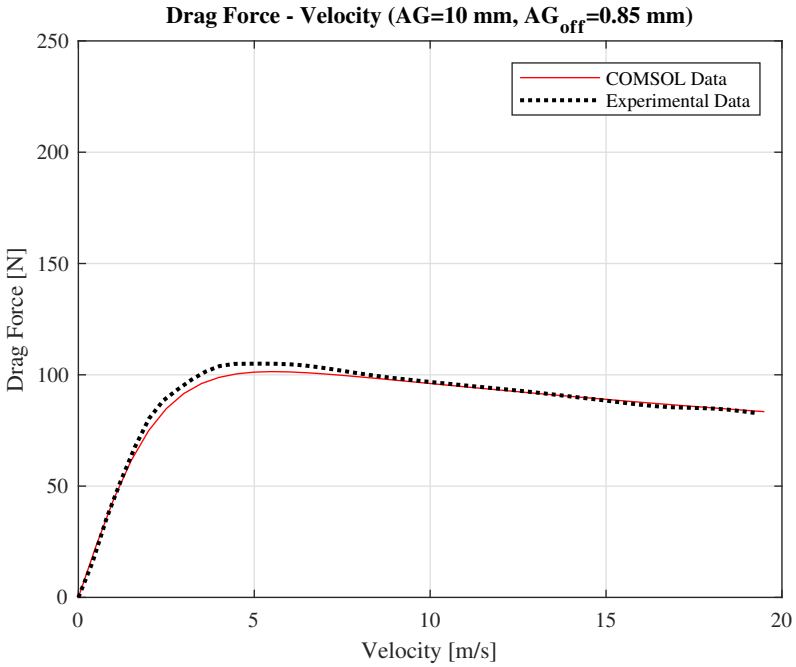

Figure 2.10: FEM data for the drag force fitted to experimental data at a nominal air gap of 10 mm and at a further improved estimate for the offset.

2.1.2 90° configuration

The magnetisation scheme pertaining to this Halbach array may be noted in Figure 2.11 as proposed in [5]. The parameters for numerical generation of the forces necessary for the computation of the offsets are reported in Tables 2.3 and 2.4. To initialise the 3D FEM model, the magnet array's remanence flux $B_r = 1.44\,\mathrm{T}$ while the recoil permeability $\mu_{pm} = 1.05$. The remanence flux differs slightly due to the difference in material composition between the two arrays of interest. The magnet side length is 12 mm, and the number of magnets per pole pair is 4, meaning that the magnetic pole pair pitch ratio γ is different for this array.

An analogous procedure is applied to this configuration, with a set of offset values obtained for each nominal air gap seen in Figures 2.12 and 2.13. Additionally, the offsets obtained for each air gap are reported in Figure 2.14. Note that, as in the case of the 45° configuration, the points on this plot are not joined due to lack of motivation for a correlation between the optimal air gap offset, and the nominal air gap. The plot in Figure 2.4 may suggest a correlation, with the lower offset at higher air gaps implying a lower effect of irregularities on the experimental data. The same cannot be suggested for the plot concerning the 90° configuration, as the points appear to have a distribution that does not present a regularity in its

behaviour. A possible reason may be that inconsistencies in the experimental setup influence the data, requiring a significantly different offset to be applied to the FEM model to capture more accurately the static behaviour. It may be noted that a general decreasing trend can be identified, if the offsets for the air gaps of 12 mm and 24 mm are considered anomalies and are removed. A verification of the offsets calculated for this configuration is executed, by simulating the data corresponding to the nominal air gap of 12 mm, whose plots are present in Figures 2.18 and 2.19. The curves present satisfactory fits, confirming the robustness of the method in identifying the unique air gap offset required to replicate the experimental system's behaviour with a FEM model. A further lack of correlation may be observed in the plot in Figure 2.15 for the weighting of the two forces, concerning the combined error, however this may be attributed once again to the potentially subjective nature of the experimental data.

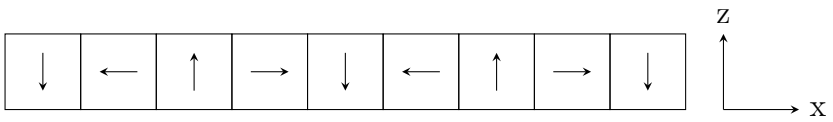

Figure 2.11: Magnetisation scheme for Halbach array in 90° configuration (cross-sectional view).

Air gap [mm]	$\omega_{p,1}$ [rad s^{-1}]	$\omega_{p,2}$ [rad s^{-1}]	L_1 [H]	L_2 [H]
10	649.10	3.88×10^3	0.0904	0.115
12	592.28	3.06×10^3	0.0826	0.103
14	576.54	2.79×10^3	0.0900	0.111
16	560.58	2.69×10^3	0.0837	0.103
18	544.48	2.56×10^3	0.0800	0.0954
20	549.12	2.58×10^3	0.0730	0.0908
22	517.47	2.32×10^3	0.0689	0.0832
24	507.69	2.23×10^3	0.0715	0.0879
26	506.22	2.17×10^3	0.0547	0.0685

Table 2.3: Multi-branch electrical circuit model parameters for experimental data in 90° configuration.

Air gap [mm]	$\omega_{p,k}$ [rad s^{-1}]	L_k [H]
10	$\omega_{p,1} = 319.93$	$L_1 = 0.347$
	$\omega_{p,2} = 651.51$	$L_2 = 0.0.106$
	$\omega_{p,3} = 2.51 \times 10^3$	$L_3 = 0.0999$
12	$\omega_{p,1} = 297.66$	$L_1 = 0.418$
	$\omega_{p,2} = 624.83$	$L_2 = 0.0996$
	$\omega_{p,3} = 2.47 \times 10^3$	$L_3 = 0.0982$
14	$\omega_{p,1} = 330.37$	$L_1 = 0.319$
	$\omega_{p,2} = 637.57$	$L_2 = 0.103$
	$\omega_{p,3} = 2.47 \times 10^3$	$L_3 = 0.0971$
16	$\omega_{p,1} = 494.79$	$L_1 = 0.0827$
	$\omega_{p,2} = 2.19 \times 10^3$	$L_2 = 0.0855$
	$\omega_{p,3} = 7.69 \times 10^3$	$L_3 = 3.09 \times 10^4$
18	$\omega_{p,1} = 488.35$	$L_1 = 0.0784$
	$\omega_{p,2} = 2.15 \times 10^3$	$L_2 = 0.0818$
	$\omega_{p,3} = 8.83 \times 10^3$	$L_3 = 4.25 \times 10^5$
20	$\omega_{p,1} = 481.28$	$L_1 = 0.0734$
	$\omega_{p,2} = 2.10 \times 10^3$	$L_2 = 0.0772$
	$\omega_{p,3} = 9.02 \times 10^3$	$L_3 = 8.01 \times 10^4$
22	$\omega_{p,1} = 474.27$	$L_1 = 0.0678$
	$\omega_{p,2} = 2.05 \times 10^3$	$L_2 = 0.0718$
	$\omega_{p,3} = 9.52 \times 10^3$	$L_3 = 1.76 \times 10^4$
24	$\omega_{p,1} = 471.38$	$L_1 = 0.0615$
	$\omega_{p,2} = 2.02 \times 10^3$	$L_2 = 0.0663$
	$\omega_{p,3} = 9.37 \times 10^3$	$L_3 = 5.42 \times 10^4$
24	$\omega_{p,1} = 465.67$	$L_1 = 0.0551$
	$\omega_{p,2} = 1.97 \times 10^3$	$L_2 = 0.0599$
	$\omega_{p,3} = 8.93 \times 10^3$	$L_3 = 1.94 \times 10^5$

Table 2.4: Results after fitting multi-branch electrical circuit model to COMSOL data in 90° configuration.

The single offset generated by considering the combined error, and an average of said error over all air gaps, yields satisfactory plots for the forces in Figures 2.16 and 2.17, when compared to the experimental data. As concluded for the previous configuration, the single offset remains a convenient parameter to approximate the forces generated for each air gap in the FEM model, however more accurate results can be obtained by imposing individual optimal offsets.

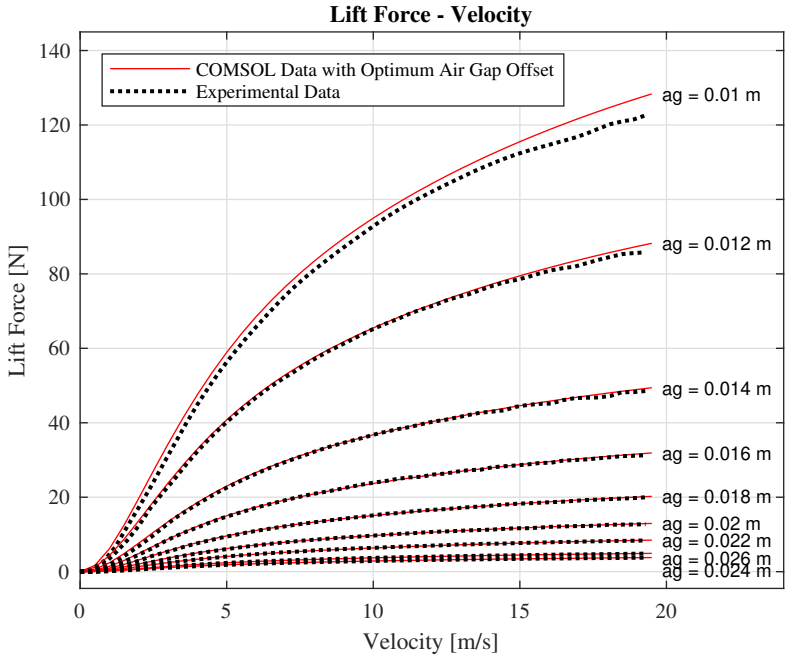

Figure 2.12: Lift force fitted to a set of experimental data for nominal air gaps by means of unique air gap offsets obtained from minimisation of squared error for 90° configuration.

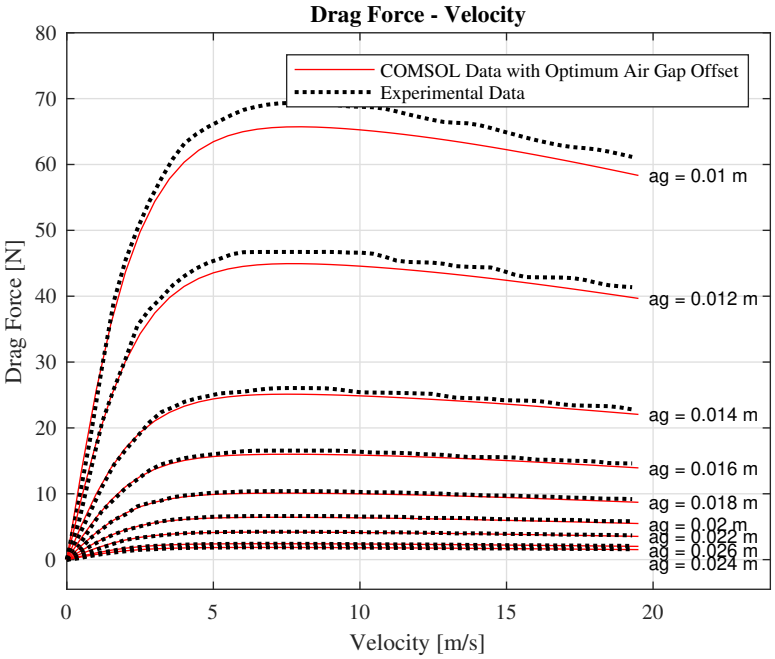

Figure 2.13: Drag force fitted to a set of experimental data for nominal air gaps by means of unique air gap offsets obtained from minimisation of squared error for 90° configuration.

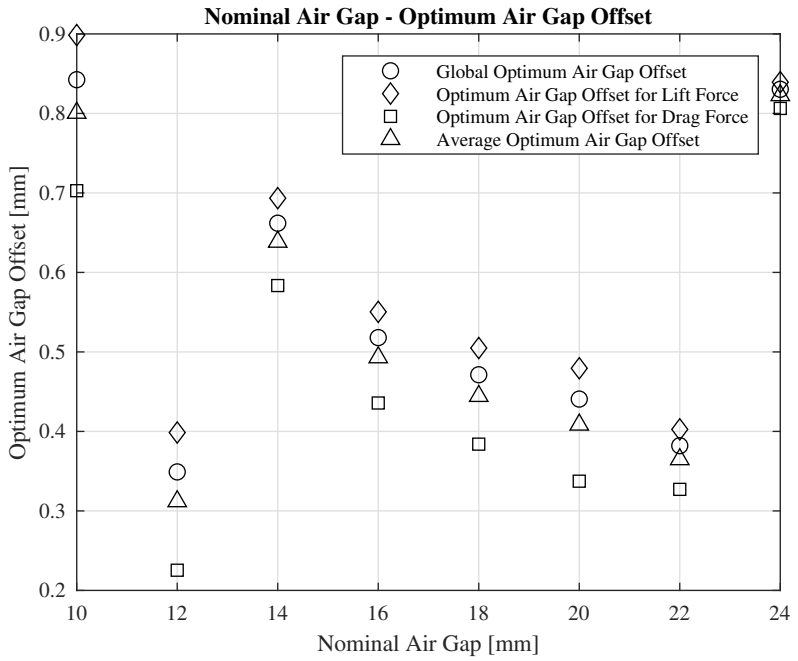

Figure 2.14: Optimum air gap offsets for each nominal air gap, dependent on the error used for computation regarding 90° configuration.

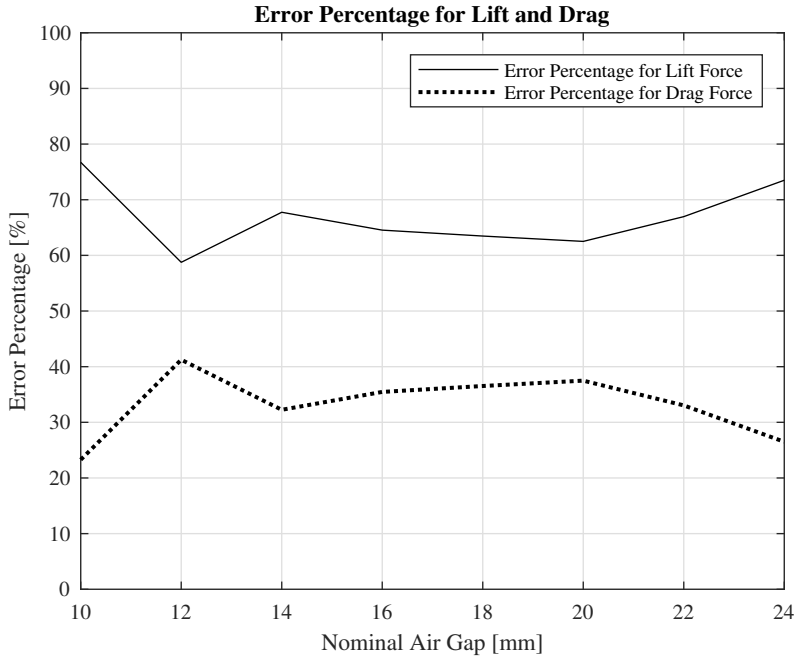

Figure 2.15: Percentage of combined error for lift and drag force, for each nominal air gap, in the identification of unique air gap offsets for 90° configuration.

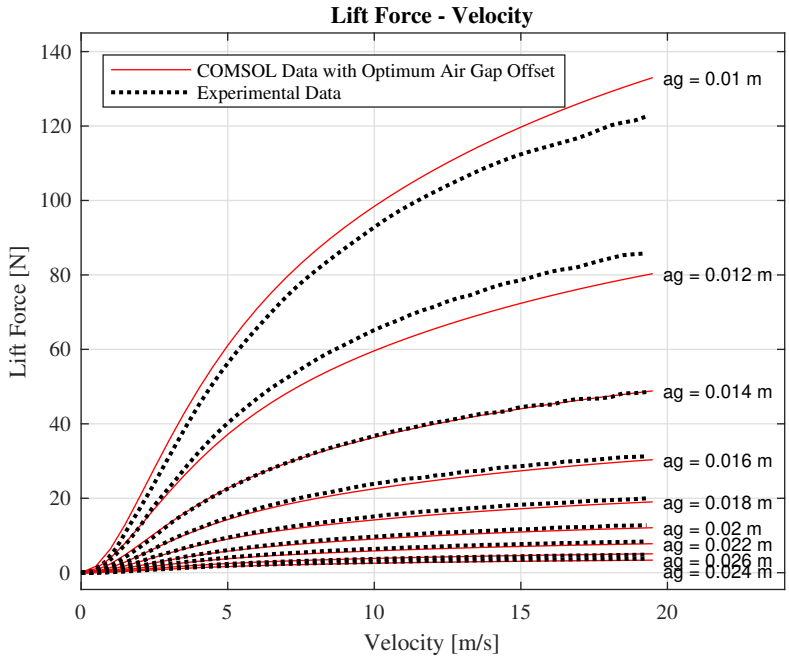

Figure 2.16: Lift force fitted to a set of experimental data for nominal air gaps by means of a single air gap offset obtained from minimisation of averaged squared error across all gaps for 90° configuration.

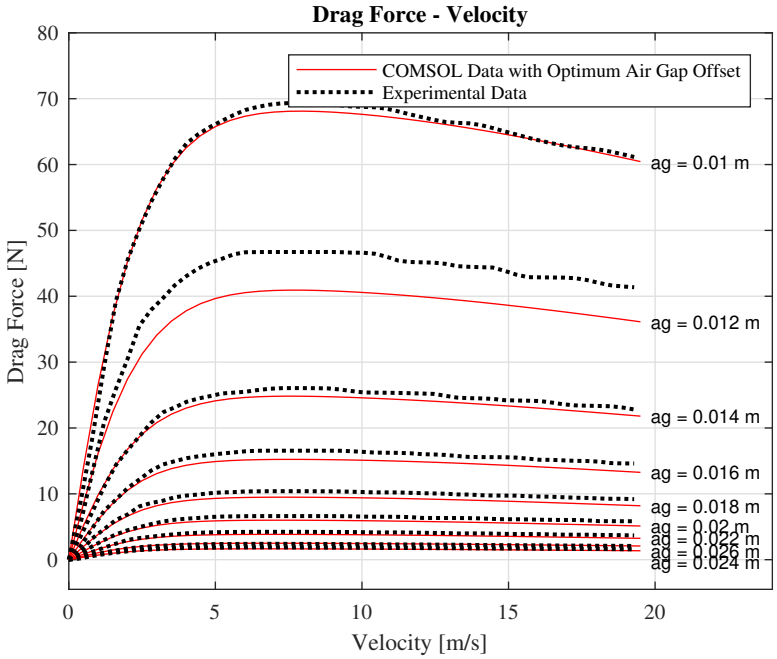

Figure 2.17: Drag force fitted to a set of experimental data for nominal air gaps by means of a single air gap offset obtained from minimisation of averaged squared error across all gaps for 90° configuration.

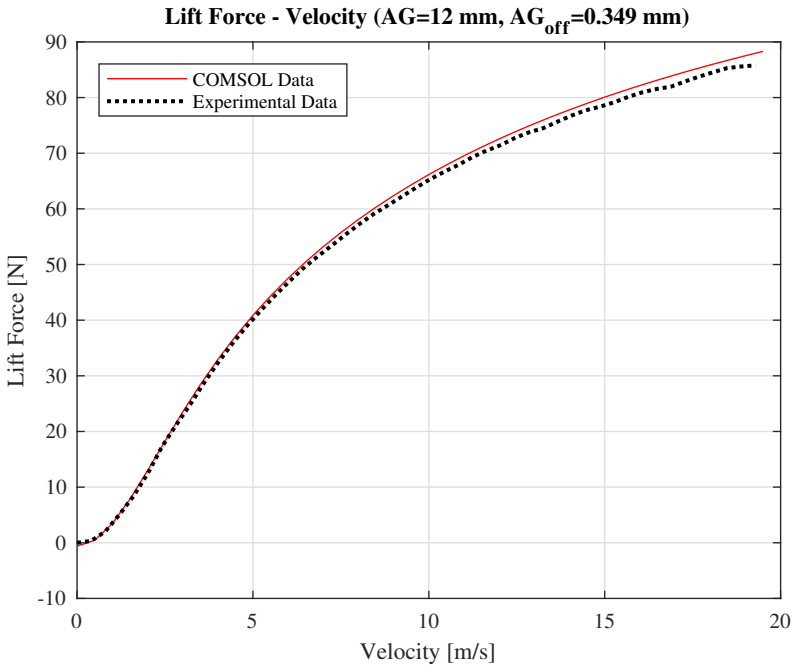

Figure 2.18: FEM data for the lift force fitted to experimental data at a nominal air gap of 12 mm at an offset of 0.349 mm for 90° configuration.

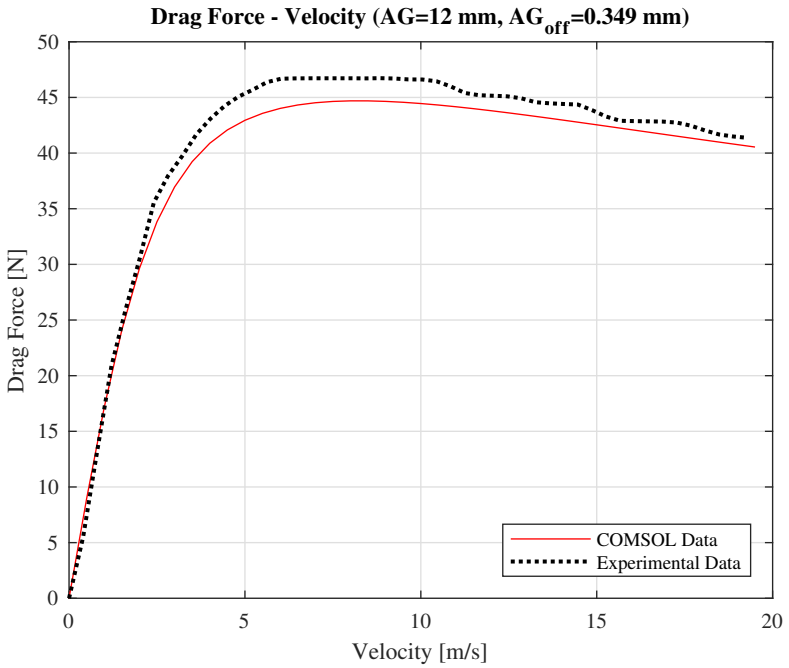

Figure 2.19: FEM data for the drag force fitted to experimental data at a nominal air gap of 12 mm at an offset of 0.349 mm for 90° configuration.

Chapter 3

Conventional Control Strategies

3.1 Skyhook Control

An initial attempt in implementing a control strategy on the system involves the well-known skyhook damping, an imaginary parameter that appears explicitly in the equations of motion [6] of the quarter-car model found in section A.1 of the Appendix. This damping action is attached solely to the sprung mass, with the intention to maximise passenger comfort. A schematic of the system is represented in Figure 3.1. The analysis on the feasibility of this control method proceeds firstly with a study on the most suitable combination of skyhook damping, c_{sky}, and suspension damping, c_s, such that the system is most stable. For every value of longitudinal velocity, and for a set of skyhook and suspension damping values, the poles of the system with the instability (lumped parameter model coupled with equations of motion) are extracted. For each combination, the most positive pole is recorded, allowing for a colour map to be plotted, evident in Figure 3.2. It can be noted that with an increasing longitudinal velocity, the well of stability diminishes, notably for lower values of c_s, hence analysing the colour map pertaining to the highest velocity is acceptable to highlight the pair of c_s and c_{sky} that present the most stable behaviour as it ensures the most conservative selection. Nonetheless, the presence of a narrow band of stability allows for the identification of a set of couples of c_s and c_{sky} such that the real part of the largest negative pole of the dynamic matrix is furthest from the origin.

As a secondary analysis, the dynamic response of the system is obtained by means of a Simulink® model. Two responses are compared, one where an adequately stable pair of c_s and c_{sky} are used, and another where c_{sky} is null representing the most

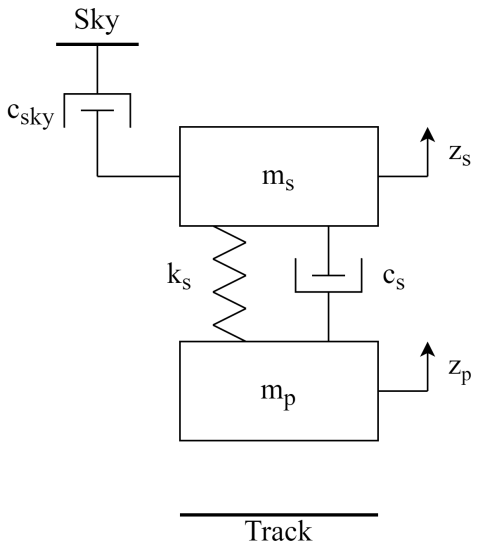

Figure 3.1: Quarter-car model of electrodynamically levitated pod with skyhook control.

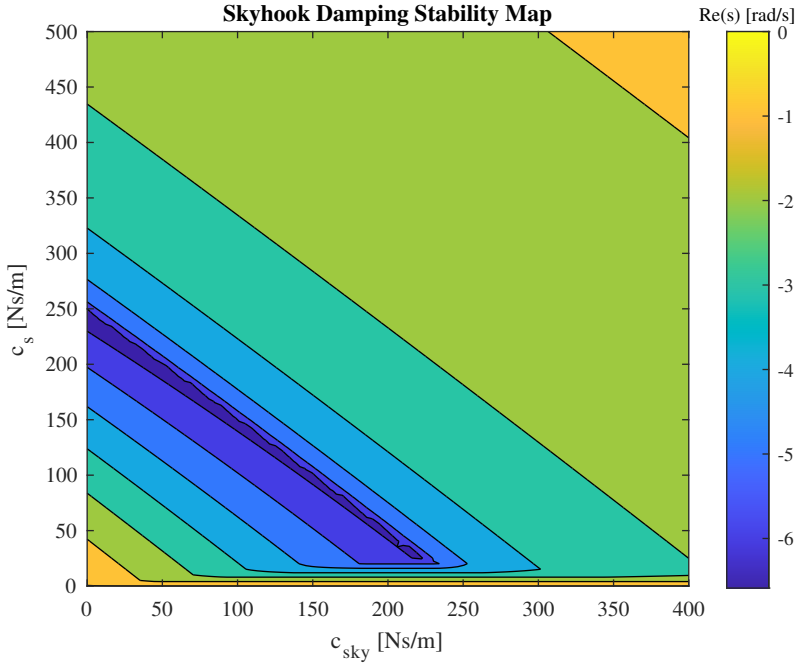

Figure 3.2: Stability map for skyhook damping coupled with suspension damping.

stable case, with time domain plots of the unsprung mass displacement and sprung mass acceleration. The excitation profile is chosen to be sinusoidal, with all relevant parameters for the study of skyhook control as well as the subsequent conventional control studies reported in Table 3.1. The sprung mass acceleration for the two configurations is compared in Figure 3.3, with Figure 3.3a denoting the response for the configuration improving passenger comfort and Figure 3.3b indicating the system's behaviour with the most stable choice of damping parameters. Likewise, the unsprung mass displacement is compared in Figure 3.4, with Figures 3.4a and 3.4b highlighting the behaviours of the two aforementioned configurations. A notably higher magnitude for the unsprung mass displacement is observed for the non-zero skyhook damping case, as a significantly lower suspension damping is implemented.

Parameter	Value	Units
A_R	0.5	mm
v	340	$^{\mathrm{m}}/_{\mathrm{s}}$
ω	100	$\mathrm{rad\,s^{-1}}$
x_0	600	m
m_s	20	kg
m_p	2	kg
γ	0.0159	m
k_s	789.57	$\mathrm{N\,m^{-1}}$
Λ_0	3.29×10^{-4}	Wb
L_1	7.72×10^{-10}	H
L_2	2.06×10^{-9}	H
L_3	4.12×10^{-9}	H
$\omega_{p,1}$	355.45	$\mathrm{rad\,s^{-1}}$
$\omega_{p,2}$	2.57×10^{3}	$\mathrm{rad\,s^{-1}}$
$\omega_{p,3}$	1.73×10^{4}	$\mathrm{rad\,s^{-1}}$

Table 3.1: Parameters used in the study of conventional control strategies.

Furthermore, the bode diagrams for the receptance of the system incorporating the two pairs of c_s and c_{sky} are displayed in Figures 3.5a and 3.5b, in Figure 3.5. The bode diagrams for the comparison of the inertance are present in Figure 3.6, with Figures 3.6a and 3.6b reporting the responses of the two system configurations. It is evident that with the combination of c_s and non-null c_{sky}, the unsprung mass displacement is not controlled, however the sprung mass acceleration presents a lower magnitude compared to that of the null skyhook damping case. Furthermore, it must be noted that the pair of c_s and c_{sky} that provide a superior condition for passenger comfort yield a real part of the largest pole (closest to the origin) approximately

equal to -6.1 $\mathrm{rad\,s^{-1}}$, when imposed in the dynamic matrix. Conversely, the case with null skyhook damping remains the most stable, with the real part of the pole approximately equal to -6.59 $\mathrm{rad\,s^{-1}}$. The results of this comparison confirm that a combination of c_s and c_{sky} can be implemented in the system, improving passenger comfort, while conserving the system's stability.

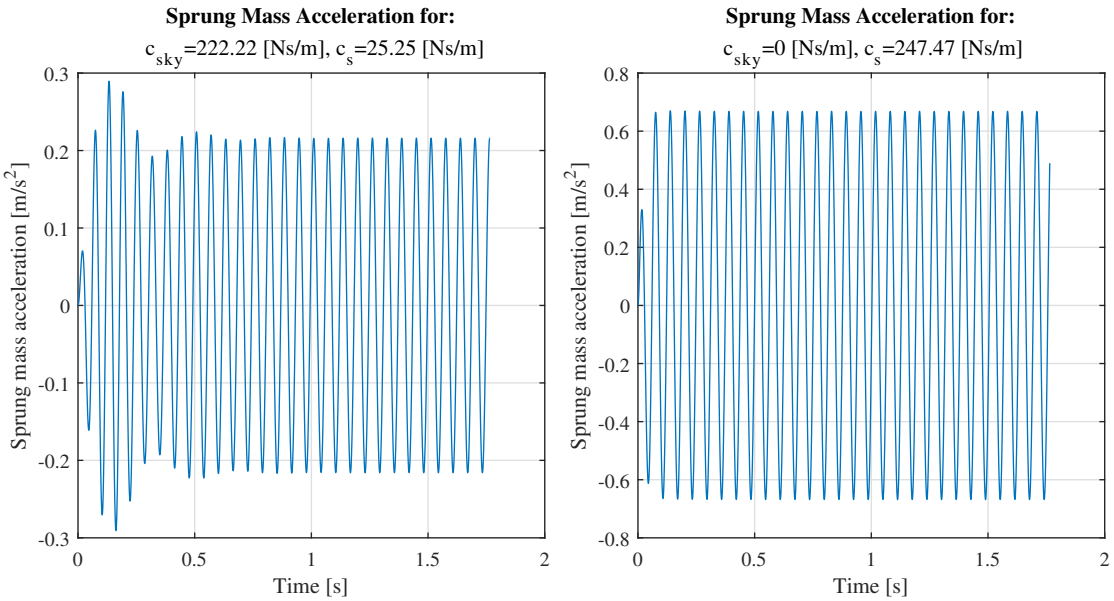

(a) Sprung mass acceleration for configuration improving comfort

(b) Sprung mass acceleration for most stable configuration

Figure 3.3: Sprung mass acceleration for different configurations of c_s and c_{sky}.

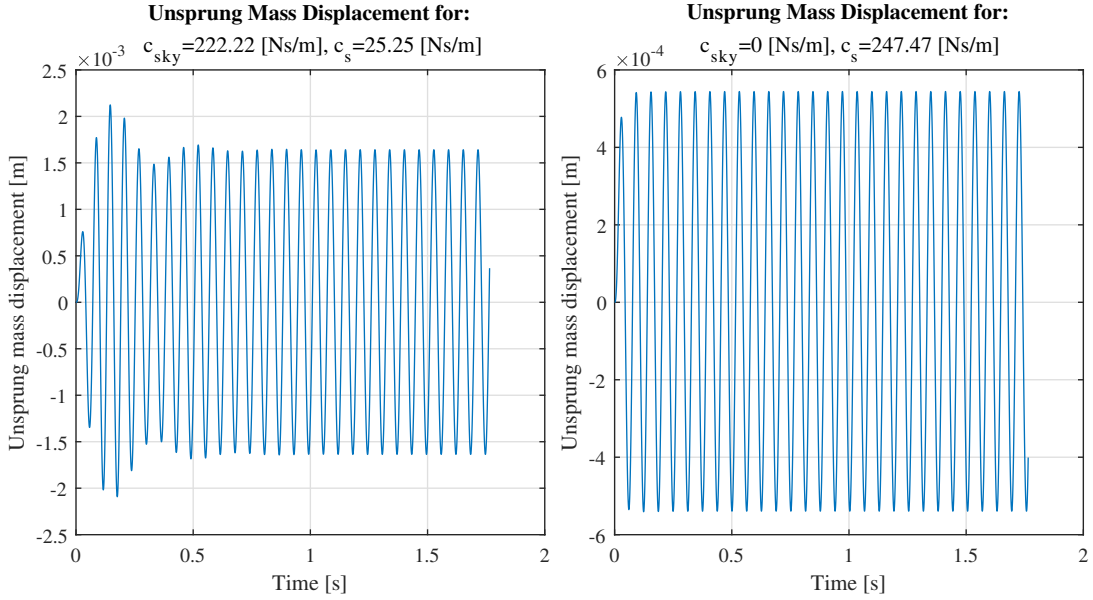

(a) Unsprung mass displacement for configuration improving comfort

(b) Unsprung mass displacement for most stable configuration

Figure 3.4: Unsprung mass displacement for different configurations of c_s and c_{sky}.

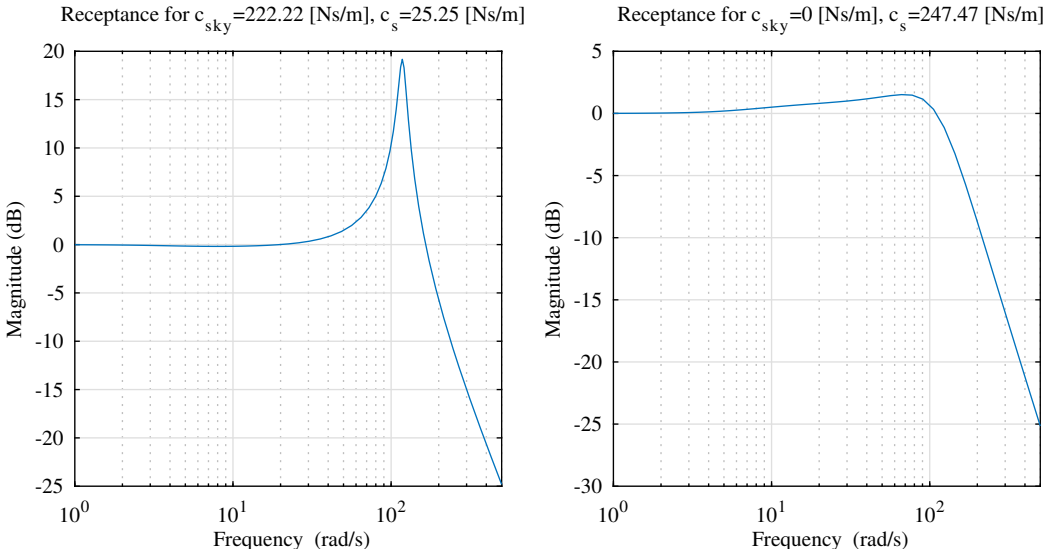

(a) Receptance for configuration improving comfort

(b) Receptance for most stable configuration

Figure 3.5: Receptance for different configurations of c_s and c_{sky}.

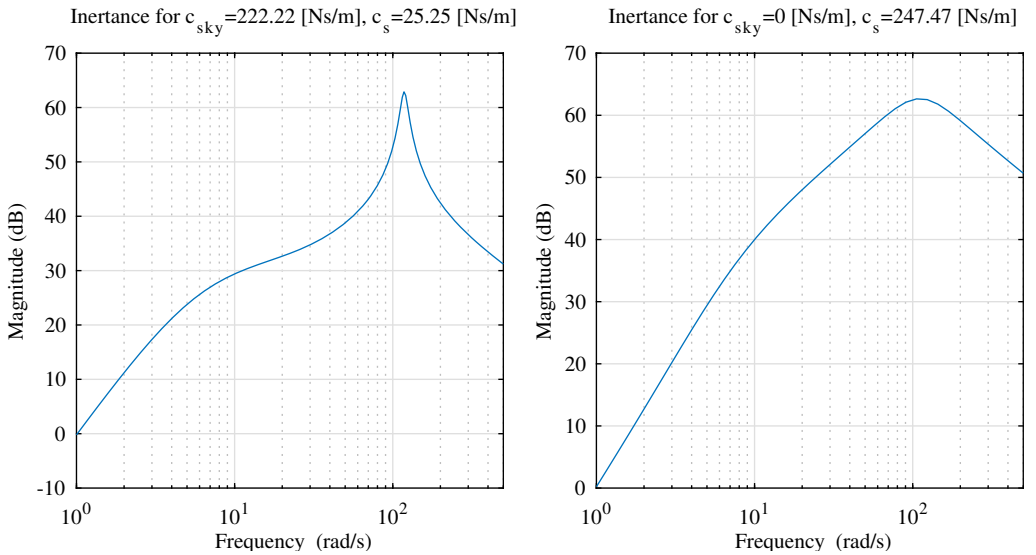

(a) Inertance for configuration improving comfort

(b) Inertance for most stable configuration

Figure 3.6: Inertance for different configurations of c_s and c_{sky}.

3.2 Groundhook Control

A shift in focus is introduced in the consideration of handling as opposed to passenger comfort. While skyhook damping acts only on the sprung mass, groundhook damping behaves analogously by targeting the unsprung mass alone [6], as illustrated in Figure 3.7. As in the case of skyhook damping, the stability of the system is analysed for combinations of c_s, and groundhook damping, c_{gr}, with an appropriate modification of the dynamic matrix found in section A.2 of the Appendix. The colour map obtained in Figure 3.8 from the analysis corresponds to that of the highest velocity, motivated by the same behaviour observed in the case of skyhook damping. Discrete regions of stability are illustrated, however with a much weaker dependency of c_{gr} with respect to c_s. A well of maximum stability is nonetheless identifiable, from which a pair of c_s and c_{gr} are extracted. For comparison, another pair close to the region of maximum stability are extracted from the map, with a larger value of groundhook damping.

The dynamic responses in terms of unsprung mass displacement and sprung mass acceleration are obtained from a corresponding Simulink® model, with identical excitation parameters as those implemented for the skyhook damping analysis. The time domain responses for the sprung mass acceleration are compared in Figures 3.9a and 3.9b of Figure 3.9, while those of the unsprung mass displacement are presented in Figures 3.10a and 3.10b of Figure 3.10. Given that c_s is almost invariant with respect to c_{gr} for regions of stability with similar real pole components, it is expected and indeed evidenced in the time domain plots that in the case of a larger value of c_{gr}, the unsprung mass displacement is lower. The sprung mass acceleration is also marginally lower in the case of a larger c_{gr}, due to the minimisation of vibrations transmitted from the unsprung mass to the sprung mass via the intermediate suspension.

The bode diagrams representing the receptance are compared in Figures 3.11a and 3.11b of Figure 3.11, while those for the inertance are compared in Figures 3.12a and 3.12b of Figure 3.12. It is clear that with a larger groundhook damping coefficient, the magnitude of the response for the displacement is expected to be lower compared to that of a lower c_{gr} value. This confirms improved handling, and it must be noted that in the case of a larger c_{gr}, the system retains a real component value of the largest pole in the neighbourhood of those noted for maximum stability, approximately equal to -6.18 $\mathrm{rad\,s^{-1}}$. The real part of the largest pole for the most stable pair of c_s and c_{gr} is approximately equal to -7.6 $\mathrm{rad\,s^{-1}}$.

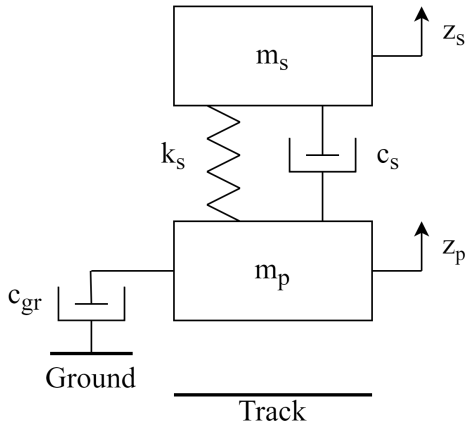

Figure 3.7: Quarter-car model of electrodynamically levitated pod with groundhook control.

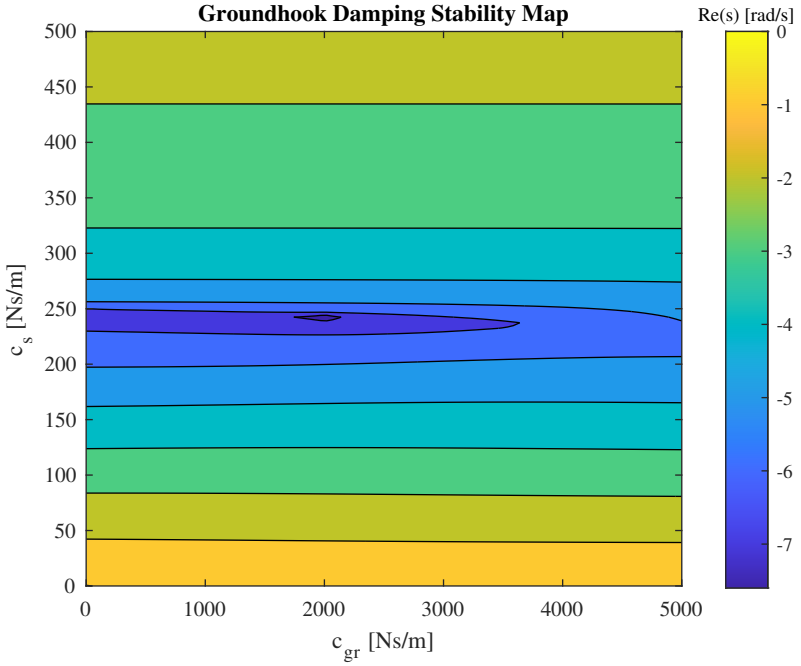

Figure 3.8: Stability map for groundhook damping coupled with suspension damping.

A further observation of the time domain responses confirms that the sprung mass acceleration presents a markedly reduced peak value compared to that of the skyhook damping case. A possible reason is that the value of c_{sky} is an order of magnitude lower than the value of c_{gr}, meaning that although groundhook damping targets handling, its larger value may also prevent oscillations from reaching the sprung mass. A brief investigation yields that a value of skyhook damping of comparable order presents a similar sprung mass acceleration response as that depicted for the groundhook damping case. A note of warning must be issued for the use of an increased value of c_{sky}, where the real component of the largest pole of the dynamic matrix is most certainly closer to the origin, therefore presenting an unsatisfactory stability condition.

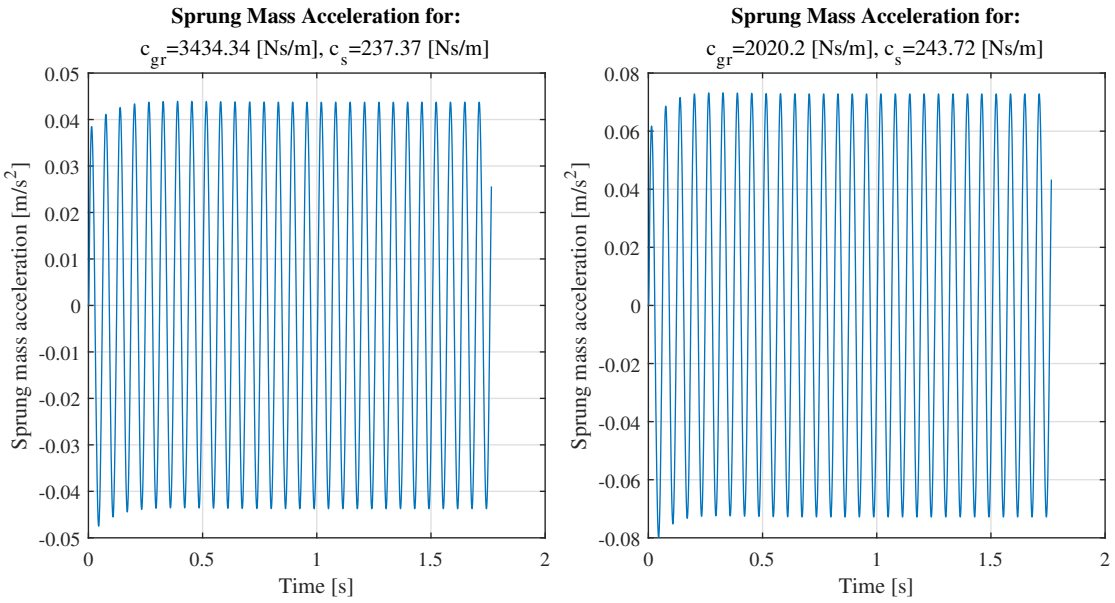

(a) Sprung mass acceleration for configuration improving handling

(b) Sprung mass acceleration for most stable configuration

Figure 3.9: Sprung mass acceleration for different configurations of c_s and c_{gr}.

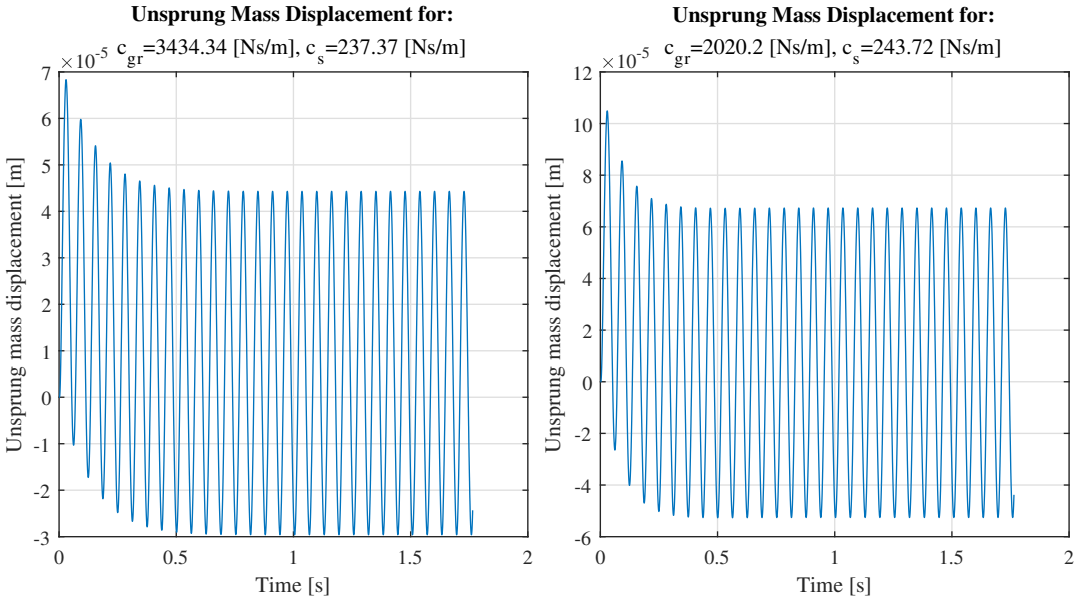

(a) Unsprung mass displacement for configuration improving handling

(b) Unsprung mass displacement for most stable configuration

Figure 3.10: Unsprung mass displacement for different configurations of c_s and c_{gr}.

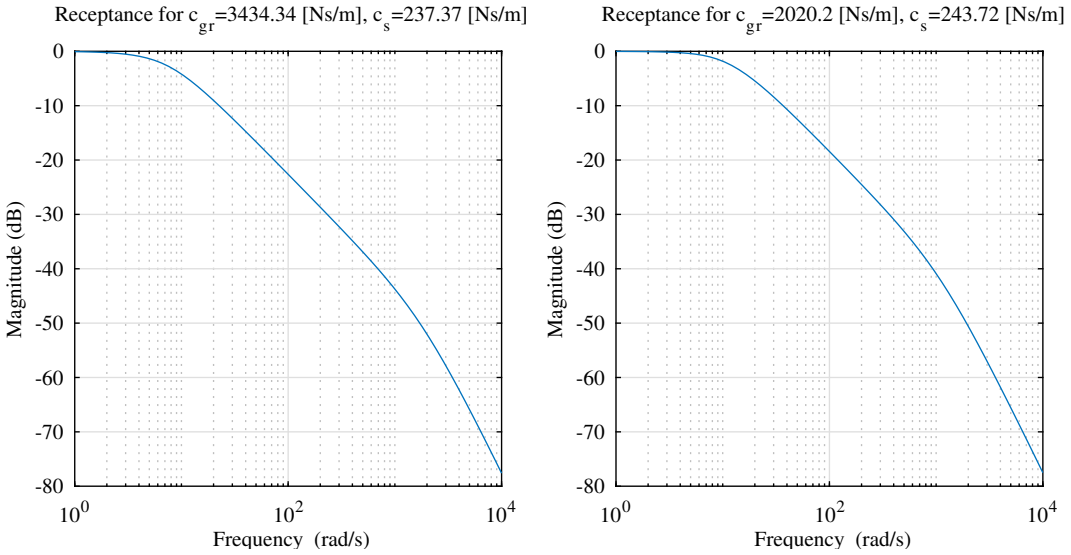

(a) Receptance for configuration improving handling

(b) Receptance for most stable configuration

Figure 3.11: Receptance for different configurations of c_s and c_{gr}.

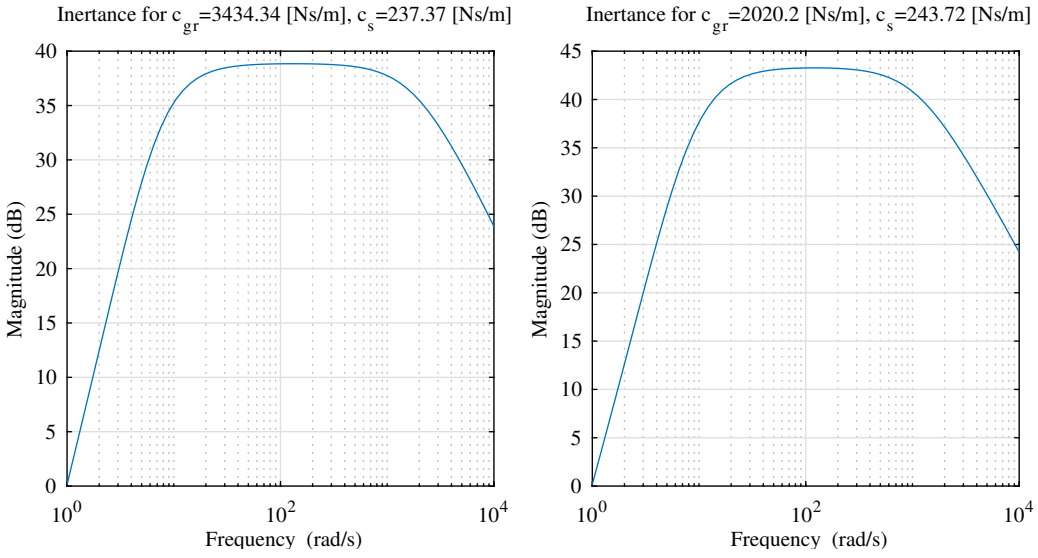

(a) Inertance for configuration improving handling

(b) Inertance for most stable configuration

Figure 3.12: Inertance for different configurations of c_s and c_{gr}.

3.3 Skyhook and Groundhook Control

The final analysis regarding conventional control strategies consists of a simultaneous action of both c_{sky} and c_{gr} as portrayed in Figure 3.13. Only one configuration is considered, with the selection of c_{sky} pertaining to the value providing a more favourable condition for passenger comfort, as outlined in subsection 3.1. Regarding c_{gr}, its value corresponds with that providing optimum stability for the system in subsection 3.2. The value of c_s is chosen in accordance with c_{sky}, as the primary intent remains to optimise passenger comfort. Modifying the dynamic matrix, present in section A.3 of the Appendix, the largest real part of the poles is approximately equal to -6.16 $\mathrm{rad\,s^{-1}}$, residing in the neighbourhood of the values observed during prior analyses.

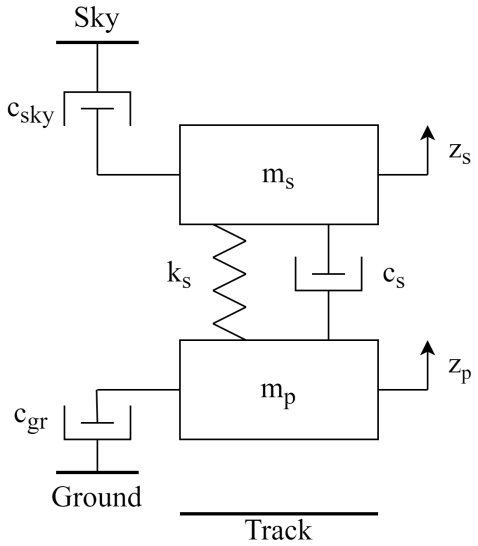

Figure 3.13: Quarter-car model of electrodynamically levitated pod with skyhook and groundhook control.

Regarding the dynamic response, time domain plots and bode diagrams reveal a superior performance of the system with the inclusion of both imaginary damping contributions, where the sprung mass acceleration and the unsprung mass displacement are lower when compared to all previous dynamic responses. The response regarding the sprung mass acceleration is indicated in Figure 3.14, while the unsprung mass displacement is reported in Figure 3.15. The bode plots for the receptance and inertance in Figures 3.16 and 3.17 respectively present notably reduced peaks in magnitude. To preserve consistency in the comparison, the input parameters such as the profile of the track and the velocity remain constant.

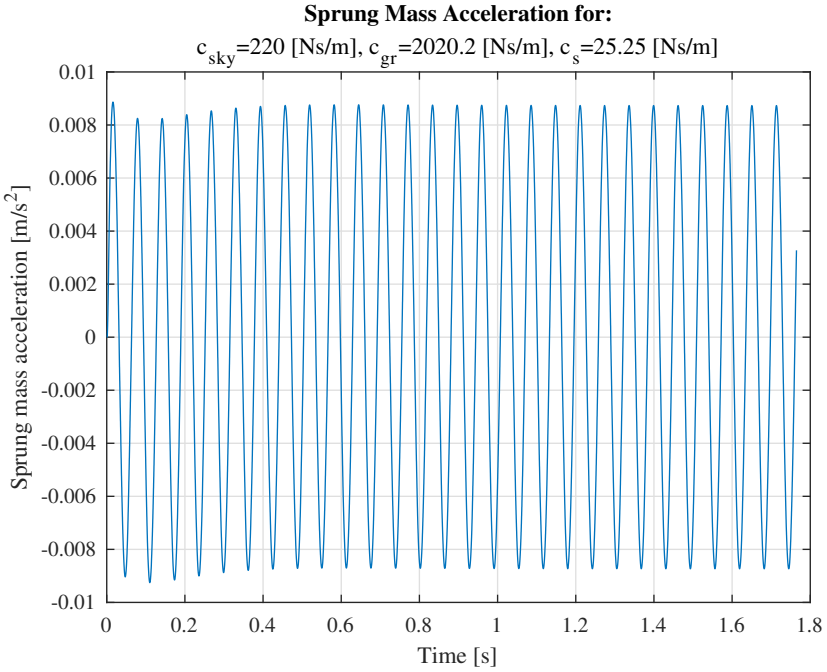

Figure 3.14: Sprung mass acceleration of configuration implementing a combination of c_{sky} and c_{gr}.

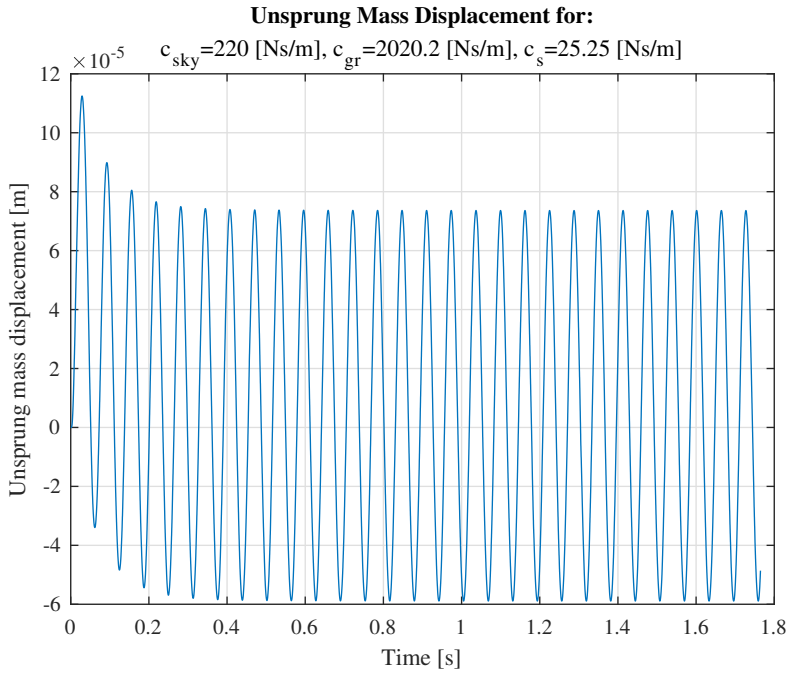

Figure 3.15: Unsprung mass displacement of configuration implementing a combination of c_{sky} and c_{gr}.

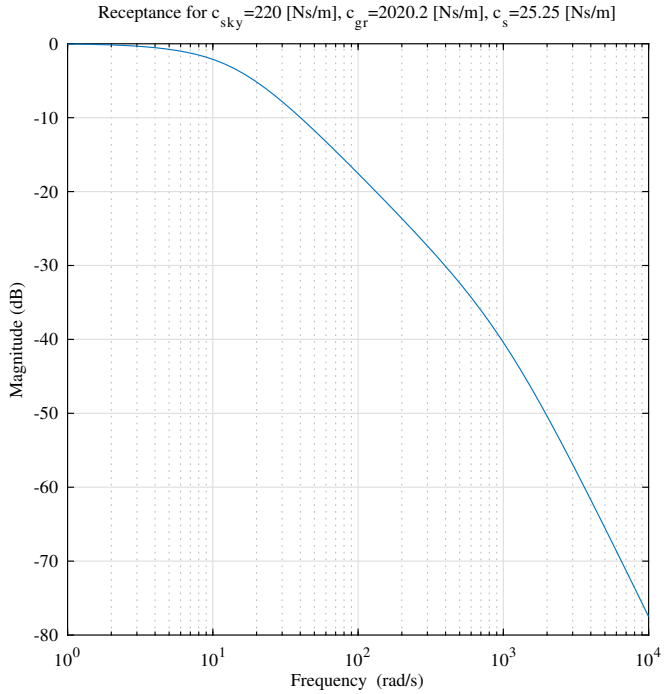

Figure 3.16: Receptance of configuration implementing a combination of c_{sky} and c_{gr}.

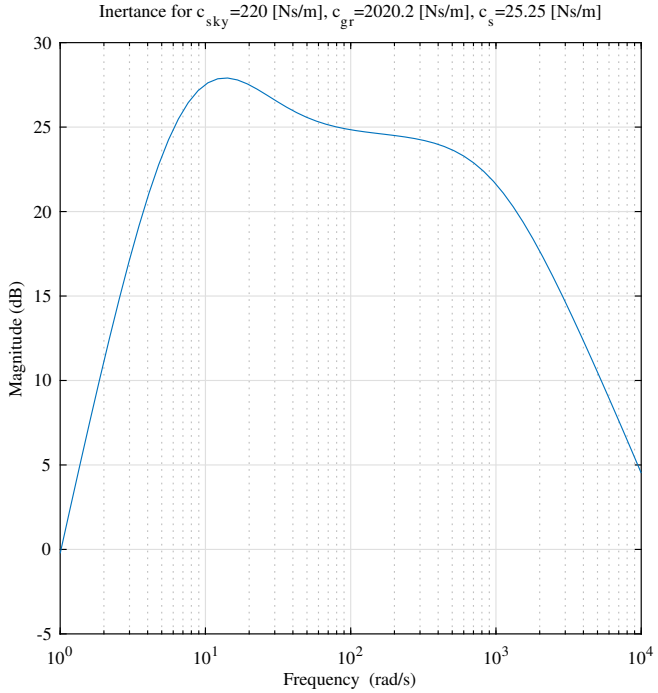

Figure 3.17: Inertance of configuration implementing a combination of c_{sky} and c_{gr}.

Chapter 4

Optimal Control Strategies

4.1 Excitation Profiles

4.1.1 Sinusoidal

Prior to the discussion concerning the Linear Quadratic Regulator, a further analysis is made on the various excitation profiles useful as inputs for the validation of the control strategy's performance. As in the case of the study concerning the implementation of skyhook and groundhook damping, the system's response due to a sinusoidal excitation profile is explored. In Simulink®, the sinusoidal input is introduced in temporal frequency, however the profile may also be expressed in spatial frequency [7] as reported in Equation 4.1. The passage from spatial to temporal frequency is outlined in Equation 4.2.

$$z_R(x) = A_R \sin(\Omega x) \tag{4.1}$$

$$\Omega x = \frac{2\pi}{\lambda} x = \frac{2\pi}{\lambda} vt = 2\pi \frac{v}{\lambda} t = \omega t \tag{4.2}$$

The study of a generic sinusoidal excitation profile is further refined by the introduction of characteristic parameters present on the HyperloopTT™ test track in Toulouse, France. The vertical profile excitations of the track comprise of mechanical loading, thermal loading, and the effects of the linear synchronous motor. The expression in spatial frequency is reported in Equation 4.3. Given that Simulink® requires a temporal frequency, appropriate modifications are made to the argument of the sine function prior to its numerical implementation for the study, as per the formulation in Equation 4.2.

$$Z_{HA} = Z_D \sin\left(\frac{2\pi}{\lambda_L} x\right) + Z_{\Delta T} \sin\left(\frac{2\pi}{\lambda_L} x\right) - \frac{Z_S}{\lambda_S} \operatorname{rem}\left(\frac{x}{\lambda_S}\right) - \frac{Z_S}{2} \tag{4.3}$$

4.1.2 Random

Random track irregularities represent a more accurate input profile, allowing for a realistic analysis of the control strategy. It is also possible to define a random track profile by means of a superposition of sinusoidal functions [7]. For a true random profile, the auto-correlation function is defined in terms of the one-sided PSD (a function of the wave number, analogous to the spatial frequency), and a cosine function with the wave number and a spatial shift as its argument, evident in Equation 4.4. For a null spatial shift, the auto-correlation function coincides with the variance of the random distribution describing the profile, indicated in Equation 4.5. Moreover, the variance can be approximated in discrete terms, by means of a summation of N power spectral densities dependent on N wave numbers, as seen in Equation 4.6.

$$R(\xi) = \int_0^\infty \Phi(\Omega)\cos(\Omega\xi)d\Omega \tag{4.4}$$

$$R(\xi = 0) = \sigma^2 = \int_0^\infty \Phi(\Omega)d\Omega \tag{4.5}$$

$$\sigma^2 \simeq \sum_{i=1}^{N} \Phi(\Omega_i)\Delta\Omega \tag{4.6}$$

$$\Delta\Omega = \frac{\Omega_N - \Omega_1}{N} \tag{4.7}$$

Before the development of the sinusoidal approximation for a random profile, an expression is defined regarding the PSD, in relation to a PSD at a reference wave number ($\Omega_0 = 1\,[rad/m]$), in Equation 4.8. It has been empirically verified that a waviness w=2 is an adequate parameter choice. The vertical profile at a point along the track is defined by a summation of a number $N \to \infty$ sine waves, and is evident in Equation 4.9. Moreover, the variance pertaining to a random profile generated by $N \to \infty$ sine waves is given by Equation 4.10, and when equated to Equation 4.6 for a true random profile, the expression for the amplitude of each component sine wave as a function of the PSD at each corresponding wave number is obtained in Equation 4.11.

$$\Phi(\Omega) = \Phi(\Omega_0)\left(\frac{\Omega}{\Omega_0}\right)^{-w} \tag{4.8}$$

$$z_R(x) = \sum_{i=1}^{N} A_i \sin(\Omega_i x - \Psi_i) \tag{4.9}$$

$$\sigma^2 = \frac{1}{2}\sum_{i=1}^{N} A_i^2 \tag{4.10}$$

$$A_i = \sqrt{2\Phi(\Omega_i)\Delta\Omega} \tag{4.11}$$

The discussion above provides the basis for modelling the irregularities of high speed maglev railway tracks [8]. Indeed it is possible to identify a power spectral density associated to this track type, as well as other types [9], present in Figure 4.1. Moreover, the generation of this profile type can be achieved with a direct implementation of the sinusoidal method, however another method to achieve a random input profile is through the well-documented ISO/TC 108/WG9 standard, where road roughness, power spectral density of the profile, and vehicle velocity primarily contribute to generating the irregularities. The use of this method is chosen for the numerical study of the system, given that the profile generated is similar to that obtainable from the sinusoidal approximation method, with a comparison evident in Figure 4.2. The PSD generated by means of the ISO method corresponds more closely to that of a welded railway track rather than to a super-speed guideway, however it is deemed appropriate in the context of the current study as the velocity imposed reflects conventional rail car speeds. The transfer function that can be identified beginning from the PSD in spatial domain defined in the standard is reported in Equation 4.12. Note that the term $s = i\omega$ in this context. The parameters used for the generation of the profiles are found in Table 4.1 with Table 4.1a indicating those necessary for the sinusoidal approximation method, and Table 4.1b outlining those generating the ISO profile. The value of G_r in particular corresponds with the roughness coefficient of the welded railway track, also coinciding with the value provided by the standard for a Grade A road. In addition, the frequency f_0 retains the purpose of shifting the pole of the transfer function such that higher frequency content is not included. The wavelength λ_f refers to the filter, and the longitudinal velocity v as well as the distance travelled are kept constant for the comparison. It must be noted that the value of the reference PSD Φ_0, coincides with that of a Grade A road [7], further confirming the adequacy of the comparison. The computational cost of the ISO profile's generation is also markedly lower.

$$TF(s) = \frac{2\pi\sqrt{G_r v}}{s + 2\pi f_0} \tag{4.12}$$

Having defined the irregularities of the track, a sinusoidal input profile (particularly that described by the HyperloopTT™ test track) coupled with random irregularities may be studied as a further attempt to gather an adequately realistic response of the system.

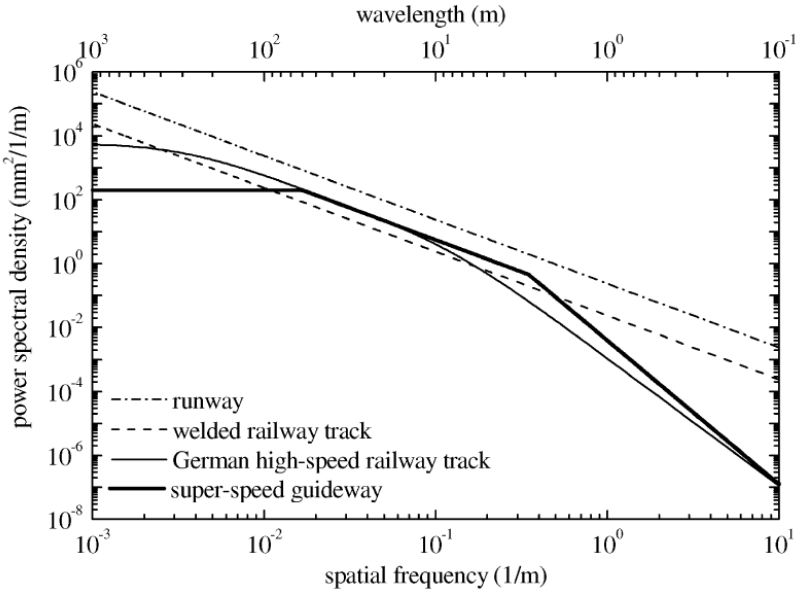

Figure 4.1: Power spectral densities of typical tracks, after Zhao and Zhai, 2002.

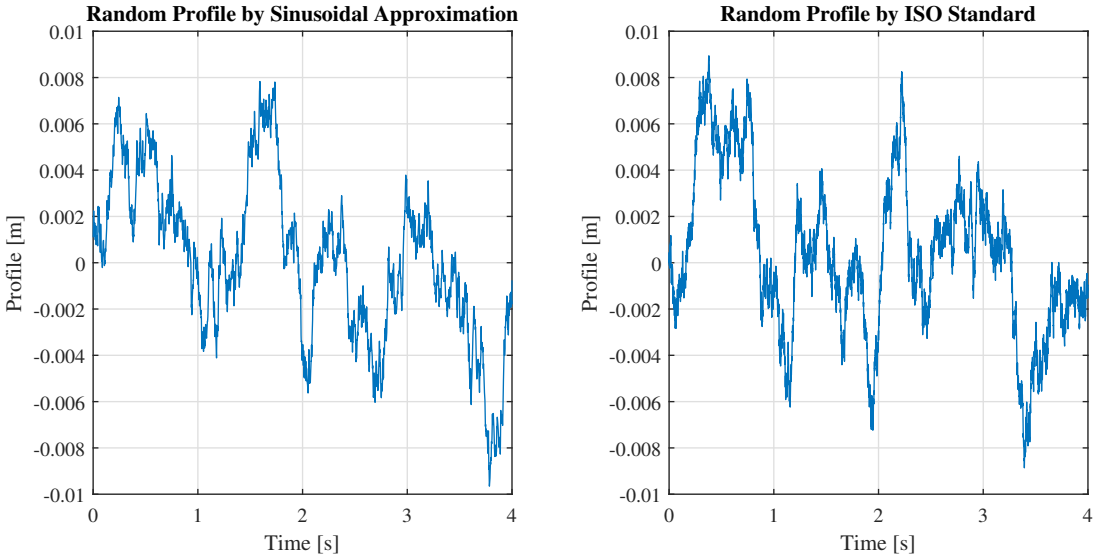

(a) Generation of random input profile by sinusoidal approximation

(b) Generation of random input profile by ISO standard

Figure 4.2: Comparison of different profiles generated by varying methods.

Parameter	Value	Units
Φ_0	10^{-6}	$\frac{\mathrm{m}^2}{\mathrm{rad/m}}$
Ω_{min}	0.0628	rad/m
Ω_{max}	62.83	rad/m
Ω_0	1	rad/m
N	2500	–

(a) Parameters used to obtain the random input profile in Figure 4.2a.

Parameter	Value	Units
G_r	1.5×10^{-6}	$\frac{\mathrm{m}^2}{\mathrm{rad/m}}$
v	25	m/s
f_0	0.25	Hz
λ_f	100	m
x_0	100	m

(b) Parameters used to obtain the random input profile in Figure 4.2b. Note that v and x_0 also pertain to the profile in Figure 4.2a.

Table 4.1: Parameters used for random profile generation.

4.2 Linear Quadratic Regulator

4.2.1 Overview and Implementation

A more general approach to the active control of the system under study is possible by means of the Linear Quadratic Regulator (LQR). The LQR is based on the minimisation of a cost function that considers appropriate target states coupled with weighting parameters. In particular, the cost function represents a quadratic performance index whose structure descends from the definition of the RMS value of the variables of interest [10][11]. With a larger weighting parameter, a lower magnitude of the coupled target state is achieved. The weighting parameters for the target states are contained in the diagonal and positive definite matrix **Q**. Similarly, the diagonal weighting matrix **R** acts on the control input, imposing an expensive or cheap control strategy. An expensive control strategy involves larger weighting on the control input, such that the action of the actuator is limited, reducing power consumption. Conversely, a cheap control strategy allows for the full exploitation of the actuator, such that the weighting parameters affecting the target states are more significant in comparison to those of the control input. The expression in Equation 4.13 outlines the structure of the cost function.

$$J = \int_0^\infty (\boldsymbol{x}^\top \boldsymbol{Q}\boldsymbol{x} + \boldsymbol{u}^\top \boldsymbol{R}\boldsymbol{u})dt \tag{4.13}$$

The output of the LQR optimisation consists of a state gain matrix **K** that is useful to compute the counteractive control forces **u**, for each linear actuator necessary to stabilise the system, summarised in Equation 4.14. Several studies have implemented the LQR to achieve optimal control using a linear actuator in the context of automotive applications [10][12], however its novel inclusion in the system representing the quarter-car model of the electrodynamic levitation vehicle is explored here.

$$\boldsymbol{u} = -\boldsymbol{K}\boldsymbol{x} \tag{4.14}$$

The practical implementation of the LQR in the form of a linear actuator requires an adequate observation of the target states. It can be noted that the lumped parameter model of the electrodynamically levitated system (including electrodynamic and mechanical behaviours) consists of states that cannot be observed with ease. Therefore, a model of reduced size is considered that accounts for more readily observable target states. The foundation of the aforementioned model lies in the introduction of an equivalent spring that approximates the behaviour of the levitation pad, coupling the track with the unsprung mass [1][13]. Thus all states concerning the eddy currents are ignored. Firstly, an expression for the stiffness is developed by using Equation 1.9 for the lift force in static conditions, followed by the substitution of Equation 1.10 for the nominal air gap. The resulting formulation evident in Equation 4.15 is a function of the total mass, the pole pitch ratio, and acceleration due to gravity. A notable feature of this approximation for the behaviour of the pad is that the system becomes marginally stable at worst.

$$k_p = \frac{2m_t g}{\gamma} \tag{4.15}$$

In all the systems under consideration, only one control input exists, consistent with the presence of one linear actuator, meaning the matrix $\mathbf{R}$ and vector $\mathbf{u}$ reduce to scalars. An optimisation of the LQR implementation is performed with a single weighting parameter r, varying from 0 to 1. The cost function representing this modification is expressed in Equation 4.16. With the reduced size model and the LQR approach defined, the target states of the optimisation are explicitly evidenced: the unsprung mass velocity and the sprung mass velocity. MATLAB® and Simulink® are used to attain time domain responses of the states. In particular, all states are extracted as outputs in a dynamic response of the system, and are operated on by the state gain matrix to provide a force that becomes an input to the system along with the external disturbances. For each value of the weighting parameter r, a set of RMS values pertaining to the outputs extracted represent performance indicators. It is evident that the weighting parameter r serves as an indicator for the priority assigned to each of the two states. With a unitary value, the cost function responds by minimising the sprung mass velocity the most, disregarding entirely the unsprung mass velocity. The opposite occurs with a null value. Note that the absence of the scalar R implies a null value, however in practice it is set to a comparatively smaller value with respect to the weighting parameter r (in the order of 10^{-5} to 10^{-12}). The studies presented herein impose the value of $R = 10^{-5}$ for an expensive control condition, and $R = 10^{-12}$ for a cheap control condition.

$$J = \int_0^\infty (r\dot{z}_s^2 + (1-r)\dot{z}_p^2)dt \tag{4.16}$$

The avenue taken in the evaluation of the LQR comprises the study of four models. Two of these models incorporate the LQR, with one being of reduced size while the other representing the system with the inherent instability, indicated in Figures 4.3 and 4.4 respectively. An analogous approach is present in the remaining two, with both utilising a passive damper, as seen in Figures 4.5 and 1.1. The intention of this comparison is two-fold. The lumped parameter model containing the instability is analysed against the reduced order model with the control mechanism constant in one comparison. A second comparison varies the control mechanism between an active and passive type. Of interest is the latter study, as the performance of the passive damper provides a benchmark for the LQR, with the LQR preferably demonstrating a superior behaviour. The cost function in Equation 4.16 is not written in a matrix and vector formulation, however the corresponding matrix **Q** can be identified for the optimisation, and is outlined in section A.10 of the Appendix. Note that section A.11 indicates the matrix **Q** necessary for the computation of the state gain matrix for the dynamic response analysis of the LQR controlled system containing the inherent instability. The main parameters useful for the models are presented in Table 4.2.

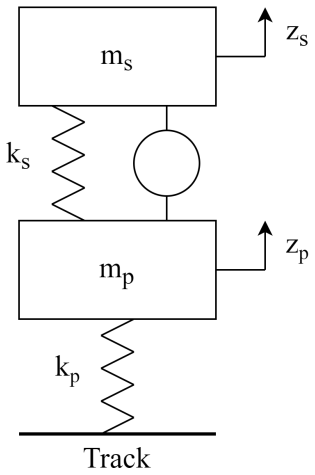

Figure 4.3: Quarter-car model of electrodynamically levitated pod with LQR control and equivalent pad stiffness.

Before proceeding to the analysis of the control strategies, an understanding of the adequacy of the proposed simplified model must be reached. For this purpose, the state space representations of both the reduced order model and the lumped

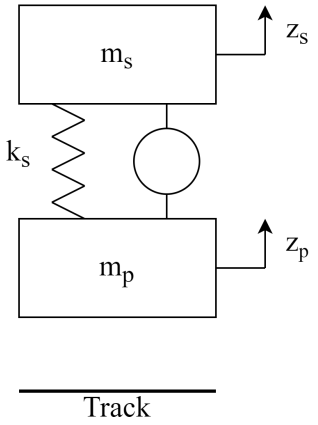

Figure 4.4: Quarter-car model of electrodynamically levitated pod with LQR control.

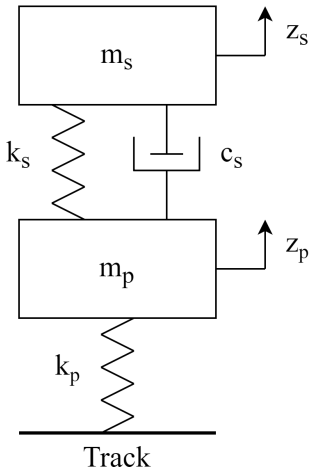

Figure 4.5: Quarter-car model of electrodynamically levitated pod with passive damper and equivalent pad stiffness.

parameter model (inherent instability included) are used to obtain their respective bode plots in MATLAB®. The state space representations of the four models useful for the current study are present in the Appendix, in sections A.5, A.6, A.8, and A.9. In particular, the receptance and inertance are observed to carry out the comparison, and it is noteworthy that the fit is appreciable, evident in Figures 4.6 and 4.7 respectively. For all analyses presented henceforth, the longitudinal velocity v is kept constant as in the study of the random profile generation, reported in Table 4.2. This pertains to the studies in frequency domain as well, due to the dependency of the dynamic matrix on the velocity for the lumped parameter model with inherent instability.

Parameter	Value	Units
v	25	$^{\mathrm{m}}/_{\mathrm{s}}$
x_0	100	m
m_s	20	kg
m_p	2	kg
m_t	22	kg
γ	0.0159	m
k_s	789.57	$\mathrm{N\,m^{-1}}$
k_p	27.1×10^3	$\mathrm{N\,m^{-1}}$
c_s	246.8	$\mathrm{N\,s\,m^{-1}}$
Λ_0	3.29×10^{-4}	Wb
L_1	7.72×10^{-10}	H
L_2	2.06×10^{-9}	H
L_3	4.12×10^{-9}	H
$\omega_{p,1}$	355.45	$\mathrm{rad\,s^{-1}}$
$\omega_{p,2}$	2.57×10^3	$\mathrm{rad\,s^{-1}}$
$\omega_{p,3}$	1.73×10^4	$\mathrm{rad\,s^{-1}}$

Table 4.2: Parameters used in the study of optimal control strategies.

The results indicate a further comparison regarding the type of LQR strategy employed, where Figures 4.6a and 4.7a exhibit the behaviour of the receptance and inertance respectively, for a choice of $R = 10^{-12}$. Conversely, Figures 4.6b and 4.7b concern the receptance and inertance for a selection of $R = 10^{-5}$. Although the fit is agreeable for this choice of R, a significant deviation between the two models can be observed for the inertance in particular. This may prove to be a source of inconsistencies in the dynamic responses to be studied. Note that in the figures, the weighting parameter notation r refers to the system described by the reduced order model, whereas the notation rf refers to the lumped parameter model containing the instability. Given that a more expensive control strategy limits the power consumption of the linear actuator, an expected decrease in performance is outlined in the behaviour of both the receptance and inertance. Indeed, at the frequencies where the sprung mass resonates, higher magnitude peaks are observed. An additional remark is an apparent shift of the poles when a cheaper control strategy is implemented; the weighting parameter r forces the poles towards lower frequencies.

Moreover, the general study of the reduced order model's response in the frequency domain is extended to a comparison between the control strategies introduced.

Figures 4.8 and 4.9 concern the receptance and inertance respectively, for two values of the weighting parameter r in a LQR controlled system, as well as for a system controlled by a passive damper. Figure 4.8a indicates a favourable performance for the unsprung mass displacement with a choice of the smallest value for r, when a cheap LQR control is used. Figure 4.8b also presents a superior performance for the smallest value of r, however a large peak is noted for the sprung mass. The performance at the largest value of r is comparable to that of the passively damped system. A similar analysis can be made for the inertance, where the magnitude of the sprung mass gain at the expected resonance frequency for the largest value of r is comparable to that of passive damper, in both the cheap and expensive control cases, indicated in Figures 4.9a and 4.9b.

The analysis moves to a study in the time domain, where RMS values for various quantities at different values for the weighting parameter r provide performance indications. The type of LQR strategy employed is also studied, varying from a cheap control strategy to an expensive control strategy. The responses for three input profiles are studied: a random profile generated by means of the ISO standard, a sinusoidal profile corresponding to the HyperloopTT™ track, and a profile combining the first two. In addition to the aforementioned longitudinal velocity, the distance travelled is maintained constant for all analyses, reported in Table 4.2.

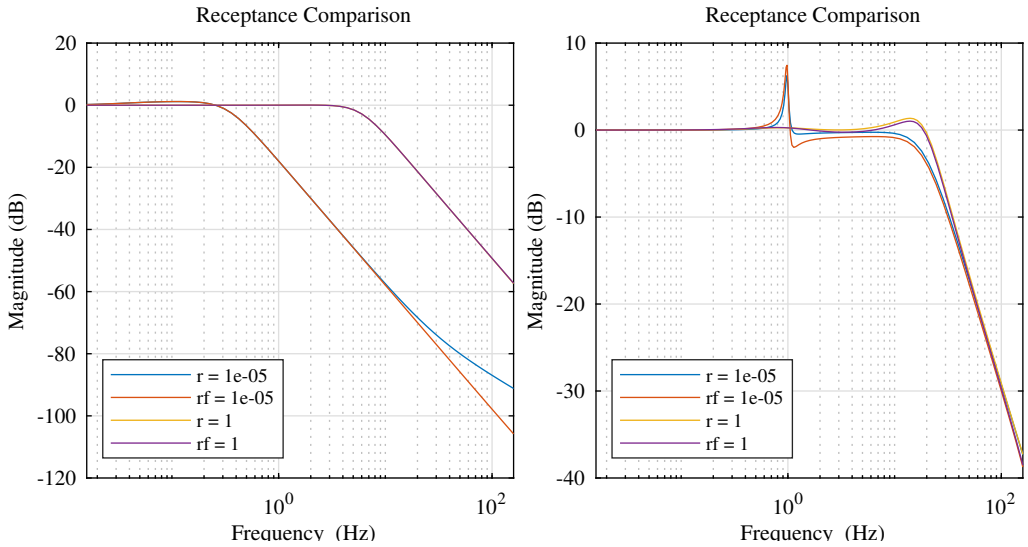

(a) Receptance comparison between reduced order model and lumped parameter model with inherent instability, concerning a cheap control strategy ($R = 10^{-12}$) and two weighting parameters r.

(b) Receptance comparison between reduced order model and lumped parameter model with inherent instability, concerning an expensive control strategy ($R = 10^{-5}$) and two weighting parameters r.

Figure 4.6: Receptance comparison for cheap and expensive control strategies, at varying weighting parameters r.

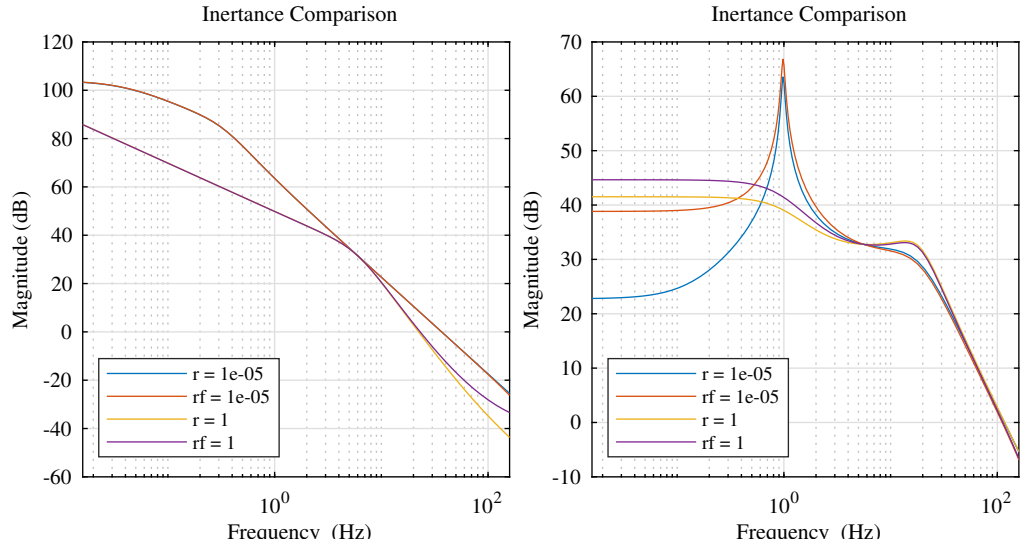

(a) Inertance comparison between reduced order model and lumped parameter model with inherent instability, concerning a cheap control strategy ($R = 10^{-12}$) and two weighting parameters r.

(b) Inertance comparison between reduced order model and lumped parameter model with inherent instability, concerning an expensive control strategy ($R = 10^{-5}$) and two weighting parameters r.

Figure 4.7: Inertance comparison for cheap and expensive control strategies, at varying weighting parameters r.

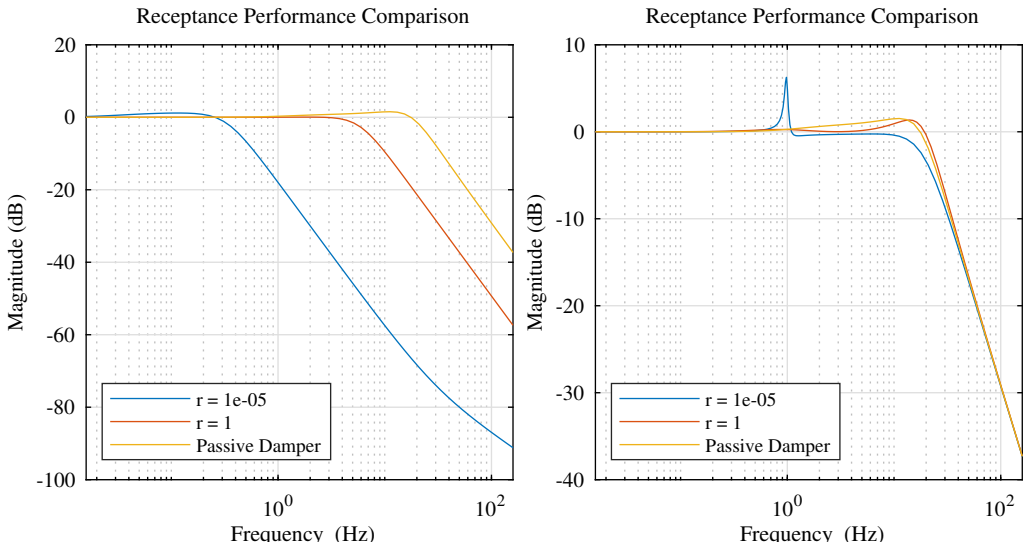

(a) Receptance performance comparison between reduced order model with a cheap LQR control strategy ($R = 10^{-12}$) and passive damping control.

(b) Receptance performance comparison between reduced order model with a cheap LQR control strategy ($R = 10^{-5}$) and passive damping control.

Figure 4.8: Receptance performance comparison for cheap and expensive control strategies.

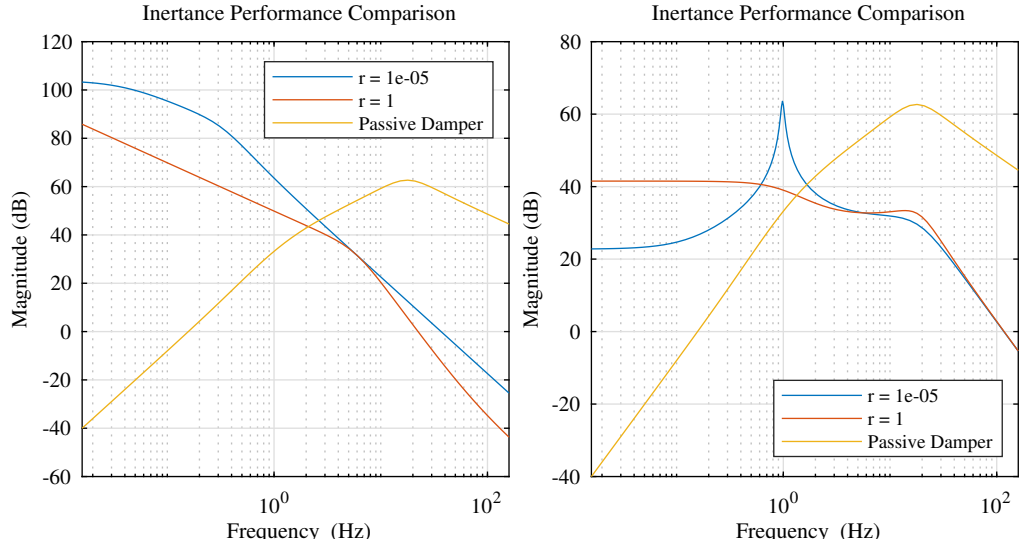

(a) Inertance performance comparison between reduced order model with a cheap LQR control strategy ($R = 10^{-12}$) and passive damping control.

(b) Inertance performance comparison between reduced order model with a cheap LQR control strategy ($R = 10^{-5}$) and passive damping control.

Figure 4.9: Inertance performance comparison for cheap and expensive control strategies.

4.2.2 Sinusoidal Profile Response

An initial analysis consists of studying effects of a sinusoidal track on the LQR controlled system. The parameters used for the generation of the HyperloopTT™ track profile are reported in Table 4.3, and a cheap LQR strategy is selected with $R = 10^{-12}$. The input profile in question imposes a certain dynamic response for different values of the weighting parameter r. The RMS of the sprung mass acceleration is presented varying with r, in Figure 4.10. Likewise, the unsprung mass displacement is reported in Figure 4.11. In particular, it must be outlined that the variables exhibit an expected behaviour regarding the range of r imposed. The sprung mass acceleration decreases with a value of r nearing 1, while the unsprung mass displacement increases. This reflects the design of the optimisation, evident in the matrices present in sections A.10 and A.11 of the Appendix. In all figures pertaining to the LQR analysis, Full Model refers to the model incorporating the instability, while Reduced Model refers to the system with the observable states. In all the plots, it is evident that the two models provide near indistinguishable behaviours with respect to r, further confirming that the reduced order model is adequate for its implementation in this context. In addition, the thresholds for performance discrimination are provided by the RMS values of the appropriate variables pertaining to the passively damped system.

Parameter	Value	Units
Z_D	2.5×10^{-3}	m
$Z_{\Delta T}$	2.5×10^{-3}	m
Z_S	10^{-3}	m
λ_L	40	m
λ_S	1	m

Table 4.3: Parameters used in the generation of the HyperloopTT™ track profile.

The control force and control power are observed to decrease with an increasing value of r, as seen in Figures 4.12 and 4.13 respectively. This may be viewed as advantageous due to the preference of the designer to choose a value of r that prioritises comfort. The control force required in an optimal comfort condition (with a unitary r) is verified to be approximately equal and opposite to the force exerted by the spring, meaning the sprung mass is stabilised. Both plots for the control force and the control power do not report maximum values, as their magnitudes exceed realistic bounds. These large power and force requirements occur for very small values of r introduced, where the system prioritises the minimisation of the unsprung mass velocity, and the actuator exerts a considerable force to stabilise it. Lower power consumption and force exertion are needed when the sprung mass is prioritised, because the actuator allows the unsprung mass to oscillate while

providing only the necessary force to stabilise the sprung mass.

The suspension stroke also reduces with a prioritisation on comfort, observed in Figure 4.14. The relative velocity is observed to generally decrease although it increases for values of r approaching 1, plotted in Figure 4.15. This reaffirms the movement of the unsprung mass with the stabilisation of the sprung mass. Once again the suspension stroke and relative velocity are exceedingly large for small values of r, hence the bounds for the axes are limited for clarity.

Moreover, given the behaviour of the weighting parameter r with respect to the RMS values of unsprung mass displacement and sprung mass acceleration, an optimal control condition can be identified with

$$0.991 < r < 1$$

where the upper bound represents the value of r guaranteeing a performance of the unsprung mass displacement that is superior to that of the passive damper. In this case, the value is unitary, due to the performance of the unsprung mass displacement being consistently more favourable than the passive damper for any value. Likewise, the lower bound represents the discriminant condition for the sprung mass acceleration. Note that this range is obtained by observing solely the curves related to the models of reduced order. With this condition, a state observer may be implemented to introduce active control using a linear actuator. The reduced order model may be configured with a desired value of r, and given the observability of the states, can be experimentally validated.

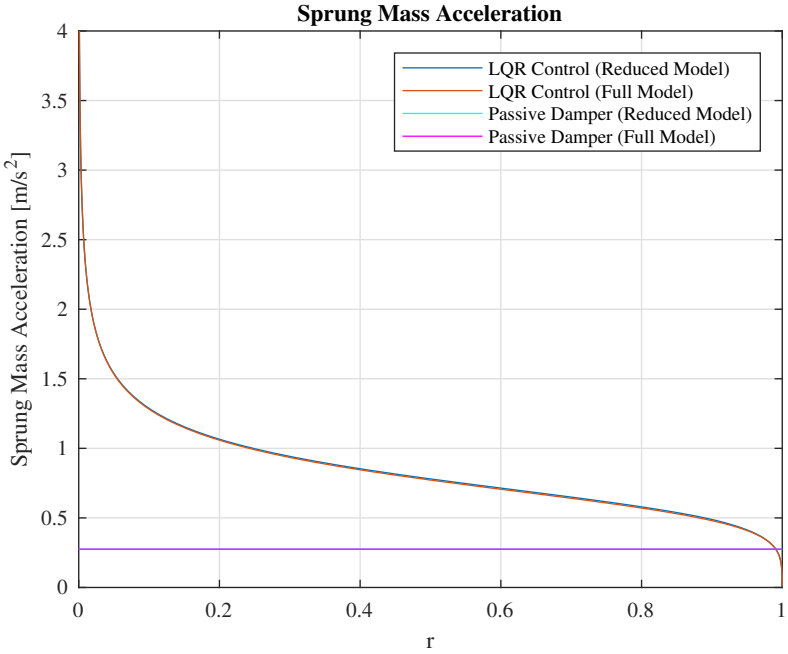

Figure 4.10: Sprung mass acceleration with $R = 10^{-12}$ and across varying weighting parameters r, for reduced order model and lumped parameter model with inherent instability. Sinusoidal input profile.

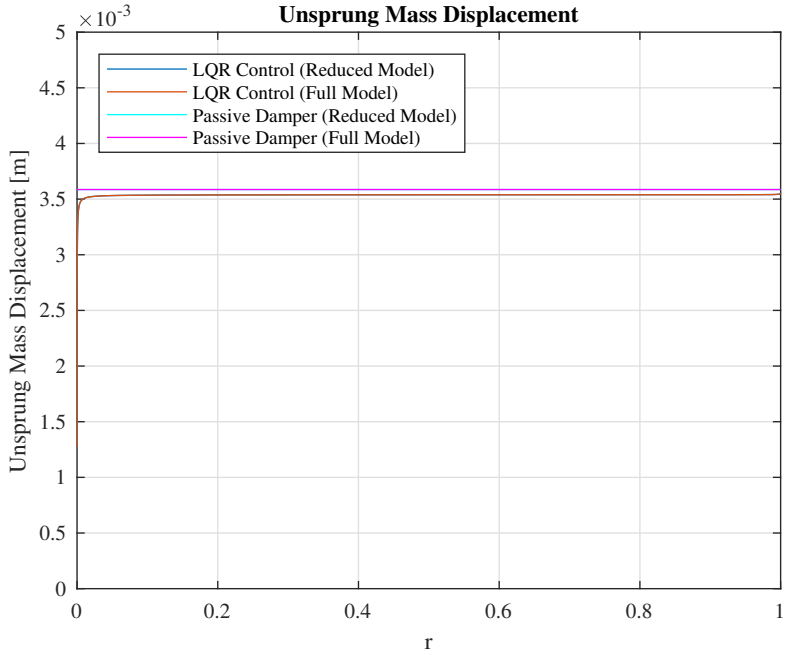

Figure 4.11: Unsprung mass displacement with $R = 10^{-12}$ and across varying weighting parameters r, for reduced order model and lumped parameter model with inherent instability. Sinusoidal input profile.

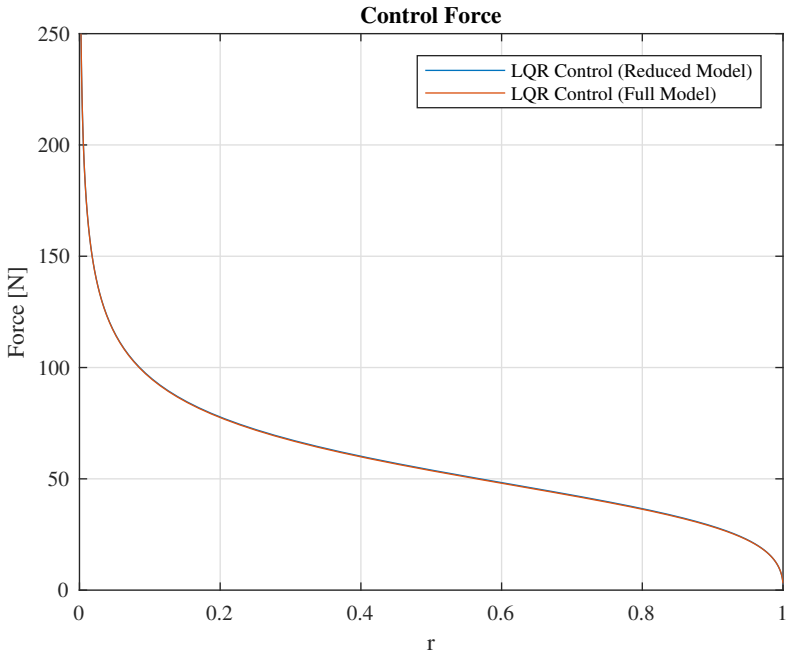

Figure 4.12: Control force for linear actuator with $R = 10^{-12}$ and across varying weighting parameters r, for reduced order model and lumped parameter model with inherent instability. Sinusoidal input profile.

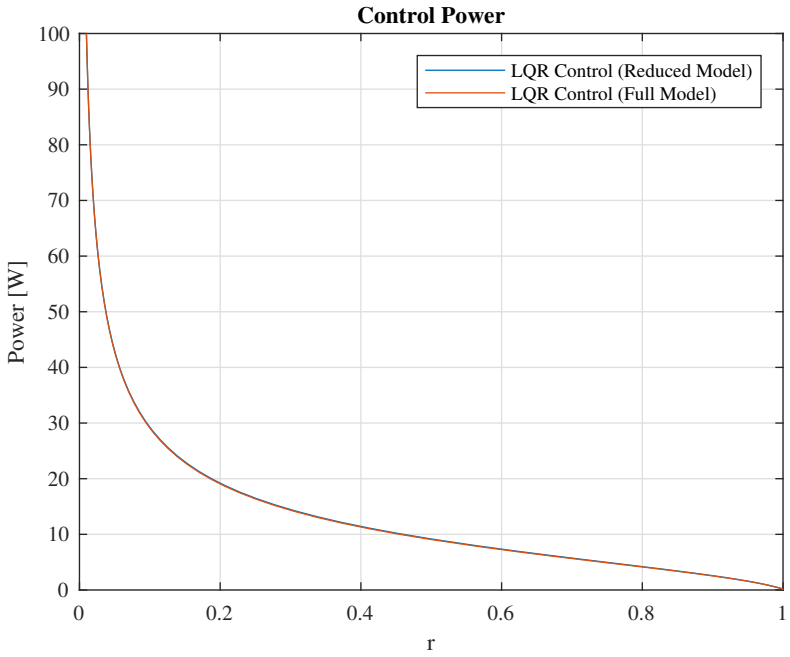

Figure 4.13: Control power for linear actuator with $R = 10^{-12}$ and across varying weighting parameters r, for reduced order model and lumped parameter model with inherent instability. Sinusoidal input profile.

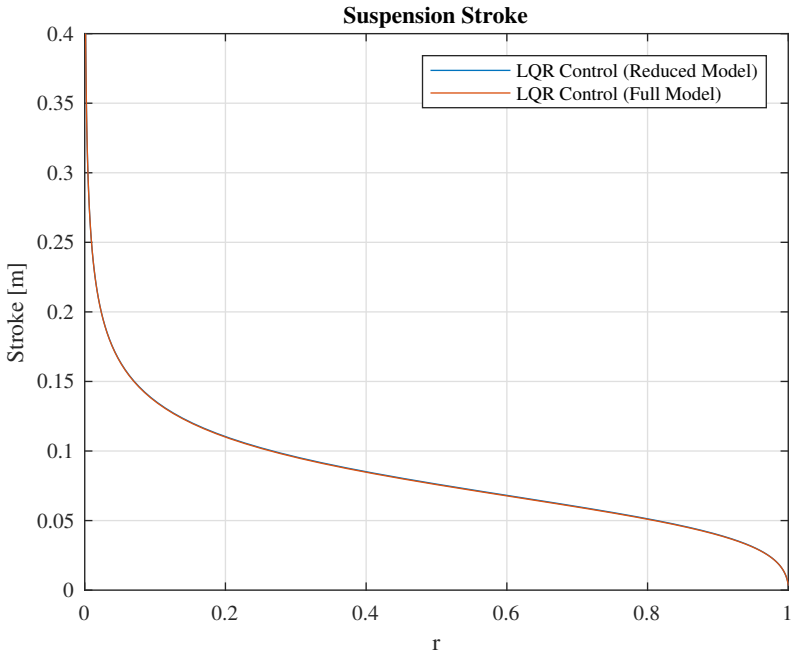

Figure 4.14: Suspension stroke for linear actuator with $R = 10^{-12}$ and across varying weighting parameters r, for reduced order model and lumped parameter model with inherent instability. Sinusoidal input profile.

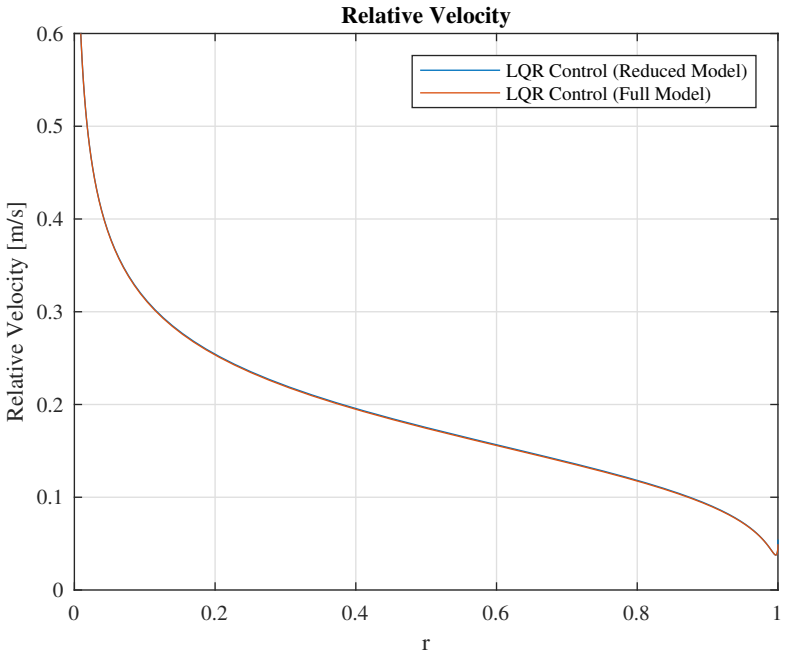

Figure 4.15: Relative velocity for linear actuator with $R = 10^{-12}$ and across varying weighting parameters r, for reduced order model and lumped parameter model with inherent instability. Sinusoidal input profile.

4.2.3 Random Profile Response

The behaviour of the LQR controlled system with respect to a random input profile across varying values of r is first indicated in Figure 4.16 with the sprung mass acceleration reported. Secondly, the unsprung mass displacement is presented in Figure 4.17. The two behaviours are once again consistent with those expected. The unsprung mass displacement is observed to increase significantly as r nears 1, while the sprung mass acceleration reflects increased comfort for the passengers. The LQR strategy imposed remains the same with $R = 10^{-12}$.

The control force and control power concerning the linear actuator reported in Figures 4.18 and 4.19 respectively again demonstrate similar characteristics as those for the sinusoidal input profile case. The power increases slightly with r approaching 1, due to the relative velocity exhibiting an expected increase, evident in Figure 4.21. The suspension stroke in Figure 4.20 notably behaves as expected with a minimised magnitude, for r in the neighbourhood of 1. It is observed that a track with random irregularities requests a higher control force for stabilisation compared to the previous case of the HyperloopTT™ track due to the unpredictable nature of the input.

As in the study regarding the sinusoidal input profile, discriminant values stemming from the results regarding the sprung and unsprung masses give rise to a condition

$$0.989 < r < 0.998$$

where the more stringent range must be respected for optimal performance. A value of r closer to the lower bound favours handling performance, however the constancy of the curve for unsprung mass displacement suggests that a similarly acceptable response is expected even if a selection of r improving comfort is made.

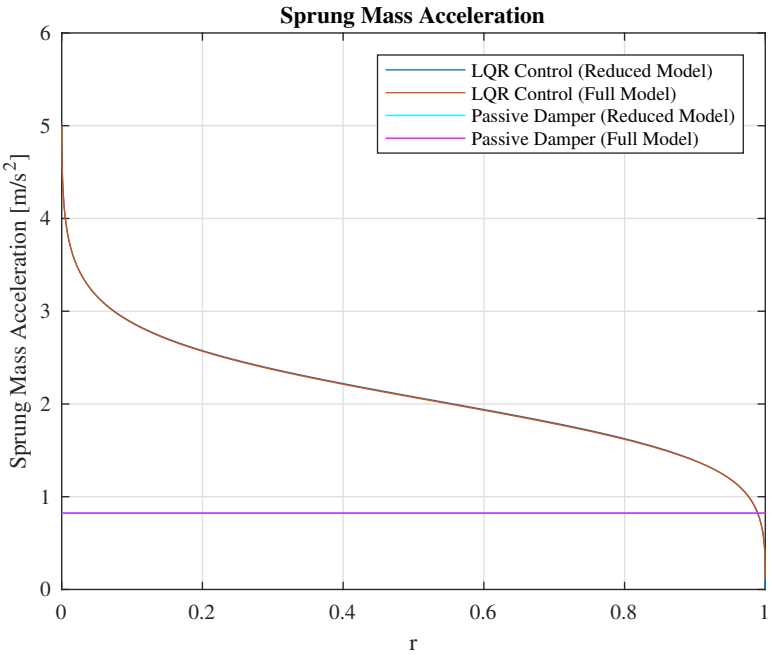

Figure 4.16: Sprung mass acceleration with $R = 10^{-12}$ and across varying weighting parameters r, for reduced order model and lumped parameter model with inherent instability. ISO standard input profile.

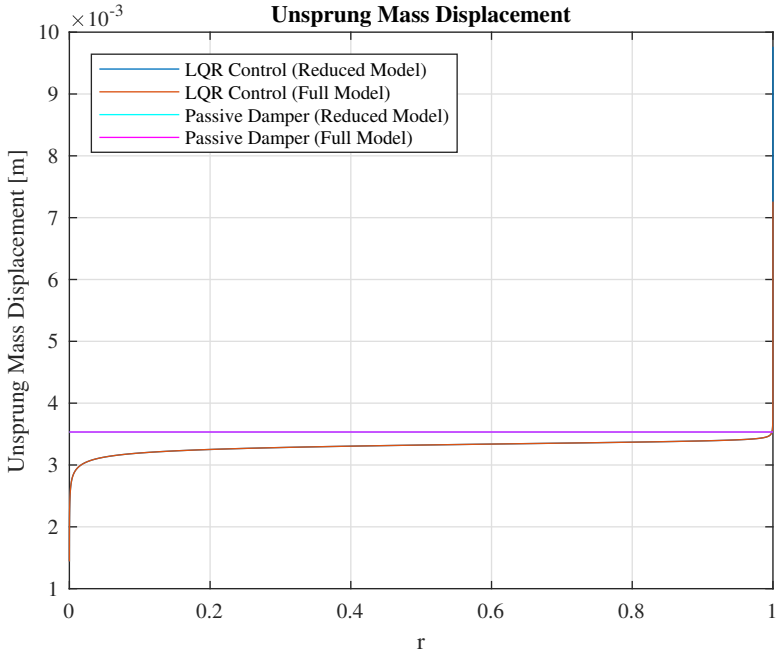

Figure 4.17: Unsprung mass displacement with $R = 10^{-12}$ and across varying weighting parameters r, for reduced order model and lumped parameter model with inherent instability. ISO standard input profile.

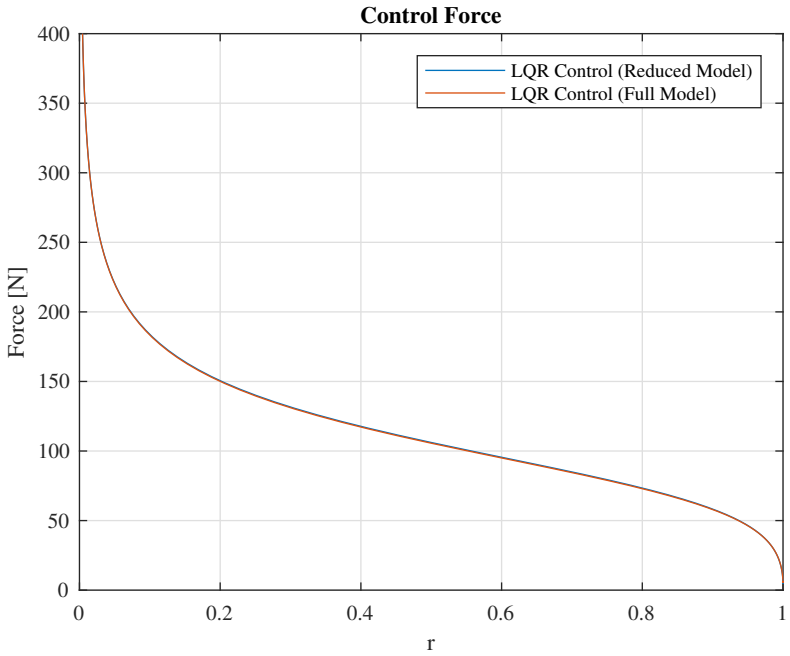

Figure 4.18: Control force for linear actuator with $R = 10^{-12}$ and across varying weighting parameters r, for reduced order model and lumped parameter model with inherent instability. ISO standard input profile.

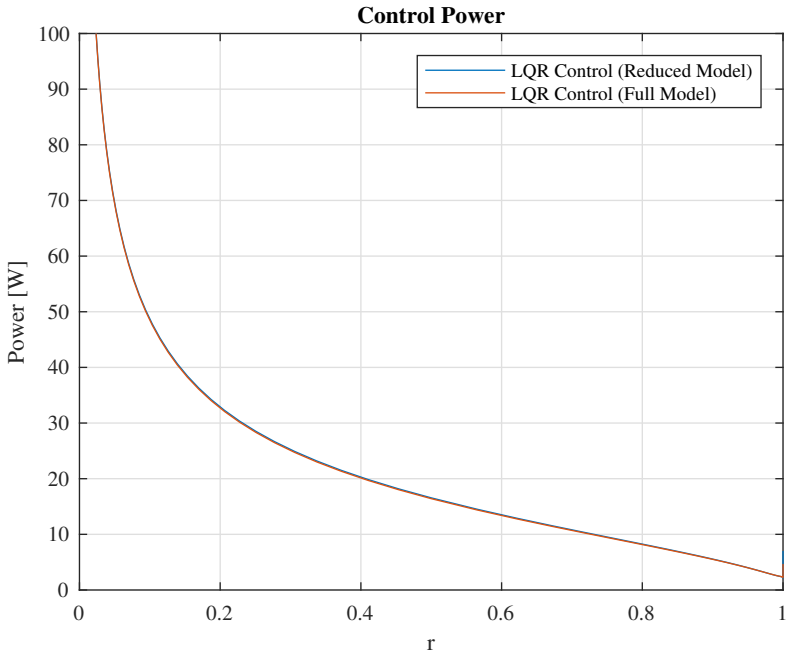

Figure 4.19: Control power for linear actuator with $R = 10^{-12}$ and across varying weighting parameters r, for reduced order model and lumped parameter model with inherent instability. ISO standard input profile.

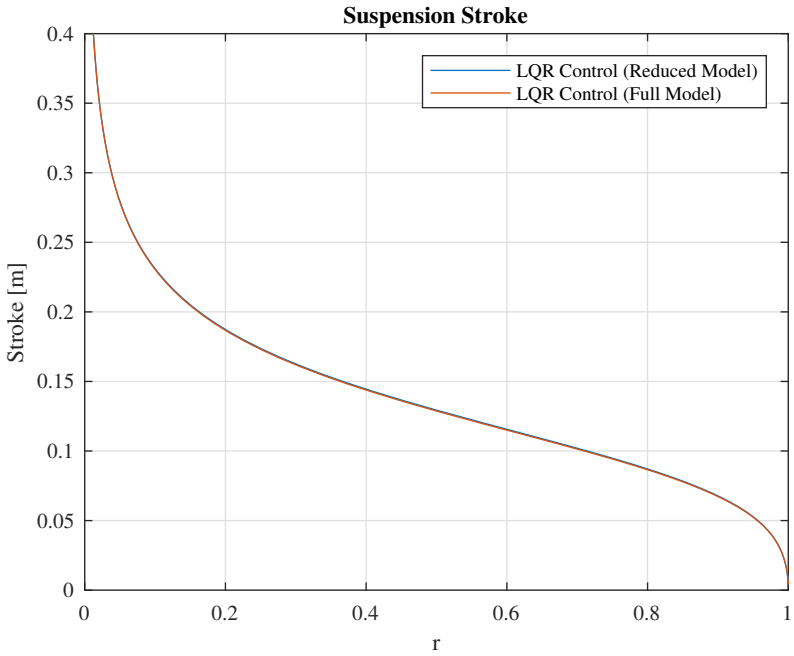

Figure 4.20: Suspension stroke for linear actuator with $R = 10^{-12}$ and across varying weighting parameters r, for reduced order model and lumped parameter model with inherent instability. ISO standard input profile.

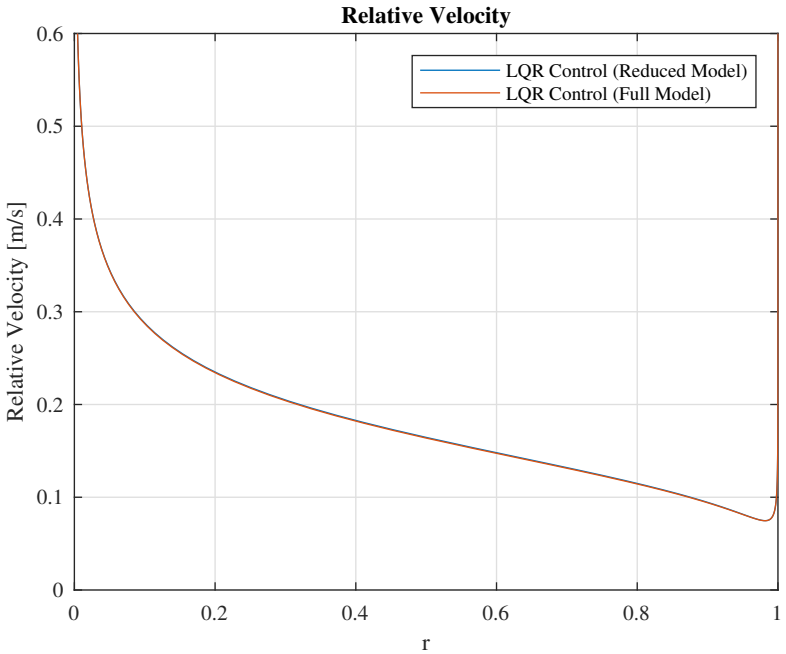

Figure 4.21: Relative velocity for linear actuator with $R = 10^{-12}$ and across varying weighting parameters r, for reduced order model and lumped parameter model with inherent instability. ISO standard input profile.

A more realistic profile may be conceived by combining the random profile generated by the ISO standard with the sinusoidal profile of the HyperloopTT™ track, although the LQR control strategy does not differ. The RMS values of sprung mass acceleration and unsprung mass displacement in this case are larger with respect to those in previous cases, however the pattern with respect to r remains the same. These behaviours are reported in Figure 4.22 for the sprung mass acceleration and Figure 4.23 for the unsprung mass displacement. The force and control power in Figures 4.24 and 4.25 respectively exhibit generally larger magnitudes as well, however of note is the plot for the relative velocity in Figure 4.27. The relative velocity for the largest values of r increases significantly, compared to other cases, however the power request is sufficiently limited due to the decreasing magnitude of the force.

The range of the parameter r necessary for optimal operation of the LQR controlled system

$$0.989 < r < 0.999$$

is similar to that pertaining to solely a random input profile. This suggests that a combination of the profiles yields a result that most closely relates to a purely random ground excitation of the system, meaning that the range obtained from the responses concerning an ISO standard input profile is sufficient for an implementation in a state observer active control.

A final study is conducted by exploring the differences stemming from an expensive control strategy (imposing $R = 10^{-5}$). Indeed, an immediate feature of note is the reduced conformity of the reduced model with the model incorporating the inherent instability. The sprung mass acceleration indicated in Figure 4.28 highlights a more conservative condition for the full model with the instability compared to the reduced order model. Regarding previous cases, one may observe that sprung mass acceleration is lower, however when plotted with the same scale, it is evident that increasing the control input penalisation reduces the sensitivity of r on the variables of interest. The unsprung mass displacement in Figure 4.29 indicates a comparable performance to that of the passive damper, although discriminant values for r can nonetheless be identified.

The control force and control power in Figures 4.30 and 4.31 respectively also highlight a more conservative behaviour for the full model. The control force is verified to not be equal and opposite to the force exerted by the spring, confirming that the actuator's capability is not fully exploited. A noteworthy result in this aspect of the study is the comparably lower power consumption, consistent with the penalisation of the control input characteristic of an expensive control strategy. The suspension stroke in Figure 4.32 is markedly lower in magnitude along the entire range of r compared to previous cases, consistent with a limitation of actuator

displacement. Likewise, the relative velocity in Figure 4.33 remains approximately constant for most of the range of r, while increasing for values nearing 1. This is again due to the stabilisation of the sprung mass.

An expensive control strategy may be implemented to reduce power consumption, although an adequate choice of the control input penalisation parameter R needs to be made. This is due to the divergence of the conformity for the two models, and if a reduced order model is to be successfully employed, their correspondence must be sufficiently close. Towards values of r closer to 1, the non-conformity is less prominent, allowing the reduced order model to be used for maximisation of passenger comfort. Moreover, the reduced sensitivity is exhibited by the range

$$0.518 < r < 0.948$$

where a wider set of values are suitable for optimal performance. This may be advantageous in tuning the system for a compromise in handling as well as passenger comfort. If only passenger comfort is desired, a cheaper control strategy with a stringent set for the weighting parameter r may be employed.

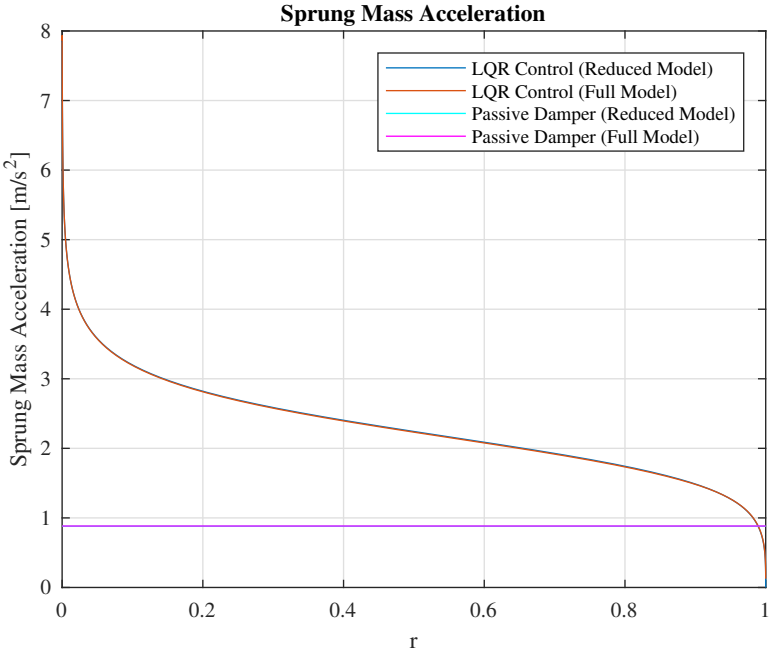

Figure 4.22: Sprung mass acceleration with $R = 10^{-12}$ and across varying weighting parameters r, for reduced order model and lumped parameter model with inherent instability. ISO standard and sinusoidal input profile combination.

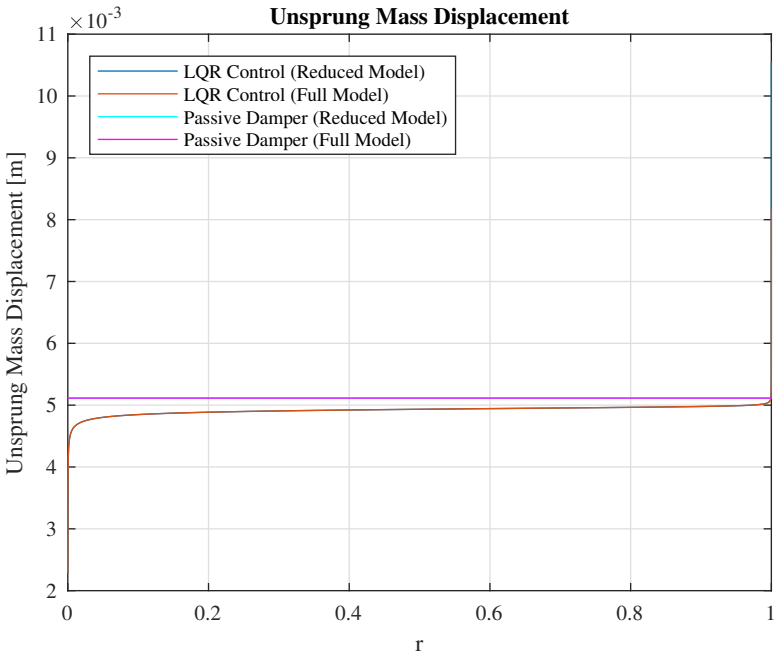

Figure 4.23: Unsprung mass displacement with $R = 10^{-12}$ and across varying weighting parameters r, for reduced order model and lumped parameter model with inherent instability. ISO standard and sinusoidal input profile combination.

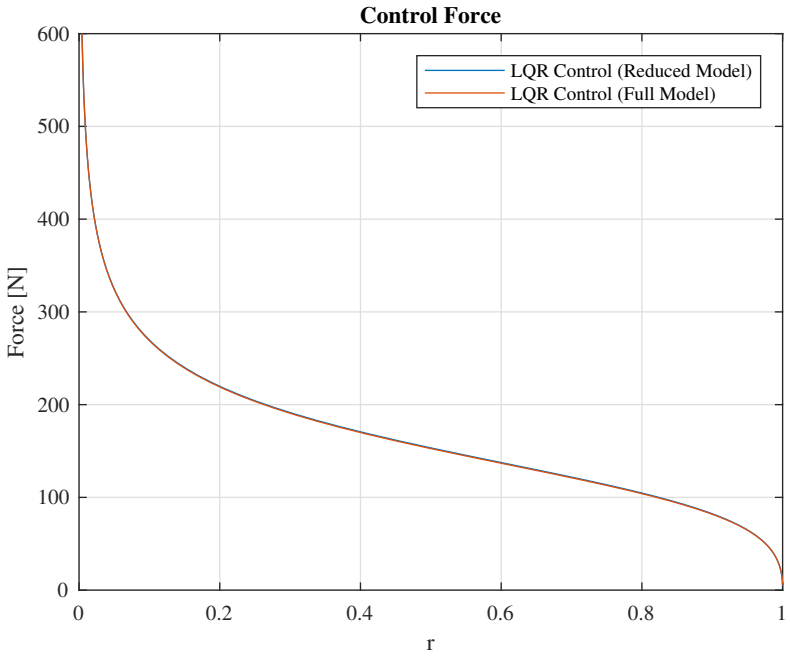

Figure 4.24: Control force for linear actuator with $R = 10^{-12}$ and across varying weighting parameters r, for reduced order model and lumped parameter model with inherent instability. ISO standard and sinusoidal input profile combination.

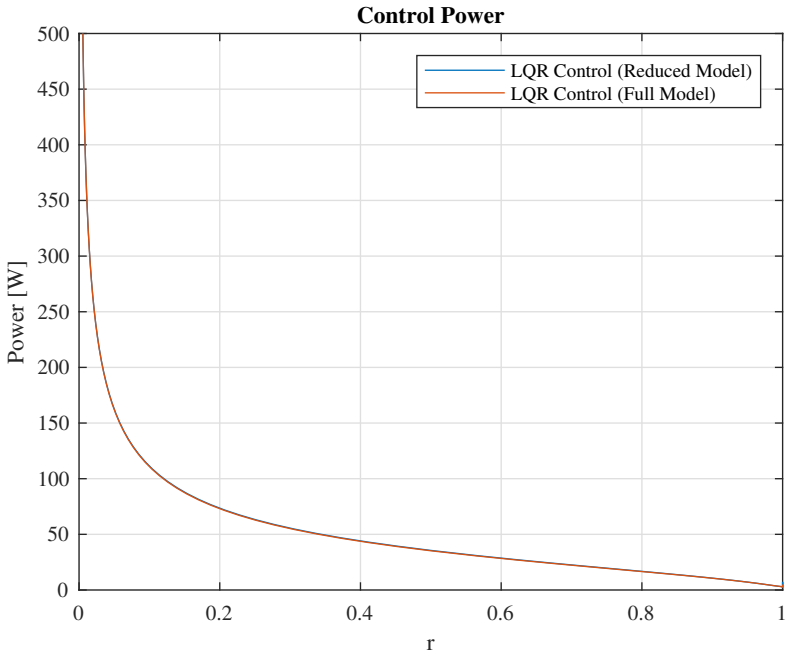

Figure 4.25: Control power for linear actuator with $R = 10^{-12}$ and across varying weighting parameters r, for reduced order model and lumped parameter model with inherent instability. ISO standard and sinusoidal input profile combination.

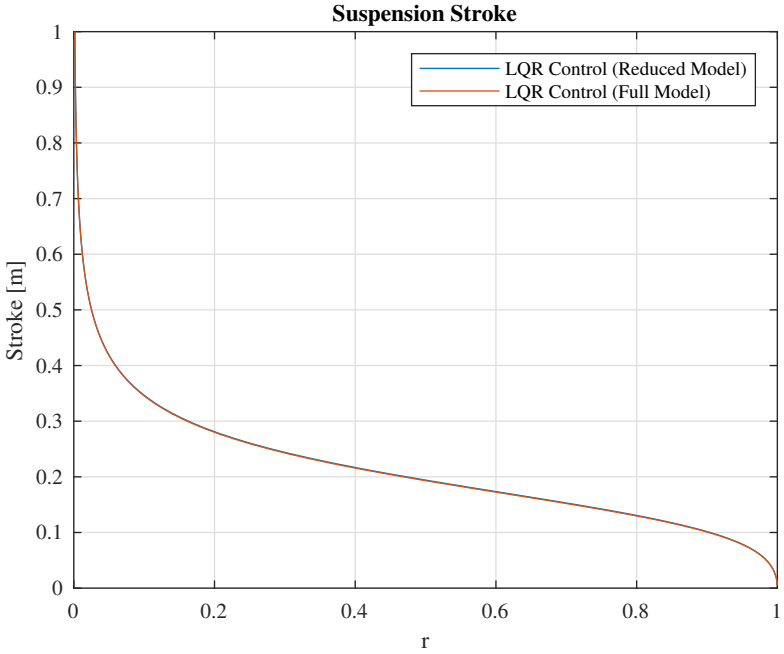

Figure 4.26: Suspension stroke for linear actuator with $R = 10^{-12}$ and across varying weighting parameters r, for reduced order model and lumped parameter model with inherent instability. ISO standard and sinusoidal input profile combination.

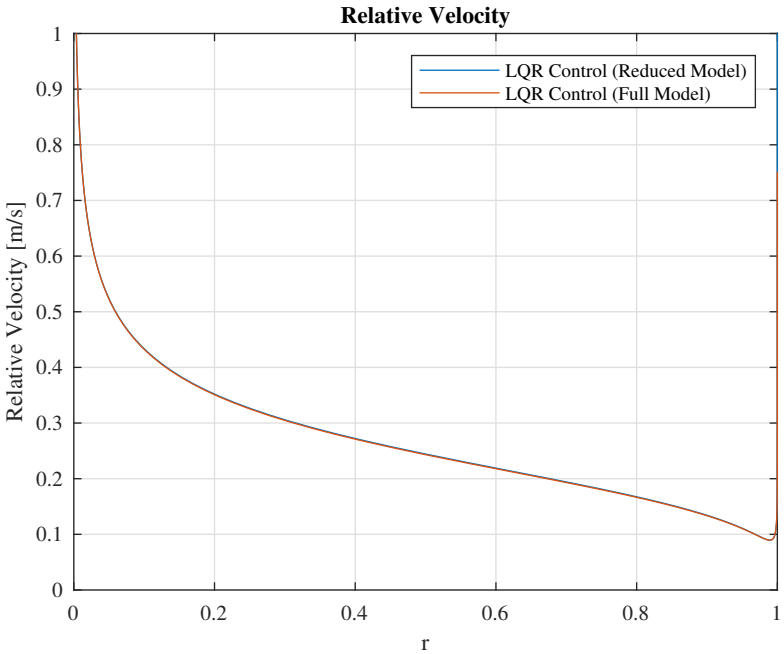

Figure 4.27: Relative velocity for linear actuator with $R = 10^{-12}$ and across varying weighting parameters r, for reduced order model and lumped parameter model with inherent instability. ISO standard and sinusoidal input profile combination.

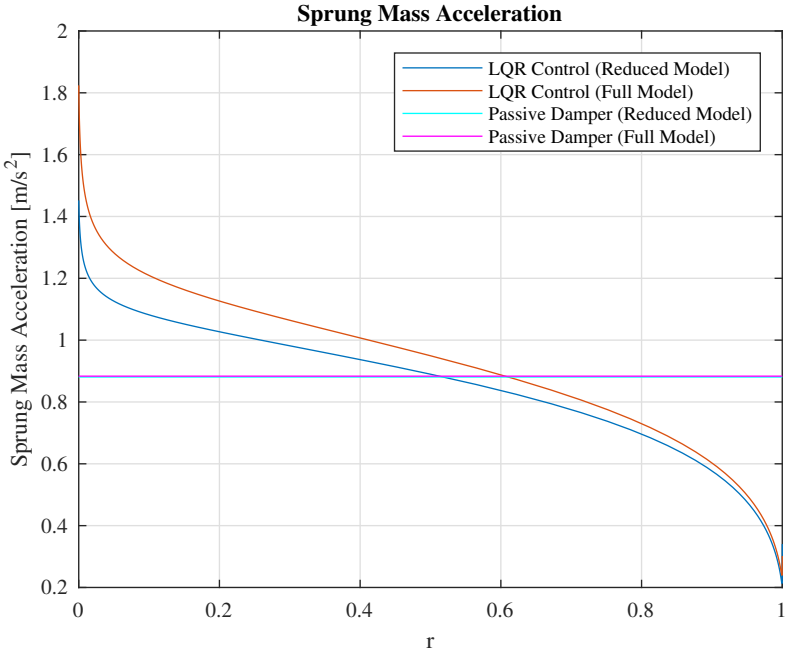

Figure 4.28: Sprung mass acceleration with $R = 10^{-5}$ and across varying weighting parameters r, for reduced order model and lumped parameter model with inherent instability. ISO standard and sinusoidal input profile combination.

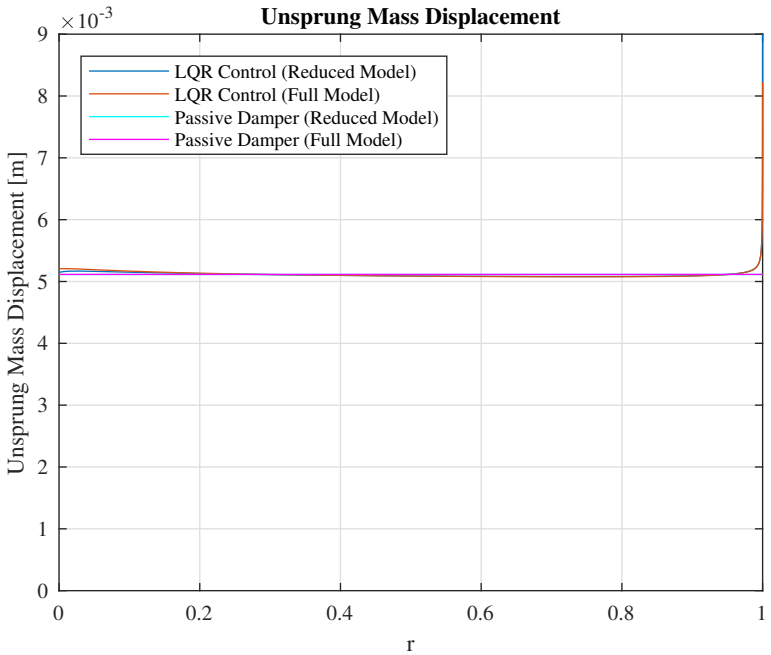

Figure 4.29: Unsprung mass displacement with $R = 10^{-5}$ and across varying weighting parameters r, for reduced order model and lumped parameter model with inherent instability. ISO standard and sinusoidal input profile combination.

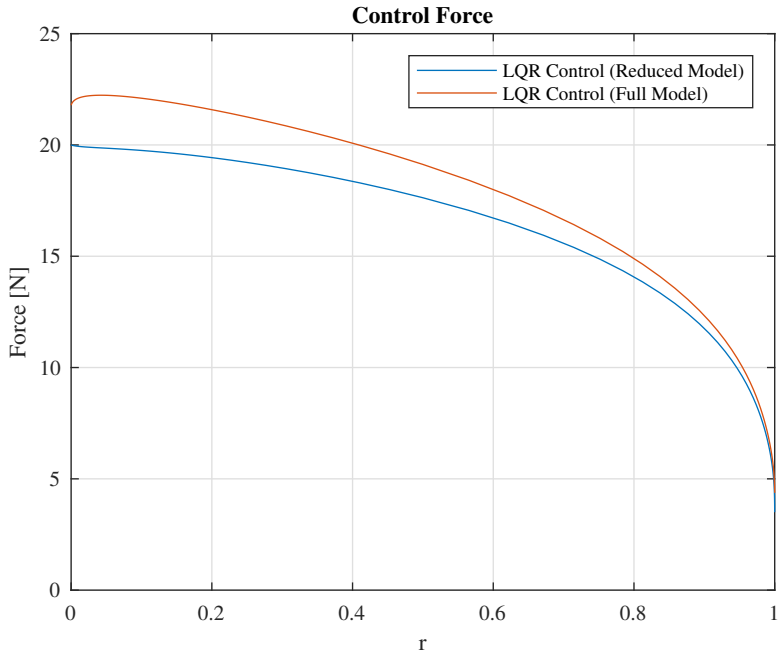

Figure 4.30: Control force for linear actuator with $R = 10^{-5}$ and across varying weighting parameters r, for reduced order model and lumped parameter model with inherent instability. ISO standard and sinusoidal input profile combination.

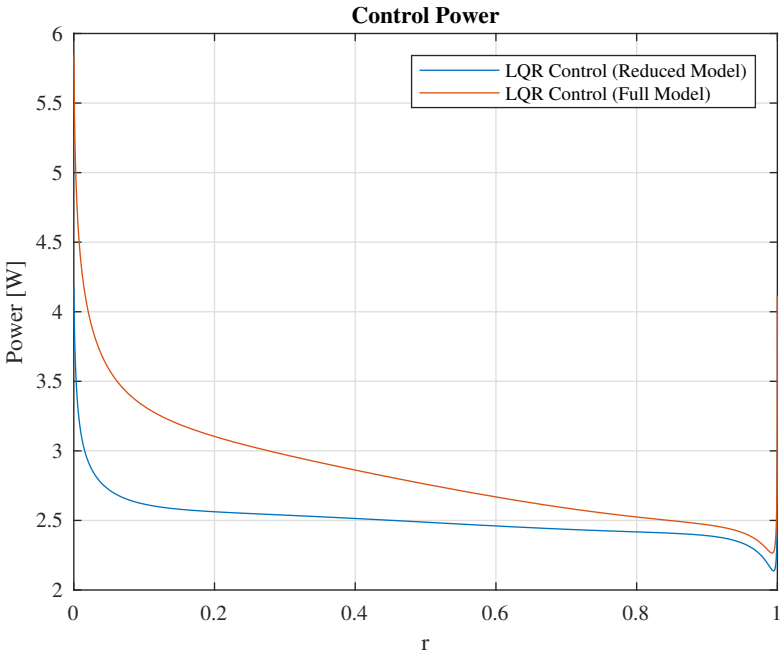

Figure 4.31: Control power for linear actuator with $R = 10^{-5}$ and across varying weighting parameters r, for reduced order model and lumped parameter model with inherent instability. ISO standard and sinusoidal input profile combination.

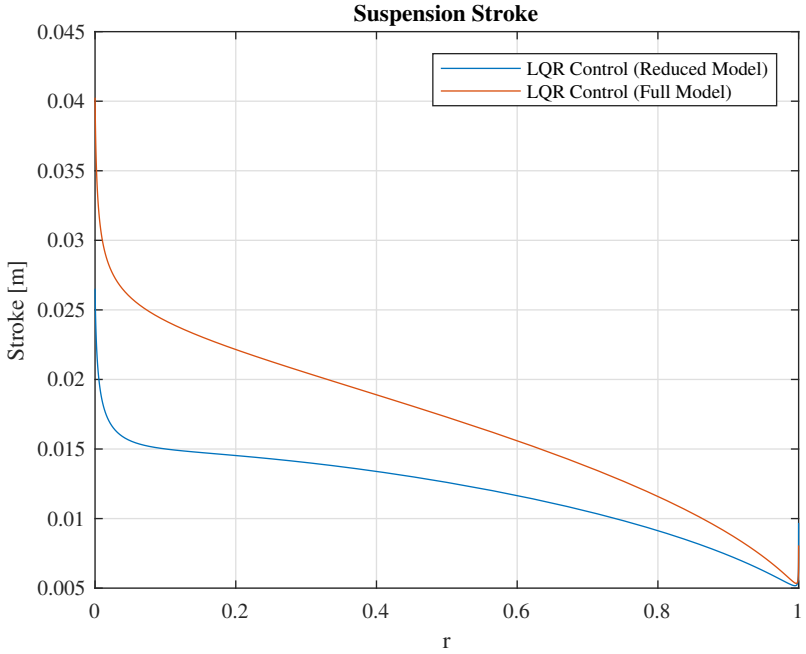

Figure 4.32: Suspension stroke for linear actuator with $R = 10^{-5}$ and across varying weighting parameters r, for reduced order model and lumped parameter model with inherent instability. ISO standard and sinusoidal input profile combination.

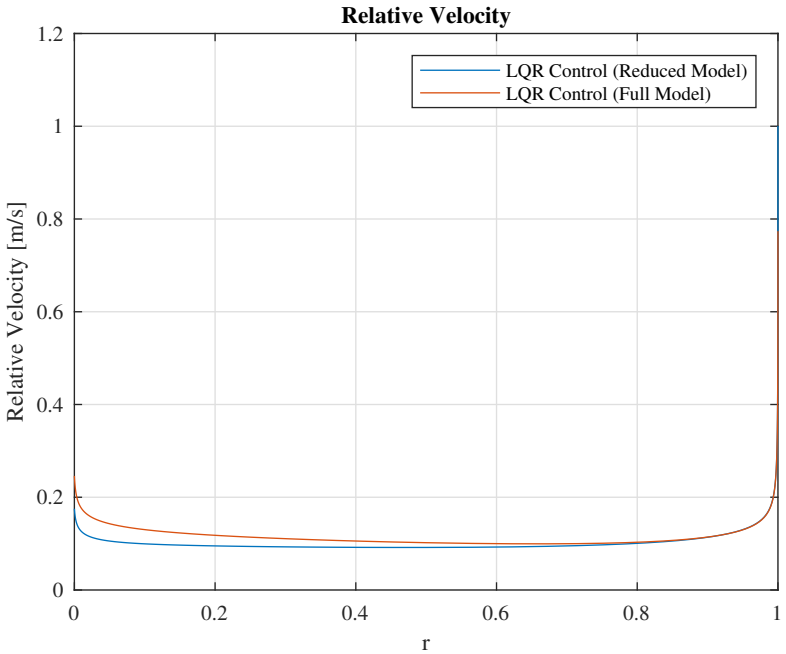

Figure 4.33: Relative velocity for linear actuator with $R = 10^{-5}$ and across varying weighting parameters r, for reduced order model and lumped parameter model with inherent instability. ISO standard and sinusoidal input profile combination.

Chapter 5

Final Remarks

5.1 Conclusions

The present study encompasses a characterisation of the effects of irregularities on the static lift and drag forces, through an optimisation that yields an air gap offset, allowing for a COMSOL model to replicate experimental behaviour. Unique air gap offsets for each nominal air gap are attainable. In addition, one air gap offset applicable to all nominal air gaps is found. The analysis concerns both configurations of the Halbach array, and as a result, the test bench is better understood, and a more accurate FEM model is available.

With regards to dynamic phenomena, skyhook and groundhook damping are implemented and studied individually within the system. Stability wells are identified, and time domain responses are obtained to validate the feasibility of such control strategies. The most optimal configuration is found to be a combination of both imaginary damping contributions, with $c_{sky} = 220$ N s m^{-1}, $c_{gr} = 2020.2$ N s m^{-1}, and $c_s = 25.25$ N s m^{-1}. The value of c_{sky} corresponds to a condition of optimal comfort found in the analysis of solely a skyhook implementation, with the suspension damping chosen to conserve stability as per the map generated. Similarly, the analysis of including only groundhook damping yields the value cited above. This strategy may be further implemented into a semi-active control system to achieve desired passenger comfort. Concerning further analysis of electrodynamic levitation dynamics, input profiles are studied in anticipation of the LQR approach for active control. The ISO standard is adopted for random track irregularities, and the HyperloopTT™ track profile is adopted for a study of a sinusoidal input. A reduced order model is implemented to ensure a potential use in state-observer active control, and its adequacy is confirmed for a cheap control condition, with an expensive control condition presenting deviations, in the frequency domain. Time

domain responses are generated for each value of r, ranging from 0 to 1. RMS values of extracted states become performance indicators, and are compared against those of the passively damped model, particularly for the sprung mass acceleration and unsprung mass displacement. For each input case, a range of r values is identified, such that the LQR controlled system's performance is superior to that of the passively damped system. The range $0.989 < r < 0.998$ for r stemming from the ISO standard profile input, although strict, is deemed sufficient for a prioritisation of passenger comfort for a cheap control strategy. A lower sensitivity of r is noted for an expensive control strategy, as well as a less satisfactory match for time domain plots. An expensive control strategy is advised only for values of r in the neighbourhood of 1, even though the identifiable range of superior performance is considerably wider than that of a cheap control strategy.

5.2 Further work

Further work in this field consists of introducing active control, facilitated by a state observer, on the voice coil of the test bench. The LQR control strategy may be imposed, and an experimental campaign may be initiated to validate numerical findings herein presented. The numerical work requires a modification to suit the characteristics of the voice coil system, however the foundation for attaining optimal weighting parameters r has been laid. For a given range of r and a suitable value of control input penalisation R, experimental results may inform the most optimal selection of final weighting parameters that significantly improve passenger comfort. Moreover, the numerical work regarding skyhook and groundhook damping may be practically exploited in a similar manner, integrating the control in an experimental context. A comparison between the strategy employing skyhook and groundhook damping, and the LQR must be carried out as well.

To consolidate this work, a study on ride comfort may provide more refined control strategies, where not only performance is considered, but also passenger well-being. The Mean Comfort Method and Sperling's Method may be used [14], where the RMS of the vertical acceleration is used to generate an index that corresponds with a certain level of perturbation sensation. The index in the Mean Comfort Method undergoes a weighted filtering, accounting for high human sensitivity to vertical vibrations. Conversely, Sperling's Method may be computed either over a range of frequencies [14], or at a specific frequency [15] regarding external excitations, however in both scenarios a frequency weight factor must be considered. These ride comfort characterisation methods may prove to generate a more complete control strategy that reliably prioritises passenger comfort.

Appendix A

Matrices

A.1 State Space for Skyhook Damping Implementation

$$\mathbf{z} = \begin{bmatrix} i_{d,1} & i_{q,1} & i_{d,2} & i_{q,2} & i_{d,3} & i_{q,3} & \dot{z}_p & z_p & \dot{z}_s & z_s & z_{in} \end{bmatrix}^\top$$

$$\mathbf{y} = \begin{bmatrix} z_p & \dot{z}_s & \ddot{z}_s \end{bmatrix}^\top$$

$$p_f = -\frac{2\Lambda_0}{\gamma m_p} \mathrm{e}^{-z_{p,0}/\gamma}$$

$$p_d = \frac{\Lambda_0}{\gamma} \mathrm{e}^{-z_{p,0}/\gamma}$$

$$p_q = \frac{\omega\Lambda_0}{\gamma} \mathrm{e}^{-z_{p,0}/\gamma}$$

$$\boldsymbol{A_{sky}} = \begin{bmatrix} \text{-}\omega_{p,1} & \omega & 0 & 0 & 0 & 0 & \frac{p_d}{L_1} & 0 & 0 & 0 & 0 \\ \text{-}\omega & \text{-}\omega_{p,1} & 0 & 0 & 0 & 0 & 0 & \frac{p_q}{L_1} & 0 & 0 & \frac{-p_q}{L_1} \\ 0 & 0 & \text{-}\omega_{p,2} & \omega & 0 & 0 & \frac{p_d}{L_2} & 0 & 0 & 0 & 0 \\ 0 & 0 & \text{-}\omega & \text{-}\omega_{p,2} & 0 & 0 & 0 & \frac{p_q}{L_2} & 0 & 0 & \frac{-p_q}{L_2} \\ 0 & 0 & 0 & 0 & \text{-}\omega_{p,3} & \omega & \frac{p_d}{L_3} & 0 & 0 & 0 & 0 \\ 0 & 0 & 0 & 0 & \text{-}\omega & \text{-}\omega_{p,3} & 0 & \frac{p_q}{L_3} & 0 & 0 & \frac{-p_q}{L_3} \\ p_f & 0 & p_f & 0 & p_f & 0 & \frac{-c_s}{m_p} & \frac{-k_s}{m_p} & \frac{c_s}{m_p} & \frac{k_s}{m_p} & 0 \\ 0 & 0 & 0 & 0 & 0 & 0 & 1 & 0 & 0 & 0 & 0 \\ 0 & 0 & 0 & 0 & 0 & 0 & \frac{c_s}{m_s} & \frac{k_s}{m_s} & \frac{-c_s-c_{sky}}{m_s} & \frac{-k_s}{m_s} & 0 \\ 0 & 0 & 0 & 0 & 0 & 0 & 0 & 0 & 1 & 0 & 0 \\ 0 & 0 & 0 & 0 & 0 & 0 & 0 & 0 & 0 & 0 & 0 \end{bmatrix}$$

$$\boldsymbol{B_{sky}} = \begin{bmatrix} -\frac{p_d}{L_1} & 0 & -\frac{p_d}{L_2} & 0 & -\frac{p_d}{L_3} & 0 & 0 & 0 & 0 & 0 & 1 \end{bmatrix}^\top$$

$$\boldsymbol{C_{sky}} = \begin{bmatrix} 0 & 0 & 0 & 0 & 0 & 0 & 0 & 1 & 0 & 0 & 0 \\ 0 & 0 & 0 & 0 & 0 & 0 & 0 & 0 & 1 & 0 & 0 \\ 0 & 0 & 0 & 0 & 0 & 0 & \frac{c_s}{m_s} & \frac{k_s}{m_s} & \frac{-(c_s+c_{sky})}{m_s} & \frac{-k_s}{m_s} & 0 \end{bmatrix}$$

$$\boldsymbol{D_{sky}} = \begin{bmatrix} 0 & 0 & 0 \end{bmatrix}^\top$$

A.2 State Space for Groundhook Damping Implementation

$$\mathbf{z} = \begin{bmatrix} i_{d,1} & i_{q,1} & i_{d,2} & i_{q,2} & i_{d,3} & i_{q,3} & \dot{z}_p & z_p & \dot{z}_s & z_s & z_{in} \end{bmatrix}^\top$$

$$\mathbf{y} = \begin{bmatrix} z_p & \dot{z}_s & \ddot{z}_s \end{bmatrix}^\top$$

$$p_f = -\frac{2\Lambda_0}{\gamma m_p} \mathrm{e}^{-z_{p,0}/\gamma}$$

$$p_d = \frac{\Lambda_0}{\gamma} \mathrm{e}^{-z_{p,0}/\gamma}$$

$$p_q = \frac{\omega\Lambda_0}{\gamma} \mathrm{e}^{-z_{p,0}/\gamma}$$

$$\boldsymbol{A_{gr}} = \begin{bmatrix} \text{-}\omega_{p,1} & \omega & 0 & 0 & 0 & 0 & \frac{p_d}{L_1} & 0 & 0 & 0 & 0 \\ \text{-}\omega & \text{-}\omega_{p,1} & 0 & 0 & 0 & 0 & 0 & \frac{p_q}{L_1} & 0 & 0 & \frac{-p_q}{L_1} \\ 0 & 0 & \text{-}\omega_{p,2} & \omega & 0 & 0 & \frac{p_d}{L_2} & 0 & 0 & 0 & 0 \\ 0 & 0 & \text{-}\omega & \text{-}\omega_{p,2} & 0 & 0 & 0 & \frac{p_q}{L_2} & 0 & 0 & \frac{-p_q}{L_2} \\ 0 & 0 & 0 & 0 & \text{-}\omega_{p,3} & \omega & \frac{p_d}{L_3} & 0 & 0 & 0 & 0 \\ 0 & 0 & 0 & 0 & \text{-}\omega & \text{-}\omega_{p,3} & 0 & \frac{p_q}{L_3} & 0 & 0 & \frac{-p_q}{L_3} \\ p_f & 0 & p_f & 0 & p_f & 0 & \frac{-c_s-c_{gr}}{m_p} & \frac{-k_s}{m_p} & \frac{c_s}{m_p} & \frac{k_s}{m_p} & 0 \\ 0 & 0 & 0 & 0 & 0 & 0 & 1 & 0 & 0 & 0 & 0 \\ 0 & 0 & 0 & 0 & 0 & 0 & \frac{c_s}{m_s} & \frac{k_s}{m_s} & \frac{-c_s}{m_s} & \frac{-k_s}{m_s} & 0 \\ 0 & 0 & 0 & 0 & 0 & 0 & 0 & 0 & 1 & 0 & 0 \\ 0 & 0 & 0 & 0 & 0 & 0 & 0 & 0 & 0 & 0 & 0 \end{bmatrix}$$

$$\boldsymbol{B_{gr}} = \begin{bmatrix} -\frac{p_d}{L_1} & 0 & -\frac{p_d}{L_2} & 0 & -\frac{p_d}{L_3} & 0 & 0 & 0 & 0 & 0 & 1 \end{bmatrix}^\top$$

$$\boldsymbol{C_{gr}} = \begin{bmatrix} 0 & 0 & 0 & 0 & 0 & 0 & 0 & 1 & 0 & 0 & 0 \\ 0 & 0 & 0 & 0 & 0 & 0 & 0 & 0 & 1 & 0 & 0 \\ 0 & 0 & 0 & 0 & 0 & 0 & \frac{c_s}{m_s} & \frac{k_s}{m_s} & \frac{-c_s}{m_s} & \frac{-k_s}{m_s} & 0 \end{bmatrix}$$

$$\boldsymbol{D_{gr}} = \begin{bmatrix} 0 & 0 & 0 \end{bmatrix}^\top$$

A.3 State Space for Skyhook and Groundhook Damping Implementation

$$\mathbf{z} = \begin{bmatrix} i_{d,1} & i_{q,1} & i_{d,2} & i_{q,2} & i_{d,3} & i_{q,3} & \dot{z}_p & z_p & \dot{z}_s & z_s & z_{in} \end{bmatrix}^\top$$

$$\mathbf{y} = \begin{bmatrix} z_p & \dot{z}_s & \ddot{z}_s \end{bmatrix}^\top$$

$$p_f = -\frac{2\Lambda_0}{\gamma m_p} \mathrm{e}^{-z_{p,0}/\gamma}$$

$$p_d = \frac{\Lambda_0}{\gamma} \mathrm{e}^{-z_{p,0}/\gamma}$$

$$p_q = \frac{\omega\Lambda_0}{\gamma} \mathrm{e}^{-z_{p,0}/\gamma}$$

$$\boldsymbol{A_h} = \begin{bmatrix} \text{-}\omega_{p,1} & \omega & 0 & 0 & 0 & 0 & \frac{p_d}{L_1} & 0 & 0 & 0 & 0 \\ \text{-}\omega & \text{-}\omega_{p,1} & 0 & 0 & 0 & 0 & 0 & \frac{p_q}{L_1} & 0 & 0 & \frac{-p_q}{L_1} \\ 0 & 0 & \text{-}\omega_{p,2} & \omega & 0 & 0 & \frac{p_d}{L_2} & 0 & 0 & 0 & 0 \\ 0 & 0 & \text{-}\omega & \text{-}\omega_{p,2} & 0 & 0 & 0 & \frac{p_q}{L_2} & 0 & 0 & \frac{-p_q}{L_2} \\ 0 & 0 & 0 & 0 & \text{-}\omega_{p,3} & \omega & \frac{p_d}{L_3} & 0 & 0 & 0 & 0 \\ 0 & 0 & 0 & 0 & \text{-}\omega & \text{-}\omega_{p,3} & 0 & \frac{p_q}{L_3} & 0 & 0 & \frac{-p_q}{L_3} \\ p_f & 0 & p_f & 0 & p_f & 0 & \frac{-c_s-c_{gr}}{m_p} & \frac{-k_s}{m_p} & \frac{c_s}{m_p} & \frac{k_s}{m_p} & 0 \\ 0 & 0 & 0 & 0 & 0 & 0 & 1 & 0 & 0 & 0 & 0 \\ 0 & 0 & 0 & 0 & 0 & 0 & \frac{c_s}{m_s} & \frac{k_s}{m_s} & \frac{-c_s-c_{sky}}{m_s} & \frac{-k_s}{m_s} & 0 \\ 0 & 0 & 0 & 0 & 0 & 0 & 0 & 0 & 1 & 0 & 0 \\ 0 & 0 & 0 & 0 & 0 & 0 & 0 & 0 & 0 & 0 & 0 \end{bmatrix}$$

$$\boldsymbol{B_h} = \begin{bmatrix} -\frac{p_d}{L_1} & 0 & -\frac{p_d}{L_2} & 0 & -\frac{p_d}{L_3} & 0 & 0 & 0 & 0 & 0 & 1 \end{bmatrix}^\top$$

$$\boldsymbol{C_h} = \begin{bmatrix} 0 & 0 & 0 & 0 & 0 & 0 & 0 & 1 & 0 & 0 & 0 \\ 0 & 0 & 0 & 0 & 0 & 0 & 0 & 0 & 1 & 0 & 0 \\ 0 & 0 & 0 & 0 & 0 & 0 & \frac{c_s}{m_s} & \frac{k_s}{m_s} & \frac{-(c_s+c_{sky})}{m_s} & \frac{-k_s}{m_s} & 0 \end{bmatrix}$$

$$\boldsymbol{D_h} = \begin{bmatrix} 0 & 0 & 0 \end{bmatrix}^\top$$

A.4 Dynamic and Input Gain Matrices for Equivalent Pad (only for state gain matrix)

$$\mathbf{z} = \begin{bmatrix} \dot{z}_p & z_p & \dot{z}_s & z_s \end{bmatrix}^\top$$

$$\boldsymbol{A} = \begin{bmatrix} 0 & -\frac{k_p+k_s}{m_p} & 0 & \frac{k_s}{m_p} \\ 1 & 0 & 0 & 0 \\ 0 & \frac{k_s}{m_s} & 0 & -\frac{k_s}{m_s} \\ 0 & 0 & 1 & 0 \end{bmatrix}$$

$$\boldsymbol{B} = \begin{bmatrix} \frac{1}{m_p} & 0 & -\frac{1}{m_s} & 0 \end{bmatrix}^\top$$

A.5 State Space for Equivalent Pad and LQR Implementation

$$\mathbf{z} = \begin{bmatrix} \dot{z}_p & z_p & \dot{z}_s & z_s \end{bmatrix}^\top$$

$$\mathbf{y} = \begin{bmatrix} z_p & \ddot{z}_s & \dot{z}_p & \dot{z}_s & z_s \end{bmatrix}^\top$$

$$\boldsymbol{A_p} = \begin{bmatrix} 0 & -\frac{k_p+k_s}{m_p} & 0 & \frac{k_s}{m_p} \\ 1 & 0 & 0 & 0 \\ 0 & \frac{k_s}{m_s} & 0 & -\frac{k_s}{m_s} \\ 0 & 0 & 1 & 0 \end{bmatrix}$$

$$\boldsymbol{B_p} = \begin{bmatrix} \frac{k_p}{m_p} & 0 & 0 & 0 \\ \frac{1}{m_p} & 0 & -\frac{1}{m_s} & 0 \end{bmatrix}^\top$$

$$\boldsymbol{C_p} = \begin{bmatrix} 0 & 1 & 0 & 0 \\ 0 & \frac{k_s}{m_s} & 0 & -\frac{k_s}{m_s} \\ 1 & 0 & 0 & 0 \\ 0 & 0 & 1 & 0 \\ 0 & 0 & 0 & 1 \end{bmatrix}$$

$$\boldsymbol{D_p} = \begin{bmatrix} 0 & 0 \\ 0 & -\frac{1}{m_s} \\ 0 & 0 \\ 0 & 0 \\ 0 & 0 \end{bmatrix}$$

A.6 State Space for Equivalent Pad with Passive Damper

$$\mathbf{z} = \begin{bmatrix} \dot{z}_p & z_p & \dot{z}_s & z_s \end{bmatrix}^\top$$

$$\mathbf{y} = \begin{bmatrix} z_p & \ddot{z}_s \end{bmatrix}^\top$$

$$\boldsymbol{A_c} = \begin{bmatrix} -\frac{c_s}{m_p} & -\frac{k_p+k_s}{m_p} & \frac{c_s}{m_p} & \frac{k_s}{m_p} \\ 1 & 0 & 0 & 0 \\ \frac{c_s}{m_s} & \frac{k_s}{m_s} & -\frac{c_s}{m_s} & -\frac{k_s}{m_s} \\ 0 & 0 & 1 & 0 \end{bmatrix}$$

$$\boldsymbol{B_c} = \begin{bmatrix} \frac{k_p}{m_p} & 0 & 0 & 0 \end{bmatrix}^\top$$

$$\boldsymbol{C_c} = \begin{bmatrix} 0 & 1 & 0 & 0 \\ \frac{c_s}{m_s} & \frac{k_s}{m_s} & -\frac{c_s}{m_s} & -\frac{k_s}{m_s} \end{bmatrix}$$

$$\boldsymbol{D_c} = \begin{bmatrix} 0 & 0 \end{bmatrix}^\top$$

A.7 Dynamic and Input Gain Matrices for Pad with Inherent Instability (only for state gain matrix)

$$\mathbf{z} = \begin{bmatrix} i_{d,1} & i_{q,1} & i_{d,2} & i_{q,2} & i_{d,3} & i_{q,3} & \dot{z}_p & z_p & \dot{z}_s & z_s \end{bmatrix}^\top$$

$$p_f = -\frac{2\Lambda_0}{\gamma m_p} \, \mathrm{e}^{-z_{p,0}/\gamma}$$

$$p_d = \frac{\Lambda_0}{\gamma} \, \mathrm{e}^{-z_{p,0}/\gamma}$$

$$p_q = \frac{\omega\Lambda_0}{\gamma} \, \mathrm{e}^{-z_{p,0}/\gamma}$$

$$\boldsymbol{A_{fp}} = \begin{bmatrix} -\omega_{p,1} & \omega & 0 & 0 & 0 & 0 & \frac{p_d}{L_1} & 0 & 0 & 0 \\ -\omega & -\omega_{p,1} & 0 & 0 & 0 & 0 & 0 & \frac{p_q}{L_1} & 0 & 0 \\ 0 & 0 & -\omega_{p,2} & \omega & 0 & 0 & \frac{p_d}{L_2} & 0 & 0 & 0 \\ 0 & 0 & -\omega & -\omega_{p,2} & 0 & 0 & 0 & \frac{p_q}{L_2} & 0 & 0 \\ 0 & 0 & 0 & 0 & -\omega_{p,3} & \omega & \frac{p_d}{L_3} & 0 & 0 & 0 \\ 0 & 0 & 0 & 0 & -\omega & -\omega_{p,3} & 0 & \frac{p_q}{L_3} & 0 & 0 \\ p_f & 0 & p_f & 0 & p_f & 0 & 0 & -\frac{k_s}{m_p} & 0 & \frac{k_s}{m_p} \\ 0 & 0 & 0 & 0 & 0 & 0 & 1 & 0 & 0 & 0 \\ 0 & 0 & 0 & 0 & 0 & 0 & 0 & \frac{k_s}{m_s} & 0 & -\frac{k_s}{m_s} \\ 0 & 0 & 0 & 0 & 0 & 0 & 0 & 0 & 1 & 0 \end{bmatrix}$$

$$\boldsymbol{B_{fp}} = \begin{bmatrix} 0 & 0 & 0 & 0 & 0 & 0 & \frac{1}{m_p} & 0 & -\frac{1}{m_s} & 0 \end{bmatrix}^\top$$

A.8 State Space for Pad with Inherent Instability and LQR Implementation

$$\mathbf{z} = \begin{bmatrix} i_{d,1} & i_{q,1} & i_{d,2} & i_{q,2} & i_{d,3} & i_{q,3} & \dot{z}_p & z_p & \dot{z}_s & z_s & z_{in} \end{bmatrix}^\top$$

$$\mathbf{y} = \begin{bmatrix} z_p & \dot{z}_s & \ddot{z}_s & i_{d,1} & i_{q,1} & i_{d,2} & i_{q,2} & i_{d,3} & i_{q,3} & \dot{z}_p & z_s & z_{in} \end{bmatrix}^\top$$

$$p_f = -\frac{2\Lambda_0}{\gamma m_p} \, \mathrm{e}^{-z_{p,0}/\gamma}$$

$$p_d = \frac{\Lambda_0}{\gamma} \, \mathrm{e}^{-z_{p,0}/\gamma}$$

$$p_q = \frac{\omega\Lambda_0}{\gamma} \, \mathrm{e}^{-z_{p,0}/\gamma}$$

$$\boldsymbol{A_f} = \begin{bmatrix} -\omega_{p,1} & \omega & 0 & 0 & 0 & 0 & \frac{p_d}{L_1} & 0 & 0 & 0 & 0 \\ -\omega & -\omega_{p,1} & 0 & 0 & 0 & 0 & 0 & \frac{p_q}{L_1} & 0 & 0 & -\frac{p_q}{L_1} \\ 0 & 0 & -\omega_{p,2} & \omega & 0 & 0 & \frac{p_d}{L_2} & 0 & 0 & 0 & 0 \\ 0 & 0 & -\omega & -\omega_{p,2} & 0 & 0 & 0 & \frac{p_q}{L_2} & 0 & 0 & -\frac{p_q}{L_2} \\ 0 & 0 & 0 & 0 & -\omega_{p,3} & \omega & \frac{p_d}{L_3} & 0 & 0 & 0 & 0 \\ 0 & 0 & 0 & 0 & -\omega & -\omega_{p,3} & 0 & \frac{p_q}{L_3} & 0 & 0 & -\frac{p_q}{L_3} \\ p_f & 0 & p_f & 0 & p_f & 0 & 0 & -\frac{k_s}{m_p} & 0 & \frac{k_s}{m_p} & 0 \\ 0 & 0 & 0 & 0 & 0 & 0 & 1 & 0 & 0 & 0 & 0 \\ 0 & 0 & 0 & 0 & 0 & 0 & 0 & \frac{k_s}{m_s} & 0 & -\frac{k_s}{m_s} & 0 \\ 0 & 0 & 0 & 0 & 0 & 0 & 0 & 0 & 1 & 0 & 0 \\ 0 & 0 & 0 & 0 & 0 & 0 & 0 & 0 & 0 & 0 & 0 \end{bmatrix}$$

$$\boldsymbol{B_f} = \begin{bmatrix} -\frac{p_d}{L_1} & 0 & -\frac{p_d}{L_2} & 0 & -\frac{p_d}{L_3} & 0 & 0 & 0 & 0 & 0 & 1 \\ 0 & 0 & 0 & 0 & 0 & 0 & \frac{1}{m_p} & 0 & -\frac{1}{m_s} & 0 & 0 \end{bmatrix}^\top$$

$$\boldsymbol{C_f} = \begin{bmatrix} 0 & 0 & 0 & 0 & 0 & 0 & 0 & 1 & 0 & 0 & 0 \\ 0 & 0 & 0 & 0 & 0 & 0 & 0 & 0 & 1 & 0 & 0 \\ 0 & 0 & 0 & 0 & 0 & 0 & 0 & \frac{k_s}{m_s} & 0 & -\frac{k_s}{m_s} & 0 \\ 1 & 0 & 0 & 0 & 0 & 0 & 0 & 0 & 0 & 0 & 0 \\ 0 & 1 & 0 & 0 & 0 & 0 & 0 & 0 & 0 & 0 & 0 \\ 0 & 0 & 1 & 0 & 0 & 0 & 0 & 0 & 0 & 0 & 0 \\ 0 & 0 & 0 & 1 & 0 & 0 & 0 & 0 & 0 & 0 & 0 \\ 0 & 0 & 0 & 0 & 1 & 0 & 0 & 0 & 0 & 0 & 0 \\ 0 & 0 & 0 & 0 & 0 & 1 & 0 & 0 & 0 & 0 & 0 \\ 0 & 0 & 0 & 0 & 0 & 0 & 1 & 0 & 0 & 0 & 0 \\ 0 & 0 & 0 & 0 & 0 & 0 & 0 & 0 & 0 & 1 & 0 \\ 0 & 0 & 0 & 0 & 0 & 0 & 0 & 0 & 0 & 0 & 1 \end{bmatrix}$$

$$\boldsymbol{D_f} = \begin{bmatrix} 0 & 0 & 0 & 0 & 0 & 0 & 0 & 0 & 0 & 0 & 0 \\ 0 & 0 & -\frac{1}{m_s} & 0 & 0 & 0 & 0 & 0 & 0 & 0 & 0 \end{bmatrix}^\top$$

A.9 State Space for Pad with Inherent Instability and Passive Damper

$$\mathbf{z} = \begin{bmatrix} i_{d,1} & i_{q,1} & i_{d,2} & i_{q,2} & i_{d,3} & i_{q,3} & \dot{z}_p & z_p & \dot{z}_s & z_s & z_{in} \end{bmatrix}^\top$$

$$\mathbf{y} = \begin{bmatrix} z_p & \dot{z}_s & \ddot{z}_s \end{bmatrix}^\top$$

$$p_f = -\frac{2\Lambda_0}{\gamma m_p} \, \mathrm{e}^{-z_{p,0}/\gamma}$$

$$p_d = \frac{\Lambda_0}{\gamma} \, \mathrm{e}^{-z_{p,0}/\gamma}$$

$$p_q = \frac{\omega\Lambda_0}{\gamma} \, \mathrm{e}^{-z_{p,0}/\gamma}$$

$$\boldsymbol{A_{fc}} = \begin{bmatrix} -\omega_{p,1} & \omega & 0 & 0 & 0 & 0 & \frac{p_d}{L_1} & 0 & 0 & 0 & 0 \\ -\omega & -\omega_{p,1} & 0 & 0 & 0 & 0 & 0 & \frac{p_q}{L_1} & 0 & 0 & \frac{-p_q}{L_1} \\ 0 & 0 & -\omega_{p,2} & \omega & 0 & 0 & \frac{p_d}{L_2} & 0 & 0 & 0 & 0 \\ 0 & 0 & -\omega & -\omega_{p,2} & 0 & 0 & 0 & \frac{p_q}{L_2} & 0 & 0 & \frac{-p_q}{L_2} \\ 0 & 0 & 0 & 0 & -\omega_{p,3} & \omega & \frac{p_d}{L_3} & 0 & 0 & 0 & 0 \\ 0 & 0 & 0 & 0 & -\omega & -\omega_{p,3} & 0 & \frac{p_q}{L_3} & 0 & 0 & \frac{-p_q}{L_3} \\ p_f & 0 & p_f & 0 & p_f & 0 & \frac{-c_s}{m_p} & \frac{-k_s}{m_p} & \frac{c_s}{m_p} & \frac{k_s}{m_p} & 0 \\ 0 & 0 & 0 & 0 & 0 & 0 & 1 & 0 & 0 & 0 & 0 \\ 0 & 0 & 0 & 0 & 0 & 0 & \frac{c_s}{m_s} & \frac{k_s}{m_s} & \frac{-c_s}{m_s} & \frac{-k_s}{m_s} & 0 \\ 0 & 0 & 0 & 0 & 0 & 0 & 0 & 0 & 1 & 0 & 0 \\ 0 & 0 & 0 & 0 & 0 & 0 & 0 & 0 & 0 & 0 & 0 \end{bmatrix}$$

$$\boldsymbol{B_{fc}} = \begin{bmatrix} -\frac{p_d}{L_1} & 0 & -\frac{p_d}{L_2} & 0 & -\frac{p_d}{L_3} & 0 & 0 & 0 & 0 & 0 & 1 \end{bmatrix}^\top$$

$$\boldsymbol{C_{fc}} = \begin{bmatrix} 0 & 0 & 0 & 0 & 0 & 0 & 0 & 1 & 0 & 0 & 0 \\ 0 & 0 & 0 & 0 & 0 & 0 & 0 & 0 & 1 & 0 & 0 \\ 0 & 0 & 0 & 0 & 0 & 0 & \frac{c_s}{m_s} & \frac{k_s}{m_s} & \frac{-c_s}{m_s} & \frac{-k_s}{m_s} & 0 \end{bmatrix}$$

$$\boldsymbol{D_{fc}} = \begin{bmatrix} 0 & 0 & 0 \end{bmatrix}^\top$$

A.10 Weighting Parameter Matrix for States of Reduced Order System

$$\boldsymbol{Q} = \begin{bmatrix} 1-r & 0 & 0 & 0 \\ 0 & 0 & 0 & 0 \\ 0 & 0 & r & 0 \\ 0 & 0 & 0 & 0 \end{bmatrix}$$

A.11 Weighting Parameter Matrix for States of System with Inherent Instability

$$\boldsymbol{Q_f} = \begin{bmatrix} 0 & 0 & 0 & 0 & 0 & 0 & 0 & 0 & 0 & 0 \\ 0 & 0 & 0 & 0 & 0 & 0 & 0 & 0 & 0 & 0 \\ 0 & 0 & 0 & 0 & 0 & 0 & 0 & 0 & 0 & 0 \\ 0 & 0 & 0 & 0 & 0 & 0 & 0 & 0 & 0 & 0 \\ 0 & 0 & 0 & 0 & 0 & 0 & 0 & 0 & 0 & 0 \\ 0 & 0 & 0 & 0 & 0 & 0 & 0 & 0 & 0 & 0 \\ 0 & 0 & 0 & 0 & 0 & 0 & 1-r & 0 & 0 & 0 \\ 0 & 0 & 0 & 0 & 0 & 0 & 0 & 0 & 0 & 0 \\ 0 & 0 & 0 & 0 & 0 & 0 & 0 & 0 & r & 0 \\ 0 & 0 & 0 & 0 & 0 & 0 & 0 & 0 & 0 & 0 \end{bmatrix}$$

Bibliography

[1] R. Galluzzi, S. Circosta, N. Amati, A. Tonoli, A. Bonfitto, T. A. Lembke, and M. Kertész. «Multi-domain Approach to the Stabilization of Electrodynamic Levitation Systems». In: *ASME: Journal of Vibration and Acoustics* Vol. 142 (Dec. 2020) (cit. on pp. 1, 42).

[2] A. Tonoli. «Dynamic characteristics of eddy current dampers and couplers». In: *Journal of Sound and Vibration* Vol. 301 (2007), pp. 576–591 (cit. on p. 2).

[3] J. H. Jeong, C. W. Ha, M. Kim, J. Lim, and J. Y. Choi. «Experimental Verification and Electromagnetic Analysis for Force Performance of Levitation and Guidance Electromagnet in Semi-high-speed Maglev Train». In: *IEEE Transactions on Magnetics* Vol. 52. No. 7 (July 2016) (cit. on p. 4).

[4] Z. Deng, W. Zhang, L. Kou, Y. Cheng, H. Huang, L. Wang, J. Chen, Z. Ke, and Q. Ma. «An Ultra-High-Speed Maglev Test Rig Designed for HTS Pinning Levitation and Electrodynamic Levitation». In: *IEEE Transactions on Applied Superconductivity* Vol. 31. No. 8 (Nov. 2021) (cit. on p. 4).

[5] R. F. Post. *Inductrack Demonstration Model*. Tech. rep. CA. U.S.A.: Lawrence Livermore National Lab., Feb. 1998 (cit. on p. 15).

[6] A. Soyiç and S. Türkay. «On the Optimization of the Semi-Active Suspension for a Railway Vehicle». In: *IFAC PapersOnLine* Vol. 53. No. 2 (2020) (cit. on pp. 23, 29).

[7] G. Rill. «Road Vehicle Dynamics: Fundamentals and Modeling». In: Regensburg, Germany: CRC Press, 2011. Chap. 2, pp. 27–41 (cit. on pp. 37–39).

[8] J. Shi, Q. Wei, and Y. Zhao. «Analysis of dynamic response of the high-speed EMS maglev vehicle/guideway coupling system with random irregularity». In: *Vehicle System Dynamics* Vol. 45. No. 12 (Dec. 2007), pp. 1077–1095 (cit. on p. 39).

[9] C. F. Zhao and W. M. Zhai. «Maglev Vehicle/Guideway Vertical Random Response and Ride Quality». In: *Vehicle System Dynamics: International Journal of Vehicle Mechanics and Mobility* Vol. 38. No. 3 (2002), pp. 185–210 (cit. on p. 39).

[10] H. E. Tseng and D. Hrovat. «State of the art survey: active and semi-active suspension control». In: *Vehicle System Dynamics: International Journal of Vehicle Mechanics and Mobility* (2015) (cit. on p. 41).

[11] M. S. Kumar and S. Vijayarangan. «Linear quadratic regulator controller design for active suspension system subjected to random road surfaces». In: *Journal of Scientific and Industrial Research* Vol. 65 (Mar. 2006), pp. 213–226 (cit. on p. 41).

[12] M.P. Nagarkar, G.J. Vikhe, K.R. Borole, and V.M. Nandedkar. «Active Control of Quarter-car Suspension System Using Linear Quadratic Regulator». In: *International Journal of Automotive and Mechanical Engineering* Vol. 3 (Mar. 2011), pp. 364–372 (cit. on p. 41).

[13] H. Tsunashima and M. Abe. «Static and Dynamic Performance of Permanent Magnet Suspension for Maglev Transport Vehicle». In: *Vehicle System Dynamics* Vol. 29. No. 2 (Mar. 1998), pp. 83–111 (cit. on p. 42).

[14] M. Dumitriu and D. I. Stănică. «Study on the Evaluation Methods of the Vertical Ride Comfort of Railway Vehicle—Mean Comfort Method and Sperling's Method». In: *Applied Sciences* Vol. 11 (2021) (cit. on p. 68).

[15] W. T. Fan and W. F. Wu. «Dynamic Analysis and Ride Quality Evaluation of Railway Vehicles - Numerical Simulation and Field Test Verification». In: *Journal of Mechanics* Vol. 22. No. 1 (2006) (cit. on p. 68).